



Supercontinuum Generation in Nanophotonic Silicon Nitride Waveguides.

Christensen, Simon

Publication date:
2021

Document Version
Publisher's PDF, also known as Version of record

[Link back to DTU Orbit](#)

Citation (APA):
Christensen, S. (2021). *Supercontinuum Generation in Nanophotonic Silicon Nitride Waveguides*. Technical University of Denmark.

General rights

Copyright and moral rights for the publications made accessible in the public portal are retained by the authors and/or other copyright owners and it is a condition of accessing publications that users recognise and abide by the legal requirements associated with these rights.

- Users may download and print one copy of any publication from the public portal for the purpose of private study or research.
- You may not further distribute the material or use it for any profit-making activity or commercial gain
- You may freely distribute the URL identifying the publication in the public portal

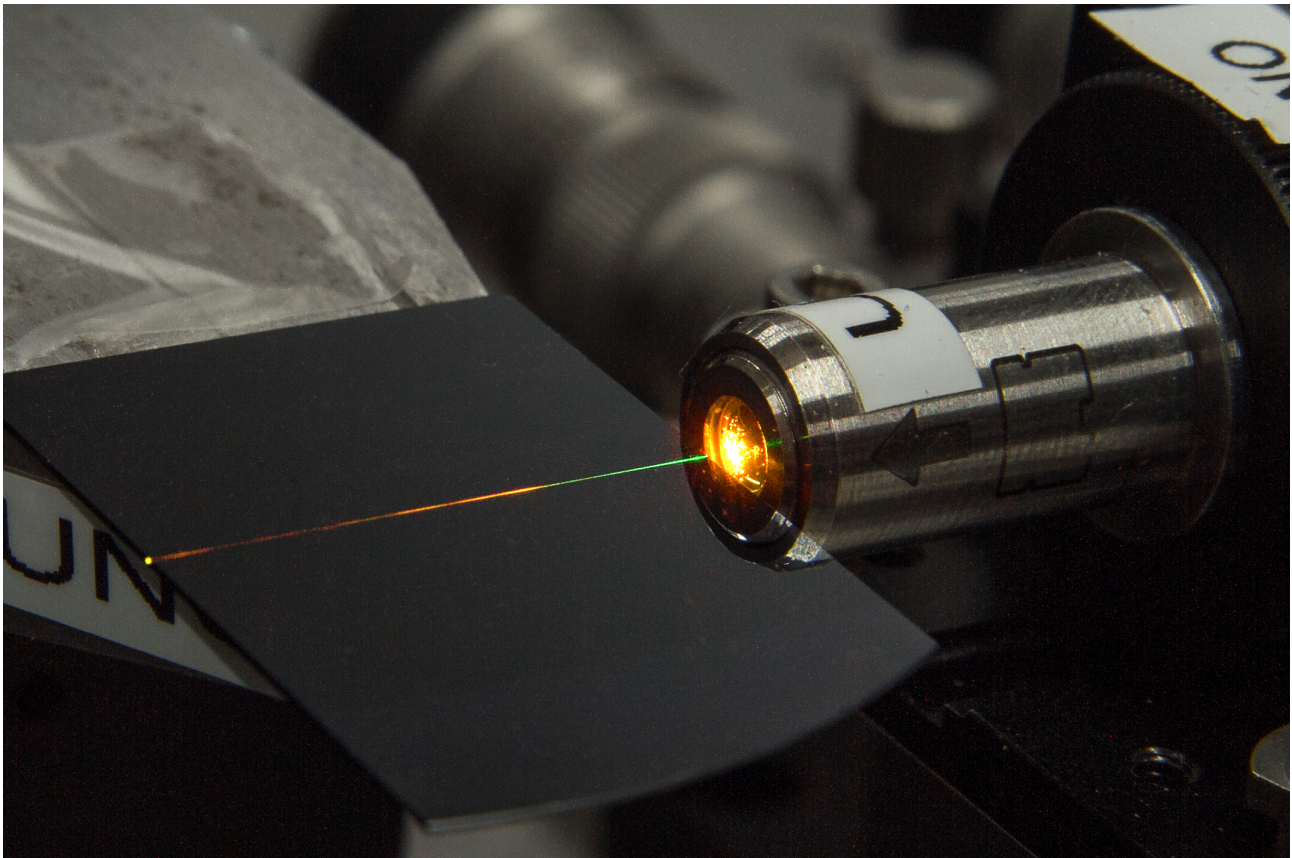
If you believe that this document breaches copyright please contact us providing details, and we will remove access to the work immediately and investigate your claim.

Supercontinuum Generation in Nanophotonic Silicon Nitride Waveguides

Simon Christensen

Ph.D. Thesis

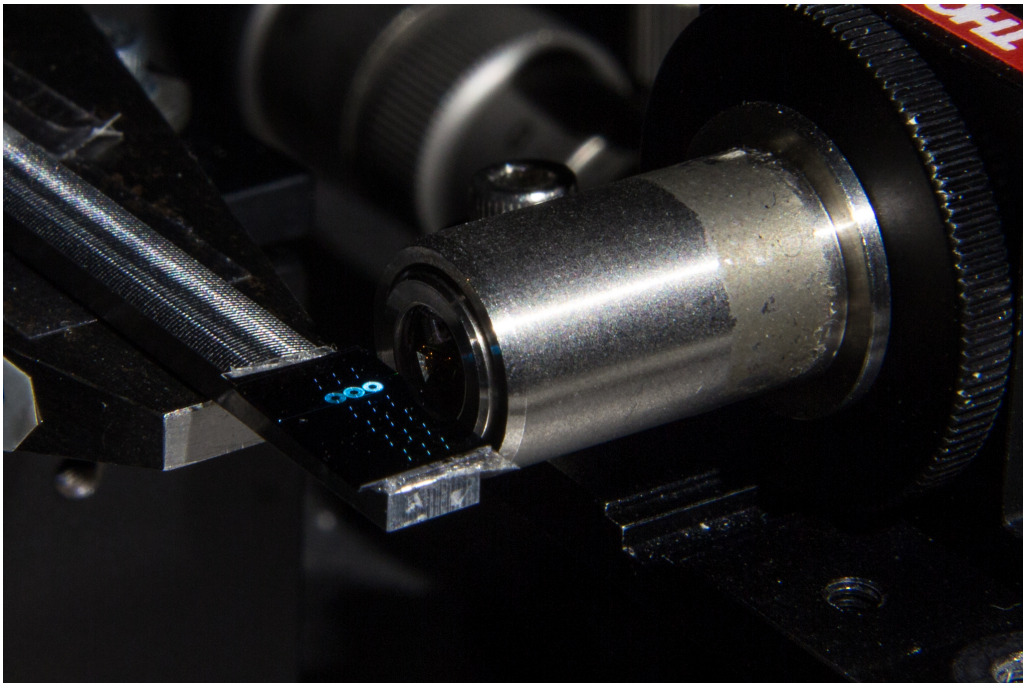
Kongens Lyngby, January 2021



b

Supercontinuum Generation in Nanophotonic Silicon Nitride Waveguides

The influence of dispersion profile on the supercontinuum generation in silicon nitride waveguides



Ph.D. Student:
Simon Christensen

Supervisors:
Professor Peter Uhd Jepsen
Morten Bache
Victor Torres Company
January 2021

d

A thesis submitted to DTU Fotonik for the fulfillment of the requirement of Doctor of
Philosophy in Photonics Engineering



Simon Christensen was founded through the Nordic Five Tech alliance

"Even a poor plan is better than no plan at all."

Mikhael Chigorin

f

Abstract

The generation of supercontinuum (SC) is a long standing research field with applications in metrology, imaging, spectroscopy and telecommunication. While SC in fibers and bulk media have dominated the field, in recent years generating SC in on-chip waveguides have been a heavily researched topic. Especially the on-chip generation of octave spanning SC for stabilized optical frequency combs (OFC) has been a major driving force. On-chip SC is vital component for broadband integrated photonics. The miniaturization of optical components would enable devices with smaller footprint, lower power consumption and reduced cost. On-chip SC has been generated in waveguides of various materials. The material used throughout this thesis is silicon nitride (SiN). It is a CMOS compatible material with low loss and high nonlinearity. It does not suffer from two photon absorption (TPA) and fabrication techniques are mature enough that a large range of waveguide sizes can be fabricated. Throughout the thesis, both Si_3N_4 and silicon-rich nitride (SiRN) waveguides are used. Increasing the silicon content increases the nonlinearity, but also increases the loss. Because of this it is necessary to use the low loss Si_3N_4 for long waveguides, while in short waveguides the increased nonlinearity of (SiRN) makes it preferable. Research has tended to focus on using the waveguide geometry to dispersion engineering waveguides with anomalous dispersion. This method of supercontinuum generation (SCG) suffers from a number of limitations, as it is governed by the dynamics of the soliton. Here, we have studied several different techniques for generating SC in silicon nitride waveguides. By engineering the dispersion profile of the waveguides dramatically different SC can be generated. Initially, the use of SiRN waveguides for SCG is investigated. The increased silicon content increases the nonlinear effect and modifies the dispersion. In these anomalous dispersion waveguides the well known combination of soliton compression and dispersive wave (DW) emission generates an octave spanning SC. It is numerically shown that by increasing the silicon content, the phase matching wavelength of the mid infrared (MID-IR) DW is pushed further into the infrared. The concept of increasing silicon content, as a way to dispersion engineer the waveguide, is shown to be a simple way of enabling a larger range of DW wavelengths with phase matching all the way to 5 μm . Previous results in on-chip SC are mainly based on anomalous dispersion waveguides. We have performed a thorough investigation of SC generated in an all normal dispersion (ANDi) Si_3N_4 waveguide. A 20 cm Si_3N_4 spiral waveguide is designed with all normal dispersion. The SC is found to retain very low relative intensity noise (RIN) for all pump powers while generating a SC from

1150nm to 1950nm. This is compared to the spectrum and noise of an anomalous dispersion waveguide. It is shown that the RIN of the anomalous dispersion waveguide rapidly increases after soliton fission. Even at soliton fission simulations show that the anomalous waveguide cannot retain low noise over the full bandwidth. One key result is that an octave spanning SC is generated using 22 pJ of pulse energy in an anomalous dispersion spiral waveguide. The ANDi SC has a much flatter spectrum, and numerical simulations show that the flatness could be improved by shaping the input laser pulse to a gaussian. Additionally, it is numerically shown that ANDi waveguides retain coherence for longer pump pulses, and the main decoherence is caused by the noise seeded Raman gain, which is expected to be significantly weaker in SiN waveguides when compared to silica fibers. It is clear from these simulations that for long pulse SCG it is necessary to use long waveguides. These waveguides could be implemented using a spiral design. The observations confirm that ANDi waveguides enable a flatter SC to be generated with a lower RIN using longer input pulses. The key limiting factors are the need for higher pulse energies and a flat dispersion profile.

Finally, we numerically study SCG by pumping a SiRN waveguide with two zero-dispersion wavelengths (ZDW). The waveguide dispersion is designed so that the pump pulse is in the normal dispersion region (NDR). We show, that because of self phase modulation (SPM), the initial pulse broadens into the anomalous dispersion region (ADR) and forms a soliton. The interaction of the soliton and the broadened pulse in the NDR causes additional spectral broadening through formation of DWs by non-degenerate four-wave mixing (FWM). It is shown that pumping in either NDR results in broadening towards the other NDR. This effect is reproduced in a micro structured fiber (MSF) with a similar dispersion profile. Finally, it is shown that by increasing the input pulse power, the soliton generated can be launched through the ZDW into the opposite NDR.

We are confident that the presented research sheds new insight on generating supercontinuum in on-chip waveguides using any of the mentioned concepts. This paves the way for small footprint supercontinuum sources with improved performance in terms of bandwidth and noise.

Dansk resumé

Superkontinuums generering er et langvarigt forskningsfelt med anvendelser indenfor metrologi, billeddannelse, spektroskopi og telekommunikation. Feltet har været domineret af superkontinuum dannet i fiber, men i de senere år har superkontinuum i chip-baserede bølgeledere været et meget aktivt forskningsfelt. Specielt muligheden for at anvende superkontinuum, der dækker over en oktav, til stabilisering af optiske frekvenskamme har været en af drivkrakterne bag den øgede interesse. I denne afhandling har vi undersøgt flere forskellige teknikker til at lave superkontinuum i siliciumnitrid bølgeledere. Til at starte med undersøges superkontinuums generering i bølgeledere med et øget indhold af silicium. Det øgede silicium indhold forstærker den ikke lineære effekt og forandrer lysets dispersion i bølgelederen. I bølgeledere med anormal dispersion er det den velkendte kombination af solitonkomprimering og dispersive bølger, som danner et superkontinuum. Det vises numerisk, at man ved at øge siliciumindholdet kan justere bølgelængden, hvor disse dispersive bølger bliver dannet. Dette kan udnyttes til at generere lys dybere i de infrarøde bølgelængder. Dette sker ved at siliciumindholdet ændrer lysets dispersion i bølgelederen, og derved kan fasematching af de dispersive bølger justeres helt op til 5 μm .

Tidligere resultater i chipbaserede bølgeledere bygger hovedsageligt på anormale bølgeledere. Vi har lavet et gennemgående studie af Si_3N_4 bølgeledere med normal dispersion. En 20 cm spiralformet bølgeleder er designet til at have normal dispersion ved alle bølgelængder. Dispersionen bliver bekræftet med en interferometrisk måling. Derefter måles den relative intensitets støj og superkontinuumet. Støjen er lav for alle anvendte pulsenergier, og ved maximal effekt dannes et superkontinuum med bredde fra 1150 nm til 1950 nm. På samme måde måles spektrum og støj i en anormal bølgeleder. Det viser sig at i disse anormale bølgeledere stiger støjen hurtigt efter soliton spaltningen. Desuden viser simuleringer, at selv ved soliton spaltningen er der ikke lav støj over hele spektret. Både eksperimenter og simuleringer af støjen viser lavere støj i de dispersive bølger end i resten af spektret. Et nøgleresultat er, at et oktavdækkende superkontinuum bliver genereret med kun 22 pJ pulsenergi. Vi finder at normal dispersion superkontinuum har et langt fladere spektrum, og simuleringer viser, at udjævnerne i spektret kan reduceres ved brug af en laserpuls med en mere gaussisk form. Numerisk vises det, at kohærent superkontinuum kan genereres i en bølgeleder med normal dispersion, selv ved brug af picosekunds laser pulser. Hovedbegrænsningen er støj introduceret af Raman forstærkningen, som dog forventes at være betydeligt lavere end i silica fiber. Det er tydeligt fra disse simuleringer at

lange pulser kræver lange bølgeledere. Disse lange bølgeledere kan implementeres via et spiralformet design. Iagttagelser bekræfter, at superkontinuum fra en normal dispersion bølgeleder kan være fladere og mindre støjfuldt, selv med længere laserpulser som pumpe. Hovedbegrænsningerne er nødvendigheden af højere pulsenergi og en flad dispersion.

Til sidst studeres en siliciumrig nitrid bølgeleder, som har to nuldispersions bølgelængder. Bølgeleder dispersionen er designet sådan, at pumpelaserens bølgelængde er i området med normal dispersion. Vi viser, at pulsen spektralt bredder sig ind i det anormale område og danner en soliton. Interaktionen mellem denne soliton og pulsen i det normale område laver yderligere spektral forbredning gennem dannelsen af dispersive bølger via ikke degenereret firebølgeblanding. Denne forbredning sker mest mod det andet normal dispersions område. Det bliver vist, at det er ligegyldigt hvilket af de to normal dispersions områder, der pumpes i, så vil spektrummet hovedsageligt bredde sig mod det andet normale område. Det er denne foretrukne forbredning af superkontinuumet, som giver det navnet: retningsbestemt superkontinuum. Denne effekt bliver reproduceret i mikrostrukturerede fibre, der har en lignende dispersion. Til sidst vises det, at man ved at øge den brugte pulsenergi kan accelerere solitonen igennem den anden nuldispersions bølgelængde.

Dette studie bidrager med ny viden indenfor chipbaserede superkontinuumsilder, og dette baner vejen for en lille superkontinuumkilde med bedre båndbredde og støj.

Preface

This thesis was prepared at the Department of Photonics Engineering and submitted to the Ph.D. school at the Department of Photonics Engineering as a part of the requirements to obtain the degree of the Ph.D. in Photonics Engineering from the Technical University of Denmark (DTU).

The title of the thesis is "Supercontinuum Generation in Nanophotonic Silicon Nitride Waveguides". The work presented here was done in a three year period from April 2017 to January 2021. The project was carried out at the Department of Photonics Engineering in the Infrared and Terahertz Science Group. The main supervisor was Peter Uhd Jepsen, co-supervisors were Morten Bache and Victor Torres Company.

Kongens Lyngby, January 17, 2021



Simon Christensen

Glossary

ADR	Anomalous Dispersion Region.
ANDi	All Normal Dispersion.
CUT	Chalmers University of Technology.
DTU	Technical University of Denmark.
DW	Dispersive Wave.
FCA	Free Carrier Absorption.
FWM	Four-wave mixing.
GNLSE	Generalized Nonlinear Schrödinger Equation.
GVD	Group Velocity Dispersion.
HOM	Higher Order Modes.
MDW	Minimum Dispersion Wavelength.
MID-IR	Mid-Infrared.
MSF	Micro Structured Fiber.
NDR	Normal Dispersion Region.
Near-IR	Near-Infrared.
NLSE	Nonlinear Schrödinger Equation.
OFC	Optical Frequency Comb.
OWB	Optical Wave Breaking.
PCF	Photonic Crystal Fibre.
Ph.D.	Doctor of Philosophy.
PIC	Photonic Integrated Circuit.
PMI	Polarization Modulation Instability.
QN	Quantum Noise.

RIN	Relative Intensity Noise.
SC	Supercontinuum.
SCG	Supercontinuum Generation.
SiN	Silicon Nitride.
SiRN	Silicon Rich Silicon Nitride.
SPM	Self Phase Modulation.
TPA	Two Photon Absorption.
ZDW	Zero Dispersion Wavelength.

Acknowledgements

I would like to thank a large number of people, without whom this thesis would not exist, or at least would have been much less enjoyable. First of all, I would like to thank Morten Bache for initially hiring me, and for teaching me a large part of what I know about supercontinuum generation. He has always been easily accessible and ready to answer any questions. Furthermore, I would like to thank him for his continued supervision after his leave from academia. It has been of great help, and it is much appreciated. I would also like to thank Peter Uhd Jepsen, for becoming my main supervisor after Mortens leave. Peter has shown great enthusiasm and engagement, especially considering the slightly unfamiliar nature of the project. Most of all I would like to thank him for giving me a large amount of freedom and support, which has been incredible useful when having two kids during my P.h.D. I would then like to express my gratitude for my final supervisor Victor Torres Company. Even as a external collaborator Victor has been heavily involved in the project. Victor was gracious enough to provide feedback, supervision and support, without which, the project would not have been the same. Additionally, I would like to thank Victor for taking great care of me during my external stay in Göteborg. I felt very welcome, and your kind and welcoming attitude made my stay a great experience. As part of this, I would like to thank the whole Ultrafast Photonics Laboratory group at CUT for a warm welcome and a nice stay. A special thanks goes to Zhichao Ye, who has fabricated the waveguides in the thesis. I have greatly enjoyed our collaboration. I am confident that your work has been vital for the success of this project. I have been at DTU for almost four years now, and have met many great and wonderful people here during my stay. And I would like to thank all of the people at the department for a great time. Nevertheless a special mention has to be extended to a few of my colleagues from the Fiber Sensors and Supercontinuum group at DTU. As office neighbours, these people have filled my days at DTU with joy: Kyei Kwarkye, Mikkel Jensen, Abubakar Adamu, Callum Smith, Yazhou Wang, Getinet Woyessa, Christian Rosenberg Petersen, Niels Møller Israelsen and Manoj Kuma Dasa. Similarly I would like to thank: Simon Lehnkov Lange, Tobias Buchmann, Thea Kristensen, Roy Kelner, Daena Madhi, Binbin Zhou, Edmund Kelleher, Martin Cross, Mattias Rasmussen, Henrik Lassen and Malte Welsch from my own group. A special thanks goes to Gaoyuan Li and Shreesha Rao D S, who started their Ph.D. at the same time as me, and shared an office with me. They have been a source of both inspiration and discussion on the details of supercontinuum generation, but perhaps more impor-

tantly two great people to discuss everything from brexit to the ins and outs of the daily live at DTU. Last, but certainly not least, I would like to thank my wife and kids for their support and love during my Ph.D. and especially the last few months.

Contents

Abstract	i
Dansk resumé	iii
Preface	v
Acknowledgements	ix
Contents	xi
1 Introduction	1
1.1 Thesis motivation	1
1.2 Thesis outline	3
1.3 Dissemination activities	4
2 Theory	5
2.1 Background	5
2.2 Nonlinear Schrodinger equation	5
2.2.1 Brief remark on Numerical modelling	7
2.3 Understanding supercontinuum generation	7
2.3.1 Dispersion	8
2.3.2 Kerr nonlinearity	9
2.3.3 Solitons	10
2.3.4 Resonant Radiation Dispersive Waves	11
2.3.5 Raman Gain and the Self Frequency Redshift	11
2.3.6 Modulation instability	13
2.3.7 Optical wave breaking	14
3 Silicon Nitride Waveguides, Silicon Rich and Stoichiometric	17
3.1 Background	17
3.2 Materials and fabrication	18
3.3 Summary	21
4 Anomalous Dispersion Supercontinuum in Silicon Rich Silicon Nitride Waveguides	23

4.1	Background	23
4.2	Dispersive wave control using material and waveguide dispersion . . .	24
4.3	Experimental result	29
	4.3.1 Noise	32
4.4	Summary	32
5	All Normal Dispersion Supercontinuum in Stoichiometric Silicon Nitride Waveguides	35
5.1	Introduction to all normal dispersion supercontinuum generation . . .	35
	5.1.1 Background	35
	5.1.2 Motivation	36
	5.1.3 Fundamental effects, and the influence of waveguide parameters	37
5.2	Dispersion measurements	42
5.3	Experimental setup	45
5.4	Supercontinuum and RIN in 20cm Spiral Waveguides	46
	5.4.1 Comparison to anomalous	53
5.5	Supercontinuum and RIN in 23mm Straight Waveguides	54
5.6	Simulation of picosecond pumped supercontinuum	57
5.7	Octave-spanning frequency comb generation in silicon-rich silicon nitride waveguide	61
5.8	Summary	62
6	Pumping Close to the Zero Dispersion Wavelengths: Directional Supercontinuum	65
6.1	Background	65
6.2	Abstract	65
6.3	Introduction	66
6.4	Numerical simulations	68
	6.4.1 Silicon-rich nitride waveguide	68
	6.4.2 Microstructured fiber	74
6.5	Conclusion	78
6.6	Funding Information	79
7	Conclusion	81
	Bibliography	85
	Appendix A	100
	A. Reprint permission from OSA	101

CHAPTER 1

Introduction

1.1 Thesis motivation

The invention of the first laser marks the starting point for the research field of non-linear optics. Laser sources at many different wavelengths have been developed since the sixties. A present challenge is to generate coherent mid-infrared (MID-IR) laser radiation. Most available lasers operate in the near-infrared (Near-IR) close to the telecommunication bands, but further into the infrared beyond $2\ \mu\text{m}$, laser sources are limited. In the MID-IR the choice of laser is essentially limited to tunable gas lasers, semiconductor lasers, quantum cascade lasers and fiber lasers [1]. Even then the spectral coverage is limited and impractical at many wavelengths [2]. The wavelengths in this region are especially interesting because they overlap with molecular vibration modes. This allows the study of many molecular species and their behavior on an atomic time scale. The MID-IR wavelength region is therefore of great interest for gas sensing and measurements of the atmospheric pollution. Additionally components of human breath, toxic agents and pollutants have fingerprint in this range. Therefore, the advancement of practical laser sources in the infrared is an enabling technology for pollution control, food quality control and noninvasive testing such as breath analysis. Finally, the generation of infrared coherent radiation will offer important improvements in communication and imaging. Because of these areas of application, infrared laser sources have been a major topic of research. One way of generating coherent radiation at new wavelengths is using the nonlinear optical interactions of a material. One such method is supercontinuum generation (SCG). Supercontinuum (SC) is an umbrella term covering a large number of nonlinear processes and effects. The main criterion is a significant spectral broadening of the input laser, where the spectrum is partly continuous. The large bandwidth of SC sources provide spectral coverage at most wavelengths without the need for additional laser sources. The combination of broadband spectrum and coherence is the key strength of a SC source. While SCG was first discovered in the seventies [3], it really took off as a commercial idea with the introduction of photonic crystal fiber (PCF) and efficient pump lasers [4]. By using the many degrees of freedom available in PCF's design, anomalous dispersion could be achieved at many different wavelengths [5], and the supercontinuum spectrum could be generated over a large range of wavelengths. Because of the mode confinement of the PCF the necessary power is comparatively low [6]. Applications of SCG have been found in spectroscopy [7], microscopy, telecommunication [8], optical

coherence tomography [9] and pulse compression [10]. One of the most interesting applications is in optical frequency metrology. The introduction of coherently generated octave spanning SC has allowed the construction of a stabilized optical frequency comb (OFC) which can be used as an ultra precise optical clock [11]. Advances in fiber and laser technology has allowed the miniaturization of the SCG sources[7]. One way to further reduce the footprint and power requirements is to go into on-chip photonic integrated circuits (PIC). The possibility of SCG on-chip combined with various other on-chip devices such as, modulators, splitter, filters and detectors would enable a wide range of applications to be performed with PIC. This lab on a chip concept has several benefits, as it enables the fabrication of full scale devices with a very small footprint. It has good mechanical stability, and as a consequence of the low mode area and high nonlinear effect, it requires low pulse energies. The low energy requirement enables on-chip SCG to be achieved, using GHz repetition rate sources [12]. Possible applications include communication [13, 14], microwave photonics [15, 16], navigation [17], optical clocks [18], biosensing [19] and spectroscopy [20]. One goal of PIC's is a fully integrated OFC, for telecommunication or dual comb spectroscopy [21, 22]. In the recent decade SCG in nanophotonic waveguides have been a heavily researched subject [23]. Most research in on-chip waveguides are focused on anomalous dispersion waveguides using soliton compression and dispersive waves (DW) as the main method of generating coherent SC. By exploiting the soliton compression and DW emission, octave spanning SC can be generated, which is for vital OFC self referencing. The key strength of the anomalous waveguides lies in the ease of dispersion engineering using the strong confinement of the waveguiding structure. The phase matching wavelengths of the DW is adjusted by varying the dimensions of the waveguide. A lot of the initial work was done in silicon waveguides, but for pump lasers below $2.1 \mu\text{m}$, the low material bandgap caused two photon absorption (TPA) and free carrier absorption (FCA) [24], which limits the SC. As some of the most used laser sources, such as Ti:Sapphire, Erbium-doped or Yb-doped, emit below $2.1 \mu\text{m}$ it is a significant drawback. If pump wavelengths above $2.1 \mu\text{m}$ are used, the TPA and FCA are reduced, and SC can be generated in the MID-IR [25, 26]. Instead a heavily used material these days is SiN. A larger bandgap ensures low nonlinear absorption. Early results have shown large amount of broadening in the visible to $2.5 \mu\text{m}$ region [27–30]. It has been shown that f-2f self referencing can be performed at relative low power [12]. As fabrication techniques have been optimized, larger waveguides have been fabricated and recent results have shown DWs generated in 2.5 to $4 \mu\text{m}$ region, when pumped with a 1550 nm laser[31].

Chalmers University of Technology (CUT) has over the past years refined a fabrication technique of silicon-nitride thin-film optical waveguides on silicon wafers and showed, that silicon-rich nitride (SiRN) has larger nonlinearities and simpler fabrication techniques than other versions of silicon nitride (SiN) [32]. Using these waveguides, an octave-spanning SC was generated at DTU Fotonik by pumping with a femtosecond fiber laser [33]. Additionally low loss stoichiometric waveguides have been fabricated [34]. The state of the art fabrication makes it possible to design waveguides with a large range of dispersion profiles and lengths.

A lot of promising results have previously been obtained in anomalous dispersion waveguides, but relatively little effort has been put into studying different regimes. This has limited the usefulness of SCG in waveguides, as the soliton dynamics of the anomalous dispersion regime imposes severe restriction [35]. In this thesis I present three different methods for generating supercontinuum in on-chip waveguides. First, the standard anomalous dispersion region where the nonlinear broadening is caused by soliton compression and DWs. The use of material composition for dispersion engineering is examined, and it is shown that it has great potential. Secondly, all normal dispersion (ANDi) waveguides are examined. ANDi based SCG is well known in PCF based SC sources, but it has largely been ignored for on-chip SCG. The broadening is a combination of self phase modulation (SPM) and optical wave breaking (OWB). This enables SCG with low noise and improved spectral flatness. It is shown that long waveguides are necessary for ANDi SCG these long waveguides are fabricated using a spiral design, which enables 20 cm of waveguide on a 1 cm chip. It is shown that the longer waveguides become increasingly important for longer input pulses. Finally, SC generated in a waveguide, where the pump wavelength is in the NDR but close to the ZDW, is investigated. Here it is found that the SC directionally broadens towards the ADR.

It is my hope, that by presenting my work on the different dispersion regions, new insight will be gained, and it will encourage other researchers to explore the different characteristics of the various SCG methods.

1.2 Thesis outline

The thesis consists of the main results obtained during this Ph.D. study. The thesis is divided into seven chapters.

- * **Chapter 1** presents the motivation of the thesis, an overview of the project, an outline of the thesis, as well as the resulting dissemination activities of this Ph.D. study.
- * **Chapter 2** introduces the basic theoretical framework. The equation used for numerical simulations is introduced. Key physical concepts are explained, which form the basis for understanding the results shown in the following chapters.
- * **Chapter 3** introduces the waveguide structure and materials. A handful of simulations and dispersion profiles are shown for a characteristic waveguide with different silicon nitride compositions.
- * **Chapter 4** describes the development of waveguides for operation in the conventional anomalous dispersion regime. In this chapter a numerical map of dispersive waves and material parameters is shown. A large tunability of the dispersive waves in the MID-IR using changes in waveguide geometry and guiding material is shown. Experimental results show a broadband supercontinuum.

- * **Chapter 5** revolves around supercontinuum generated in the all normal dispersion regime. I experimentally demonstrate a supercontinuum spanning from 1150nm to 1950nm in an all normal spiral waveguide. Furthermore, the supercontinuum and noise is compared to an anomalous dispersion waveguide. Finally, the idea of pumping the ANDi waveguide with picosecond pulses is numerically investigated, especially the influence of the Raman gain on the noise is considered.
- * **Chapter 6** presents my work on directional supercontinuum. Here both the anomalous and normal dispersion regions are combined. Numerically the complex dynamics are investigated clarifying the key effect of the soliton.
- * **Chapter 7** provides a summary and conclusion of the previous 6 chapters

1.3 Dissemination activities

The work carried out during the course of this Ph.D. project has resulted in several peer-reviewed journal publications and conference contributions.

Peer-reviewed journal publications

- I. Simon Christensen, Shreesha Rao D. S., Ole Bang, and Morten Bache, "Directional supercontinuum generation: the role of the soliton," J. Opt. Soc. Am. B 36, A131-A138 (2019)
DOI: 10.1364/JOSAB.36.00A131 [36]

Peer-reviewed conference proceedings

- I. S. Christensen, Z. Ye, M. Bache, and V. T. Company . "Octave-spanning frequency comb generation in all-normal-dispersion silicon-rich silicon nitride waveguide," in Conference on Lasers and Electro-Optics, OSA Technical Digest (Optical Society of America, 2020), paper STu3H.7.
DOI: 10.1364/CLEO_SI.2020.STu3H.7 [37]
- II. S. Christensen and M. Bache, "Directional supercontinuum generation," in Advanced Photonics 2018 (BGPP, IPR, NP, NOMA, Sensors, Networks, SPPCom, SOF), OSA Techncail Digest (online) (Optical Society of America, 2018), paper NpTh4C.5.
DOI: 10.1364/NP.2018.NpTh4C.5 [38]

Journal publications in progress

- I. S. Christensen, Z. Ye, M. Bache, and V. T. Company . "Supercontinuum generation in all normal dispersion Si_3N_4 waveguide."

CHAPTER 2

Theory

2.1 Background

The propagation of short optical pulses in a nonlinear medium is a cornerstone in ultrafast photonics. Because of the nonlinear character of the experimental results, it is vital to have a good theoretical understanding. While analytical results are sparse. A lot of progress have been made using numerical solutions. The numerical work relies on the use of the generalized nonlinear schrödinger equation (GNLSE). The first step in deriving a propagation equation for a pulse in an optical medium is to derive the wave equation, while including the nonlinear polarization. Early papers such as [39], reduced the complexity of the equation by separating the carrier and envelope terms. This was done assuming the envelope was slowly varying. But with the continued research into SCG, It was found that the resulting equations seemed to perform well, even when the slowly varying envelope condition was not fulfilled. Various improved conditions was found [40]. Most importantly it was shown that similar equations could be derived by assuming that the backward propagating waves could be neglected [41, 42]. Later work has also included vector components and multiple modes [43, 44]. Finally, most initial derivations focused on obtaining a time domain formulation of the GNLSE. But this make it difficult to include the wavelength dependent nonlinearity. Formulations of GNLSE in the frequency domain conversely allowed a straight forward inclusion of these terms [45, 46]. In the following a brief introduction to the GNLSE and its parameters is given. The key effects governing SCG are introduced. Which works as the bedrock for understanding results obtained in the rest of the thesis.

2.2 Nonlinear Schrodinger equation

In this thesis the governing equation is a single mode frequency domain GNLSE given by eq. 2.1 [46, 47]. As the equation is single mode, it does not take into account any interaction with higher order modes (HOM) of the waveguide. It will be shown in chapter 3 that the waveguides in general contain several modes. The HOM have larger mode areas, and therefore their nonlinear interactions should be limited. Good agreement is found between simulation and experiment throughout the thesis, confirming that the HOM are not vital to understanding the broaden-

ing. Nevertheless, a possible avenue for further research would be including 1-2 additional modes to confirm these assumptions. The electric field is defined as $\vec{E}(\vec{r}, t) = \frac{1}{2}\vec{x}(E(x, y, z, t)\exp(-i\omega_0 t) + \text{c.c.})$ using the Fourier transform we then get $\vec{E}(x, y, z, \omega) = F(x, y, \omega)\tilde{A}(z, \omega - \omega_0)\exp(i\beta_0 z)$, where it has been separated into the transverse mode distribution $F(x, y, \omega)$ and a spectral envelope $\tilde{A}(z, \omega - \omega_0)$.

$$\frac{\partial \tilde{A}'}{\partial z} = i\tilde{\gamma}(\omega)\exp(-\hat{L}(\omega)z)\mathcal{F}\left\{\bar{A}(z, T) \int_{-\infty}^{\infty} R(T') |\bar{A}(z, T - T')|^2 dT'\right\} \quad (2.1)$$

The change of variable $\tilde{A}' = \tilde{A}\exp(-\hat{L}(\omega)z)$ has been employed. Which allows the equation to be solved by ODE solvers. $\tilde{\gamma}(\omega)$ is the nonlinear coefficient given by the unconventional expression

$$\tilde{\gamma}(\omega) = \frac{n_2 n_0 \omega_0}{c n_{eff}(\omega) A_{eff}^{1/4}(\omega)}. \quad (2.2)$$

Where the effective area is defined as usual with

$$A_{eff} = \frac{(\int_{-\infty}^{\infty} |F(x, y)|^2 dx dy)^2}{\int_{-\infty}^{\infty} |F(x, y)|^4 dx dy} \quad (2.3)$$

c is the speed of light in vacuum, n_2 is the nonlinear change in the refractive index of the material given by $n_2 = \frac{3\chi_{xxxx}^{(3)}}{4n_0^2\epsilon_0 c}$, $\chi_{xxxx}^{(3)}$ is the third order susceptibility, ϵ_0 is the vacuum permittivity. n_0 is the effective refractive index of the mode at pump frequency $n_{eff}(\omega_0)$. $\hat{L}(\omega)$ is the linear operator, which includes the propagation constant $\beta(\omega)$ and linear loss $\alpha(\omega)$.

$$\hat{L}(\omega) = i(\beta(\omega) - \beta(\omega_0) - \beta_1(\omega_0)(\omega - \omega_0)) - \alpha(\omega)/2 \quad (2.4)$$

where β_1 is the inverse of the group velocity, z is the propagation distance, \mathcal{F} denotes the Fourier transform. $\bar{A}(z, T)$ is given by

$$\bar{A}(z, T) = \mathcal{F}^{-1}\left\{\frac{\tilde{A}(z, \omega)}{A_{eff}(\omega)^{1/4}}\right\} \quad (2.5)$$

T is the time in the frame of pump pulse and $R(T)$ is the Raman response function. Which takes into account the both the instantaneous and delayed nonlinear effects.

$$R(T) = (1 - f_R)\delta(T) + f_R(\tau_1^{-2} + \tau_2^{-2})\tau_1 \exp(-T/\tau_2) \sin(T/\tau_1) \quad \text{for } T \geq 0 \quad (2.6)$$

f_R is contribution of the delayed Raman response, τ_1 is the oscillation period and τ_2 is the decay time. The material parameters for the Raman effect in silicon nitride is largely unknown. And are usually neglected, or included using the Raman response of silica. In this thesis, the following parameters are used $f_R = 0.2$, $\tau_1 = 13\text{fs}$ and $\tau_2 = 150\text{fs}$ as in Liu et al. [33]. As a frequency domain formulation is used,

it is possible to correctly include the effect of the wavelength dependent effective area [46]. Furthermore, the shock term is easily included. One caveat with this formulation is that the nonlinear coefficient $\tilde{\gamma}$ has different units compared to the conventional γ . This is remedied when introducing the following change of variables. $A(z, T)$ and $\tilde{A}(z, \omega)$ to $C(z, T)$ and $\tilde{C}(z, \omega)$, with the transformation given as $\tilde{C}(z, \omega) = [A_{eff}(\omega)/A_{eff}(\omega_0)]^{-\frac{1}{4}}\tilde{A}(z, \omega)$. This transformation results in the following Eq. (2.7) [46, 47].

$$\frac{\partial \tilde{C}'}{\partial z} = i\tilde{\gamma}(\omega)\exp(-\hat{L}(\omega)z)\left[1 + \frac{\omega - \omega_0}{\omega_0}\right]\mathcal{F}\left\{C\int_{-\infty}^{\infty}R(T')|C(T-T')|^2dT'\right\} \quad (2.7)$$

It now has a nonlinear coefficient $\tilde{\gamma}$, with regular units given by

$$\tilde{\gamma}(\omega) = \frac{n_2n_0\omega_0}{cn_{eff}(\omega)\sqrt{A_{eff}(\omega)A_{eff}(\omega_0)}}. \quad (2.8)$$

All simulations in the thesis solves eq 2.7 using the effective area in eq 2.3, except for chapter 6, where the effective area includes vectorial components following V. and Monro [43].

2.2.1 Brief remark on Numerical modelling

The pulse evolution is found by solving Eq. (2.7), using an ordinary differential equation solver implemented in Matlab. As seen in Eq (2.7) information about the effective area and propagation constant of the waveguide mode is necessary to model the evolution. The group velocity dispersion (GVD) is either measured in an interferometric setup presented in chapter 5, or calculated based on the propagation constant from simulations in COMSOL Multiphysics. The effective area is calculated based on Comsol simulations. Details regarding the Comsol model is shown in chapter 3.

Eq. (2.7) does not contain any noise terms. Noise is added in the initial conditions. Multiple simulations are then performed with different input conditions creating an ensemble of output SC. Statistical analysis of the resulting SC can then be directly compared with experiment. Two types of noise are included in the simulations in this thesis. The noise inherent in the quantum vacuum state is added in the time domain as a Wigner distribution with a zero mean and half a photon standard deviation. The technical noise of the laser is included as a relative intensity noise (RIN) which is modelled with a normal distribution variation in the input pulse energy, or equivalently the input peak power. Based on RIN measurement of the laser, 1% variations of the pulse energy are used. The RIN of the output spectrum is then calculated for a 12nm bin, in order to be comparable to the measured RIN.

2.3 Understanding supercontinuum generation

While equation 2.1 contains all the most important effects in SCG, it cannot be solved analytically. And while it can be solved numerically, it is difficult to interpret the

results without having some understanding of the building blocks which are involved in the nonlinear processes. All of these effects can be found in textbooks such as Dudley and Taylor [47] and Agrawal [48]. And they are in general well understood as the results of years of research in optical fibers. Nevertheless, these effects are key to understanding the supercontinuum generated in the thesis, and I will therefore present a brief overview of the different effects, so that they can be referenced later. When combining all of these effects, it becomes possible to interpret the results of a GNLSE simulation. To derive the different effects it is helpful to start from a simpler form of the GNLSE. Here, higher order dispersion, loss, Raman effect, and the wavelength dependence of the nonlinearity have been neglected. This results in the simple NLSE in Eq.2.9.

$$i \frac{\partial A}{\partial z} = \frac{\beta_2}{2} \frac{\partial^2 A}{\partial T^2} + \gamma \left(A(z, T) |A(z, T)|^2 \right) \quad (2.9)$$

Optical pulse propagation is governed by two different effects, the dispersion of the pulse caused by the different group velocity for different colors of light. This is a linear effect. The second effect is the conversion of light into different wavelengths of light by the nonlinear effect of the guiding material. The combination of these two effects can be highly complicated, even for the simple NLSE, and it cannot in general be solved analytically.

2.3.1 Dispersion

Dispersion arises as the pulse travels through the optical medium instead of vacuum. In our case, the pulse travels through a guided mode in the waveguide. In this case, the dispersion is caused by a combination of chromatic dispersion of the various waveguide materials and the dispersion caused by the confinement of the waveguide being wavelength dependent. It is common to express the propagation constant as a Taylor expansion. $\beta(\omega) = \beta_0 + \beta_1(\omega - \omega_0) + \beta_2(\omega - \omega_0)^2 + \dots$ where $\beta_m = \left(\frac{\partial^m \beta}{\partial \omega^m} \right)_{\omega=\omega_0}$. In a comoving frame, only the second order derivative β_2 or higher is of importance. $\beta_2 < 0$ is defined as anomalous dispersion, while wavelengths with $\beta_2 > 0$ are normal dispersion. At the crossing point one has the zero dispersion wavelength $\beta_2(\lambda_{ZDW}) = 0$. While dispersion is a linear effect, it is very important for understanding the nonlinear interactions in a waveguide. If the nonlinearity is neglected, the reduced equation is.

$$i \frac{\partial A}{\partial z} = \frac{i\beta_2}{2} \frac{\partial^2 A}{\partial T^2} \quad (2.10)$$

It can easily be solved using the fourier transform. If the input pulse is assumed to be a gaussian $A(0, T) = A_0 \exp\left(\frac{T^2}{2T_0^2}\right)$ one arrives at the following expression for instantaneous frequency of the pulse $\delta\omega_c = -\frac{\partial\phi}{\partial T} = \frac{\text{sgn}(\beta_2)(z/L_D)}{1+(z/L_D)^2} \frac{T}{T_0}$. Where the dispersion length is given by $L_D = \frac{T_0^2}{|\beta_2|}$. Based on this, it is concluded that the instantaneous

frequency changes linearly over the pulse. Importantly, the direction of the chirp depends on the sign of β_2 . Essentially, for normal dispersion, the red components travel faster than the blue component and visa versa for anomalous dispersion. This delay of different parts of the pulse is the cause of the pulse broadening in time.

The dispersion influences SCG through phase matching conditions and by introducing varying propagation speed for different parts of the pulse. This controls the interaction different parts of the spectrum can have, and is therefore vital in understanding the final spectrum and pulse shape. Because the sign of the group velocity dispersion (GVD) influences the frequency chirp of the pulse, it is a very important characteristic, when understanding SCG.

2.3.2 Kerr nonlinearity

The Kerr nonlinearity is an instantaneous change in the refractive index, when the guiding materials are interacting with the laser pulse. The temporal intensity of the pulse modifies the refractive index of the mode linearly with the instantaneous power of the pulse. This results in an intensity dependent phase, which generates new frequencies. To only consider the nonlinear effect, the group velocity dispersion in equation 2.9 is neglected. The result is the following equation.

$$i\frac{\partial A}{\partial z} + = \gamma \left(A(z, T) |A(z, T)|^2 \right) \quad (2.11)$$

This is easily solved by integration, yielding the solution

$$A(z, T) = A(0, T) e^{i\gamma |A(0, T)|^2 z} \quad (2.12)$$

If the result is separated into phase and amplitude, it is straight forward to show that the shift in the instantaneous frequencies of the pulse given by

$$\delta\omega_c(z, t) = -\frac{\partial}{\partial t} (\gamma |A(0, T)|^2 z) \quad (2.13)$$

The exact behaviour is of course dependent on the input pulse shape, but some intuition can be gained by examining a Gaussian input pulse $A(0, T) = A_0 \exp(-\frac{T^2}{2T_0^2})$.

$$\delta\omega_c(z, t) = \frac{2\gamma z T}{T_0^2} |A_0|^2 \exp(-\frac{T^2}{T_0^2}) \quad (2.14)$$

A few things can be understood by examining this result. The frequency chirp becomes red shifted near the leading edge and blue shifted near the trailing edge. Importantly, this is the opposite of the dispersion induced frequency chirp with anomalous dispersion. In the center of the pulse a linear chirp can be expected. While at the edges of pulse the frequency chirp will go towards zero. As the instantaneous frequencies at the edges approaches zero, they must cross the frequencies of other parts of the pulse. It is these identical frequencies at different phases, which interfere to create large peaks and dips in the spectrum.

2.3.3 Solitons

In practise, the dispersion and nonlinearity must be examined simultaneously. The sign of the dispersion is vital for the nonlinear evolution. In regions with positive GVD(normal dispersion), the frequency chirp of the dispersion and nonlinearity has the same sign, and the pulse broadens in both time and spectrum. In regions where the GVD is negative(anomalous dispersion), the nonlinear frequency chirp and the dispersion frequency chirp can cancel, which enables the formation of a stable pulse solution. The solution is called a soliton. This is the most important building block for understanding SCG in anomalous dispersion. The fundamental soliton is given by

$$A(z, T) = \sqrt{P_0} \operatorname{sech}(T/T_0) \exp\left(\frac{-i|\beta_2|z}{2T_0^2}\right) \quad (2.15)$$

This can be confirmed as a solution to equation 2.9 by direct insertion. The most important aspect of the soliton is the fact it doesn't change during propagation, even through it experiences both dispersion and a nonlinear phase shift. The perfect balance between these two effects enables the constant propagation of the pulse. Solitons are restricted by the soliton order N , which must be equal to an integer. The soliton order given by $N^2 = \frac{L_D}{L_{NL}}$. With $L_D = T_0^2/|\beta_2|$ being the dispersion length and $L_{NL} = 1/(\gamma P_0)$ being the nonlinear length. Essentially the soliton number is an indication of the relative strength of the linear and nonlinear contributions. For higher integers of N , periodic higher order solitons exists. Higher order solitons do not propagate unchanged, but have a periodic evolution. They compress and expand in time and frequency as they propagate. Figure 2.1 shows an example of the spec-

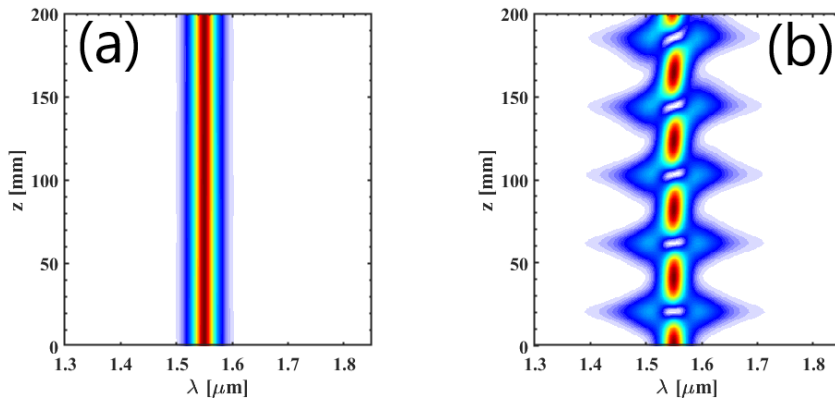


Figure 2.1: (a) Fundamental soliton with $N=1$. (b) Higher order soliton with $N=2$.

tral evolution of a fundamental soliton ($N=1$) and a higher order soliton($N=2$). The higher order soliton periodically broadens in spectrum, and equivalently compresses

in time. While the solitons are sech^2 shaped, and require stringent peak powers to satisfy the soliton order, an arbitrary pulse will attempt to reshape into a soliton as it propagates in the waveguide.

2.3.4 Resonant Radiation Dispersive Waves

Solitons are constant or periodic solutions to the NLSE. They effectively do not experience GVD because of the balance between GVD and nonlinearity. But if additional terms are introduced, especially higher order solitons become unstable. One such additional term is higher order dispersion. If higher order dispersion is included, the GVD will change from anomalous to normal dispersion at the ZDW. The perturbation by the higher order dispersion causes the soliton to fission as it compresses during its periodic evolution. As it fissions the soliton will collapse into several fundamental solitons, which can emit DWs if they are phase matched close enough to the soliton. As solitons do not experience GVD, they have different phase matching conditions, which allow the soliton to phase match to DWs outside the anomalous dispersion region (ADR). DWs are generated at ω_{dw} . As defined by the phase matching condition in eq 2.16 [6].

$$\beta(\omega_{sol}) - \omega_{sol}/v_{g,s} + (1 - f_R)\gamma P_s = \beta(\omega_{dw}) - \frac{\omega_{dw}}{v_{g,s}} \quad (2.16)$$

The term $(1 - f_R)\gamma P_s$ is commonly neglected, as it doesn't have a vital role for most powers used in SCG. Figure 2.2(a) shows an example of a pulse experiencing soliton compression. At $z=8$ mm it fissions, and emits solitons and dispersive waves. Most waveguide designs have two ZDWs and can generate a dispersive wave on both sides of the anomalous dispersion region. The final SC is shown in figure 2.2(b). The phase matching conditions are shown in figure 2.2(c). The DWs are clearly seen in both phase matching and spectrum. This combination of soliton compression and resonant radiation is the most commonly used physical mechanism for generating on-chip SC.

2.3.5 Raman Gain and the Self Frequency Redshift

The spectral bandwidth of the soliton, enables the Raman gain to be understood as a loss at short wavelengths and a gain at long wavelengths. Effectively, this redshifts the central wavelength of the soliton as it propagates. This effect is vital in understanding fiber based supercontinuum sources, but the weak Raman response and short length of most waveguides generally mean, that the effect is neglected in on-chip SCG in SiN waveguides [30]. Nevertheless, the Raman effect has been observed in ring resonator experiments [49]. A comparison of SCG in PCF and SiN, suggest that the influence of Raman limits the coherence of the PCF based SC [50] when using low pulse power for SCG. In this thesis the Raman effect is included as in [33]. The included Raman

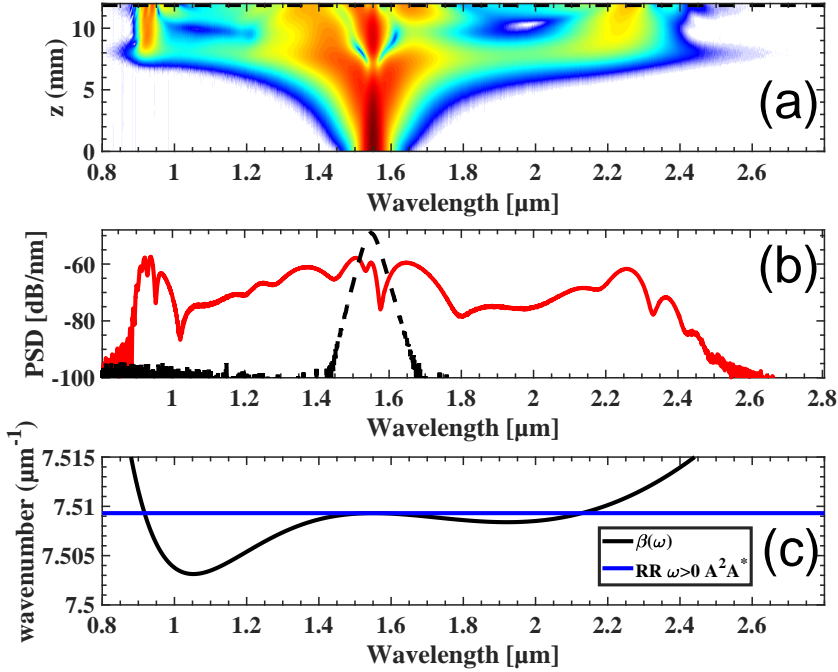


Figure 2.2: (a) Spectral evolution. (b) Spectrum at the end of propagation. (c) Dispersive wave phase matching conditions. Crossing of black and blue indicate phase matching.

effect seem to have little influence on the anomalous supercontinuum simulated in the thesis.

In the normal dispersion regime, no solitons exist, and a self frequency redshift is not expected. Nevertheless, the Raman gain is important for the noise properties of normal dispersion supercontinuum [51]. The Raman gain fundamentally limits the input pulse length for coherent supercontinuum generation. A simple model for the Raman scattering is a single Lorentzian oscillator response function as seen in equation 2.17. And the resulting gain profile can be found using eq. 2.18 [39, 48].

$$h_R(t) = \frac{\tau_1^2 + \tau_2^2}{\tau_1 \tau_2^2} \exp\left(\frac{-t}{\tau_2}\right) \sin\left(\frac{t}{\tau_1}\right), \quad (2.17)$$

$$g_R(\Delta\omega) = \frac{f_R \omega_0}{cn(\omega_0)} \chi_{xxxx}^{(3)} \Im[\mathcal{F}(h_R(t))], \quad (2.18)$$

Where $\tau_1 = 13\text{fs}$ is the inverse of the vibration frequency and $\tau_2 = 150\text{fs}$ is the damping time. The fractional strength of the Raman effect is $f_R = 0.20$.

2.3.6 Modulation instability

Modulation instability is a region of gain inherent to the anomalous dispersion region. The gain is the result of four wave mixing. If this gain is unseeded it leads to the generation of noisy sidebands. In the time domain these noisy sidebands will introduce a temporal modulation. The requirement for anomalous dispersion and the position of the MI instability peaks can be derived as follows. Assuming a simple input continuous wave $A(0, t) = \sqrt{P_0}$ in the simplified propagation equation we get

$$A(z, t) = \sqrt{P_0}e^{-i\gamma P_0 z} \quad (2.19)$$

now we add a small perturbation a_p

$$A(z, t) = (\sqrt{P_0} + a_p)e^{-i\gamma P_0 z} \quad (2.20)$$

If assuming the perturbation is small, results in

$$\frac{\partial a_p}{\partial z} = \frac{i\beta_2}{2} \frac{\partial^2 a_p}{\partial T^2} - i\gamma P_0 \left(a_p(z, T) + a_p(z, T)^* \right) \quad (2.21)$$

Where the solutions have a propagation constant K given by.

$$K = \pm \frac{\beta_2 \Omega}{2} \sqrt{\Omega^2 + \text{sgn}(\beta_2)(\Omega_c)^2}, \quad (2.22)$$

Where $\Omega_c = \frac{4}{\gamma} P_0 |\beta_2|$. In the anomalous dispersion regime $\text{sgn}(\beta_2) < 0$ and there exist frequencies at which K is imaginary, this enables the growth of the small perturbation. This in turn means that the initial input wave is unstable, as the perturbation is increasing. The maximum gain is at the frequencies given by

$$\Omega_{MI-Max} = \pm \sqrt{\frac{2\gamma P_0}{|\beta_2|}}, \quad (2.23)$$

This derivation is valid for a simplified version of the NLSE. It is important to keep in mind, that modulation instability can also occur with positive GVD, if the fourth order dispersion is negative [52]. Modulation instability is one of the main limiting factors of coherent supercontinuum generation. If the pulse doesn't coherently seed the modulation instability gain, the gain will be seeded by the quantum noise, and in turn generate incoherent radiation. This limits coherent SCG in the anomalous dispersion regime to pulse widths of approximately 150 fs or lower. Figure 2.3 shows a simulated example of these modulation instability sidebands.

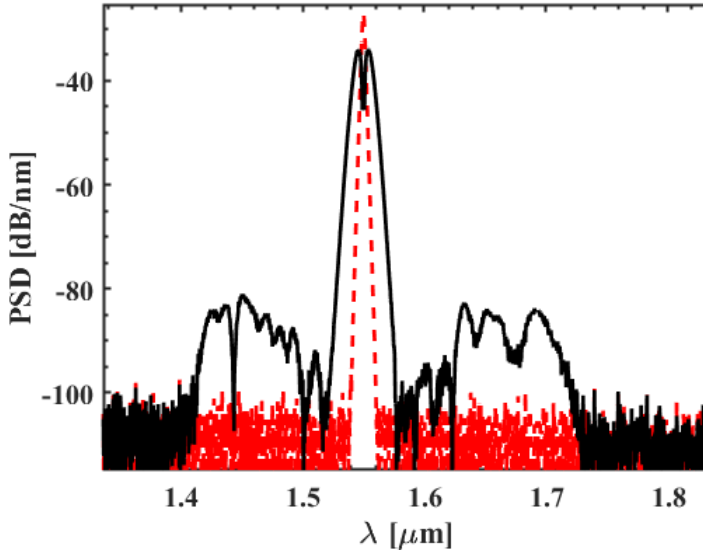


Figure 2.3: Example of modulation instability sidebands seeded by quantum noise..

2.3.7 Optical wave breaking

Optical wave breaking is the spectral broadening associated with the temporal overlap of the heavily chirped central part of a pulse, and the unchirped wings. It has been shown to be a key component in generating broadband supercontinuum in all normal dispersion fiber. No simple analytical solution can be found, but following the derivation of Anderson et al. [53], a few equations can be derived. Let's start by considering the frequency chirp of a Gaussian pulse experiencing only SPM and a Gaussian pulse experiencing only dispersion. From the earlier sections on dispersion and SPM, it is known that

$$\delta\omega_c(z, t) = \frac{2\gamma z T}{T_0^2} |A_0|^2 \exp\left(\frac{-T^2}{T_0^2}\right) \quad (2.24)$$

$$\delta\omega_c(z, t) = \frac{\text{sgn}(\beta_2)(z/L_D) T}{1 + (z/L_D)^2} \frac{T}{T_0} \quad (2.25)$$

As an approximation, it is assumed that the total frequency chirp is just the sum of the two. Now let's imagine a pulse with two parts initially separated by a time $\Delta\tau$, after the pulse has traveled some distance z , the separation between the two parts has changed by $\Delta\tau'$, with $\Delta\tau' = z\beta_2 \frac{\partial\omega}{\partial\tau} \Delta\tau$. The two parts will overlap in time when $-\Delta\tau' = \Delta\tau$. As OWB is exactly this temporal overlap of different parts of the pulse, the OWB distance is $z_{OWB} = \frac{-1}{\beta_2 \frac{\partial\omega}{\partial\tau}}$. By inserting the combined chirp of eq 2.24, one

then obtains

$$\left(\frac{z_{OWB}}{L_D}\right)^2 = \frac{-1}{1 - N^2(1 - 2\tau^2/T_0^2)\exp(-\tau^2/T_0^2)} \quad (2.26)$$

The maximum wave breaking length can then be shown to occur at

$$\left(\frac{z_{OWB}}{L_D}\right) = \frac{1}{\left(\frac{N^2}{\exp(3/2)/2} - 1\right)^{1/2}} \quad (2.27)$$

For high soliton order this gives

$$z_{OWB} \propto \frac{L_D}{N} \quad (2.28)$$

While this result is heavily approximated, it has been shown to accurately predict the onset of optical wave breaking in Anderson et al. [53] and Finot et al. [54].

CHAPTER 3

Silicon Nitride Waveguides, Silicon Rich and Stoichiometric

3.1 Background

Many different materials have been used for supercontinuum generation in integrated waveguides. It is difficult to define a figure of merit for the materials, as waveguide platforms can be judged on several different parameters. CMOS compatibility, Kerr nonlinearity, linear loss, nonlinear losses, transparency window, dispersion management and $\chi^{(2)}$ [23]. Nevertheless a few different materials stand out. Perhaps the most obvious choice for optical waveguides is silicon. It was shown in the 1986, that optical waveguides using silicon could be fabricated in a CMOS compatible way. And thereby be easily integrated into the already existing production environment. Silicon waveguides have a high nonlinearity and low loss and seems like the ideal material. Early experiments in silicon waveguides at telecom wavelengths showed broadening, but were fundamentally limited by the low material bandgap, as this give rise to strong two photon absorption (TPA) and free carrier absorption (FCA) [24]. Several techniques have been employed to limit these effect. Most importantly, by using lasers with a pump wavelength above $2.1 \mu\text{m}$ the TPA and FCA can be reduced, and SC can be generated well into the MID-IR [25, 26]. Using this technique octave spanning SC frequency combs are generated with pulse energies as low as 16 pJ [55]. Another strong candidate for a waveguide material is AlGaAs. It has outstanding material properties [56]. But the III-IV materials are in general avoided in the CMOS fabrications lines as they serve as dopants for silicon. Recent work has shown SCG in AlGaAs with 3.6pJ energy, highlighting the very strong nonlinear effect of AlGaAs [57]. Chalcogenides have shown great promise, with their high nonlinear effect and low loss [58, 59]. The high refractive index allows for strong confinement. They

can furthermore have a extremely large transparency window in the IR, and could potential be used for very broadband mid-IR SCG [60]. Lithium Niobate is another extremely interesting material for SCG, as it has a strong $\chi^{(2)}$ effect. Initial work was done in bulk [61–63], but in recent years advances in fabrication has enabled f-2f self referencing and SCG using a single waveguide [64–70].

Silicon nitride is a CMOS compatible material, with relatively strong nonlinearity and low loss. Furthermore, because of its large bandgap, it does not suffer from two photon absorbtion. The most commonly used type of silicon nitride is stoichiometric Si_3N_4 . Previously, the main difficulty with Si_3N_4 was the appearances of cracks, when attempting to fabricate large waveguides, because of a large tensile stress [71]. This effect has been mitigated using advanced fabrication techniques [72–77], which in turn enabled the generation of SC at telecom wavelength and beyond [12, 28, 29, 31, 78–81]. Silicon rich nitride has several advantages compared to stoichiometric. It has a lower tensile stress, which enables one to fabricate larger waveguides without using any advanced fabrication techniques [82]. Furthermore, the increase in silicon content increases the nonlinear coefficient with as much as an order of magnitude more than Si_3N_4 [83]. It has been shown that an octave spanning SC can be generated in SiRN waveguides [33]. The main problem with SiRN is that the loss is higher than the loss of stoichiometric SiN [82]. Which has previously been a key limiting factor. Recently losses as low as 0.4 dB/cm has been observed [84].

3.2 Materials and fabrication

All waveguides in this thesis were fabricated at Chalmers University of Technology by my collaborator Zhichao Ye. Here a brief overview of the waveguide design and materials are presented. In later chapters, many different simulations will be presented. All simulations except for chapter 6 are made using the refractive index, linear loss and Kerr effect presented in this chapter.

Throughout this thesis both waveguides with a core material of Si_3N_4 and silicon rich nitride (SiRN) are used. In total three different silicon nitride compositions will be used. The two silicon rich compositions are indexed by the DCS:NH3 gas ratio used during fabrication, as in [82]. An increase in gas ratio corresponds to an increase in silicon content. This increases the nonlinear coefficient. The increase in gas ratio also lowers the bandgap, but no TPA is observed [82]. The height and width of the waveguide are crucial parameters for designing the dispersion. The height of the SiN film varies depending on the exact position of the waveguide on the wafer. Previous work has estimated the variance in height to 3%. This is important to take into account when designing waveguides, as small height deviations can severely change the character of the waveguide dispersion.

Figure 3.1(a) shows a schematic drawing of the waveguide, and the used materials. The waveguide consist of a bottom layer of thermally oxidized SiO_2 . Silicon nitride is deposited using LPCVD, with the DCH:HS gas ratio controlling the silicon content. The waveguide is patterned with DUV lithography and Electron beam lithography.

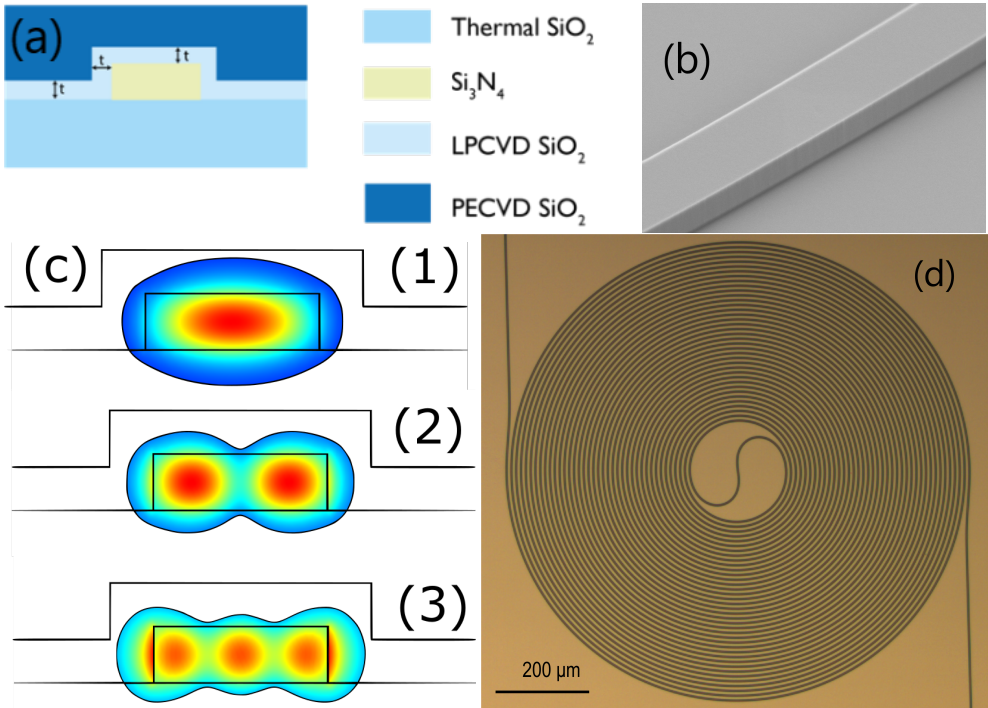


Figure 3.1: (a) Schematic drawing of the waveguide structure. (b) SEM image of a fabricated waveguide. (c) Normalized electric field of the three TE modes at 1550 nm. (d) Microscope image of a spiral waveguide.

The excess SiN is then removed with dry etching. An approximately 500 nm layer of LPCVD SiO₂ forms on top of the structure. Lastly the whole structure is clad in PECVD SiO₂. A SEM image of a fabricated waveguide is shown in figure 3.1(b). Figure 3.1(c) shows three TE modes at 1550 nm from in a 650nm by 2000nm waveguide. Usually no fourth order modes are found. The modes are found using Comsol Multiphysics. The HOM are neglected simulations of the SCG. The most noticeable effect of the HOM is that only 50% of the incoupled laser power seems to travel in the fundamental mode. This is especially clear when measuring on spiral waveguides, where the output power is only half that of a straight waveguide. This is believed to be caused by the increased bending loss in spiral waveguides for HOM. An example of a spiraled waveguide is shown in figure 3.1(d). The spiralling of the waveguide allows the 20 cm waveguides used in chapter 5 to be fabricated on a 1 cm long chip. The spiral waveguide is a larger and more complex structure to fabricated. Therefore, ad-

ditional problems can occur, such as coupling between modes or fabrication errors. In this thesis the need for longer waveguides are driven by need for more spectral broadening and to ensure that OWB can occur. This will be especially important when considering picosecond pump lasers. In Krückel et al. [82] a careful characterization is performed showing how increasing the silicon content lowers the stress of the SiN thin film, while increasing the nonlinear effect. It is further found that two compositions of SiN are optimal when using the nonlinear phase shift as a figure of merit. Si₃N₄ and SiRN8 were found to best, with SiRN3.9 being slightly worse. Increasing the silicon content to more than SiRN8 reduces the nonlinear phase shift. This relation is not based on any fundamental analysis of the different compositions. Optimization of the fabrication process, by introducing an annealing process have significantly lowered the loss in SiRN3.9 making it significantly better [84]. Additionally, the loss has been lowered by an order of magnitude in Si₃N₄ waveguides [34]. The loss and kerr effect of the three types of silicon nitride, used as a core material, are seen in table 3.1 The nonlinear effect was measured using a dual continuous wave laser experiment [82]. The loss was measured using optical frequency domain reflectometry or by cutback measurements. While the nonlinear phase shift is a useful figure of merit it is not sufficient to characterize the materials use for SCG. It will be seen in chapter 4 that most anomalous dispersion waveguides generate the SC after 1-3 cm of propagation. Further propagation mostly introduces additional noise. Therefore, low loss waveguides are mainly useful if a limited amount of input pulse power is available. It is nonetheless clear that if long waveguides are necessary, the low loss of Si₃N₄ makes it the obvious choice. One example of this is shown in chapter 5, where long Si₃N₄ are used to generate SCG. It is numerically shown that if longer input pulses are used, the waveguides must be similarly longer.

For increasingly demanding waveguide designs, it is necessary to accurately predict the dispersion of the fabricated waveguides. To this end, it is necessary to know the refractive index of each of the materials used. The refractive index of thin films of the various materials was measured using ellipsometry by J.A Woolam. The refractive index was measured from 0.2 μ m to 30 μ m. For clarity only the refractive index from 0.8 μ m to 5 μ m is plotted in figure 3.2. It is seen that varying the silicon content drastically changes the refractive index of the core material. Additionally, a significant difference is seen between the different cladding materials. To get an estimate of the influence of the core material on the waveguide dispersion. Using Comsol Multiphysics, a simulation of a waveguide with height 650nm and width 2000nm is

	Si ₃ N ₄	SiRN3.9	SiRN8
α [dB/cm]	0.04	0.4	1.5
n2Kerr [m ² /W]	2.4e-19	5e-19	6e-19

Table 3.1: Loss(α) and nonlinear refractive index(n2Kerr) for SiN with different silicon content. SiRN are indexed by the DCH:HS gas ratio during fabrication [82] .

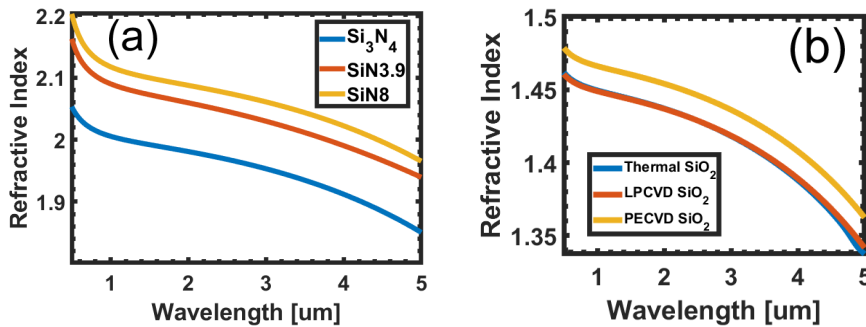


Figure 3.2: (a) Refractive index of the core materials. (b) Refractive index of the cladding materials.

performed for each of the three core materials. All waveguide simulations in the thesis are simulated over the full wavelength range of the expected SC using the measured refractive index for all wavelengths. Some care has to be taken when doing broad wavelength sweeps, as any small fluctuations in refractive index can make it difficult for Comsol to correctly identify the modes. The model is solved for a large number of modes, that are then sorted using both the mode refractive index. An overlap with the electric field in the x direction and y direction is also calculated to ensure that the TE and TM modes are correctly identified.

In figure 3.3 it is observed that the main effect of increased refractive index due to increased silicon content, is the tilting and red shifting of the dispersion profile. In the inset, it is observed that as the silicon content increases, the minimum dispersion wavelength moves towards the red wavelength. Interestingly, there is no clear change in behaviour of the dispersion at 1550 nm, when the silicon content is increased.

3.3 Summary

Silicon nitride has shown great promise as a material platform for SCG in waveguides. In this chapter, the waveguide structure is presented, with the refractive index of all the used materials included. The refractive index is measured over a broad wavelength range, easily covering the range of wavelengths examined in this thesis. Furthermore, the Kerr coefficient and loss of three different silicon nitride compositions are shown. Recent results in fabrication has lowered the loss of the Si_3N_4 and $\text{SiRN}3.9$ waveguides. These low losses makes it feasible to use longer waveguides for SCG. Very long straight waveguides are practically not feasible so a spiral waveguide is used. It is observed that an increase in silicon content can modify the dispersion profile of the fabricated waveguides significantly.

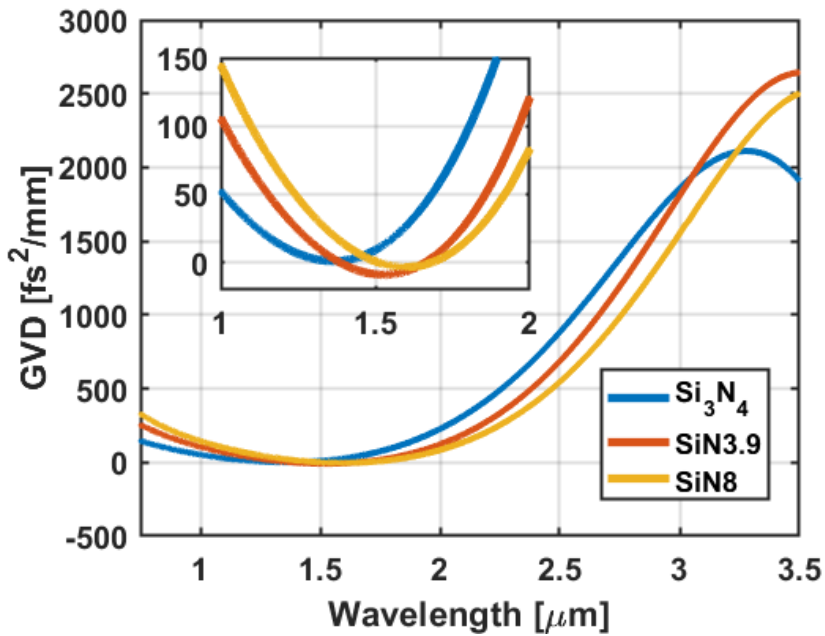


Figure 3.3: GVD for 650nm by 2000nm waveguide, with the core material Si_3N_4 (Blue), $\text{SiN}_{3.9}$ (Orange) and SiN_8 (Yellow). Inset is a zoom in of (a) to show the behaviour around 1550 nm.

CHAPTER 4

Anomalous Dispersion Supercontinuum in Silicon Rich Silicon Nitride Waveguides

4.1 Background

Supercontinuum generation at MID-IR wavelengths is especially relevant for molecular spectroscopy as the vibrational modes of most molecules are in this region. Additionally, coherent light sources in the infrared are limited and are usually bulky and expensive. For on-chip waveguides, the concept of frequency comb spectroscopy has been a major focus. A key requirement for frequency comb spectroscopy is to have a coherent broadening process. This can be achieved in an anomalous dispersion waveguide by restricting pulse width and propagation length. In the pursuit of generating coherent light at longer wavelengths, dispersion engineering has been one of the main techniques. By engineering the dispersion, the phase matching condition of DWs can be adjusted, and the wavelength can be controlled. Most dispersion engineering has been performed by adjusting the waveguide dimensions, thereby influencing the waveguide dispersion. Early results in Si_3N_4 waveguides have shown large amount of broadening in the visible to $2.5 \mu\text{m}$ region [28–30]. It has been shown that f - $2f$ can be performed at relative low power [12]. A recent landmark result have shown DWs generated in 2.5 to $4 \mu\text{m}$ range, when pumped using a 1550 nm laser [31]. Moving to longer pump wavelengths is another way of generating wavelengths further into the infrared [79]. Here conversion efficiencies of 35% has been achieved [81]. Finally more advanced mode dispersion engineering techniques have been performed by exploiting the increased dispersion control available when pumping in the coupled mode of a dual core waveguide system [80]. In a silicon rich nitride waveguide an 1.5 octave spanning supercontinuum was generated from 820nm – 2250nm [33].

4.2 Dispersive wave control using material and waveguide dispersion

In SiRN Liu et al. [33] predicted and modelled that by adjusted the height of the waveguide the DW could be tuned far into the MID-IR. It was then experimentally shown in Si_3N_4 waveguides [31]. Similarly here, the influence of waveguide height and width is investigated, but more importantly, modifying the silicon content of SiN as a tuning parameter is examined, and compared to the influence of the waveguide dimensions. More specifically, a numerical study of the dispersive wave phase matching for different silicon nitride compositions and waveguide dimensions is performed. The phase matching calculations are confirmed using SCG simulations of the waveguides with the GNLSE as seen in chapter 2. Finally, the SC of two waveguides with different core materials are experimentally investigated. As shown in chapter 3, increasing the silicon content of SiN increases the nonlinear coefficient, and linear loss. It is also shown that the refractive index of SiN depends on the silicon content. The dispersion profile of the waveguides are simulated using the material refractive index and waveguide model shown in chapter 3. The dispersive wave frequency is calculated using eq 2.16. Three types of SiN are investigated, stoichiometric Si_3N_4 , SiRN3.9 and SiRN8. Dispersive waves are a result of the soliton dispersion allowing phase matching, therefore to achieve any dispersive wave phase matching, it is necessary to have anomalous dispersion. Figure 4.1 shows the GVD at 1550 nm for the TE mode of the waveguide, with a core material of Si_3N_4 (a), SiRN3.9 (b) and SiRN8 (c). The height is swept from 640nm to 800nm, and width from 1400nm to 3000nm. Si_3N_4 waveguides have the most positive GVD at 1550nm. The SiRN3.9 waveguides have an increased silicon content and show an overall more negative dispersion for all waveguide sizes. Interestingly, this trend reverse when going to the SiRN8 waveguides, where the GVD increases when compared the SiRN3.9. Therefore no simple relation between the silicon content and the GVD 1550nm can be seen. All waveguide materials see a similar behaviour when considering their height and width. Small height and large widths gives the most positive dispersion, while large height and small width gives the most negative dispersion. Based on the small change in dispersion between the two SiRN waveguides, and the similar dispersion in terms of height and width, one might suggest, that silicon content has limited influence on the dispersive wave phase matching. To examine this, the phase matching wavelength of the waveguides were calculated. Figure 4.2 shows the long wavelength phase matching wavelength for Si_3N_4 (a), SiRN3.9 (b) and SiRN8 (c). The zeroes indicate waveguides with normal dispersion at 1550 nm, and therefore no dispersive waves.

The dispersive wave map of Si_3N_4 shows a tuneability of the long wavelength dispersive wave from 1.6 μm to 3.4 μm . The height is observed to be to be a very important parameter. An example of this is the tuneable range of the 740 nm high waveguide, which goes from 2.1 μm to 2.6 μm , while for the slightly higher 800 nm waveguide, the tuneability is from 2.5 μm to 3.4 μm . The SiRN3.9 waveguide shows dispersive waves from from 1.9 μm to 4.1 μm . The tallest waveguide is observed to

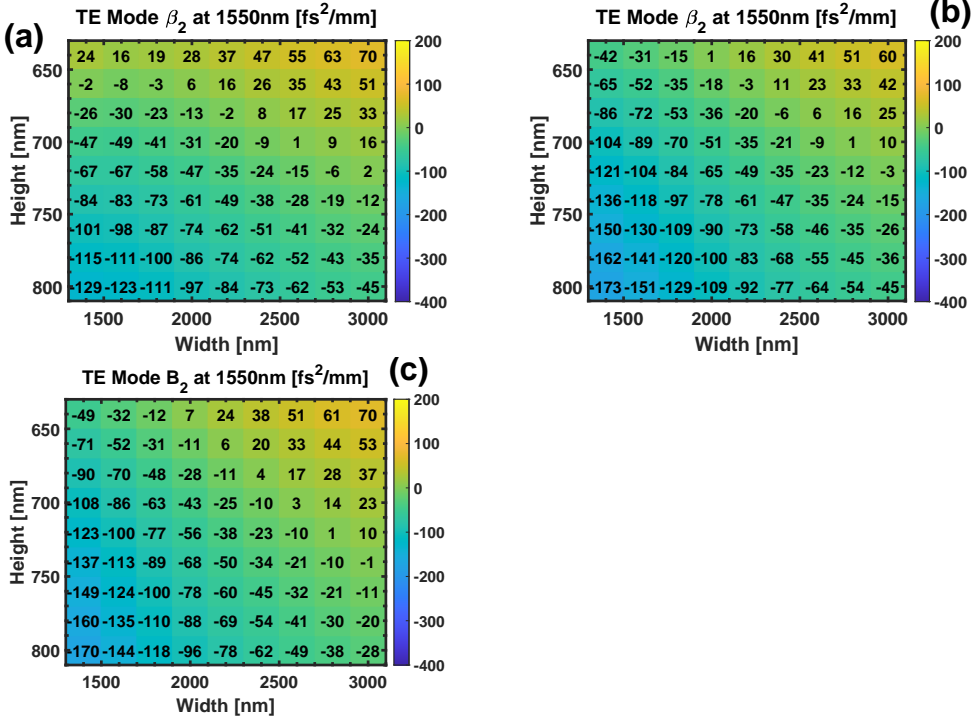


Figure 4.1: GVD for waveguides of varying height and width. (a) Si_3N_4 as core material (b) SiRN3.9 as core material. (c) SiRN8 as core material.

have the longest wavelength dispersive wave at $4.1 \mu\text{m}$ with a tuneability from $3 \mu\text{m}$ to $4.1 \mu\text{m}$. Now the SiRN8 dispersive wave phase matchings are considered. Here, it is observed that the longest phase matching wavelength is $5.2 \mu\text{m}$. The phase matching ranges from $3.3 \mu\text{m}$ to $5.2 \mu\text{m}$ when varying the width of the 800nm waveguide. Based on this it is seen that for these waveguide dimension, the increase in silicon content increases the possible wavelength of the dispersive wave. The difference between dispersive wave wavelength from the lowest silicon content Si_3N_4 and highest SiRN8 is $1.8 \mu\text{m}$, which is equivalent to the maximum tuneability of the Si_3N_4 waveguide, when adjusting height and width. A few general things can be noted, the largest waveguides generate the longest wavelengths. While this is not true for all height, and would probably also not be true if larger width were included, it is noteworthy that the trend is towards taller and wider waveguides. It is also interesting to consider what material has the largest range of wavelengths. If the wavelength range of the tallest waveguide is compared between the three waveguide materials, the following can be observed. The Si_3N_4 waveguide can be tuned for $0.9 \mu\text{m}$ from $2.5 \mu\text{m}$ to $3.4 \mu\text{m}$, the SiRN3.9 waveguides wavelengths range $1.1 \mu\text{m}$ from $3 \mu\text{m}$ to $4.1 \mu\text{m}$, and

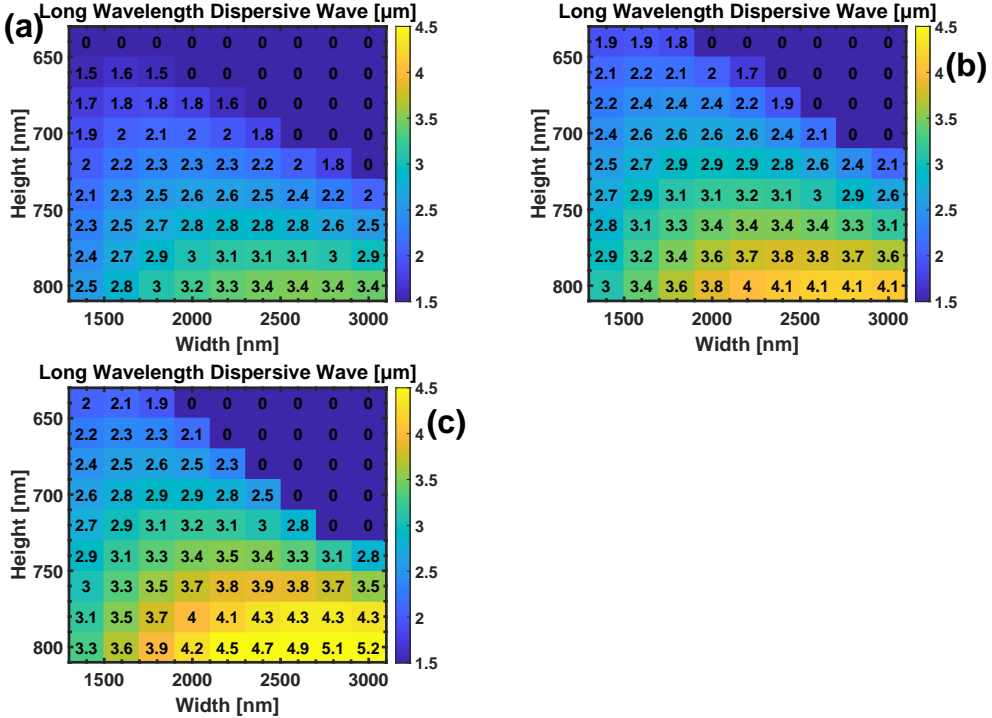


Figure 4.2: Phase matching wavelength of the long wavelength DW. (a) Si₃N₄ as core material, (b) SiRN3.9 as core material. (c) SiRN8 as core material.

for the SiRN8 waveguide the range is $1.9\mu\text{m}$ from $3.3\mu\text{m}$ to $5.2\mu\text{m}$. This is quite interesting, as it shows how changing the material composition can change the range of wavelengths which can be phase matched using dispersion engineering via height and width. Perhaps a last thing to note based on these figures is that by adjusting the material composition, a wavelength change from $3.4\mu\text{m}$ to $5.2\mu\text{m}$ is seen, which is similar to changing the width of the 800 nm high SiRN8 waveguide from 1400nm to 3000nm. This highlights the fact that by adjusting the silicon content, dispersion engineering with similar strength as adjusting waveguide dimensions is achieved. As the waveguides have two ZDW, an additional dispersive wave is predicted on the short wavelength side of the anomalous dispersion region. The resulting phase matching wavelengths are shown in figure 4.3 for Si₃N₄(a), SiRN3.9(b) and SiRN8(c).

For the Si₃N₄ waveguides, phase matchings from $0.5\mu\text{m}$ to $1.1\mu\text{m}$ are seen. The SiRN3.9 waveguides dispersive wave wavelengths are slight redshifted. With an effect of around 100nm. Similarly, the SiRN8 seem to have around 200nm redshift in comparison to the Si₃N₄ waveguides. This indicates that Si₃N₄ is better for generating short wavelength dispersive waves. These dispersive wave maps are calculated based

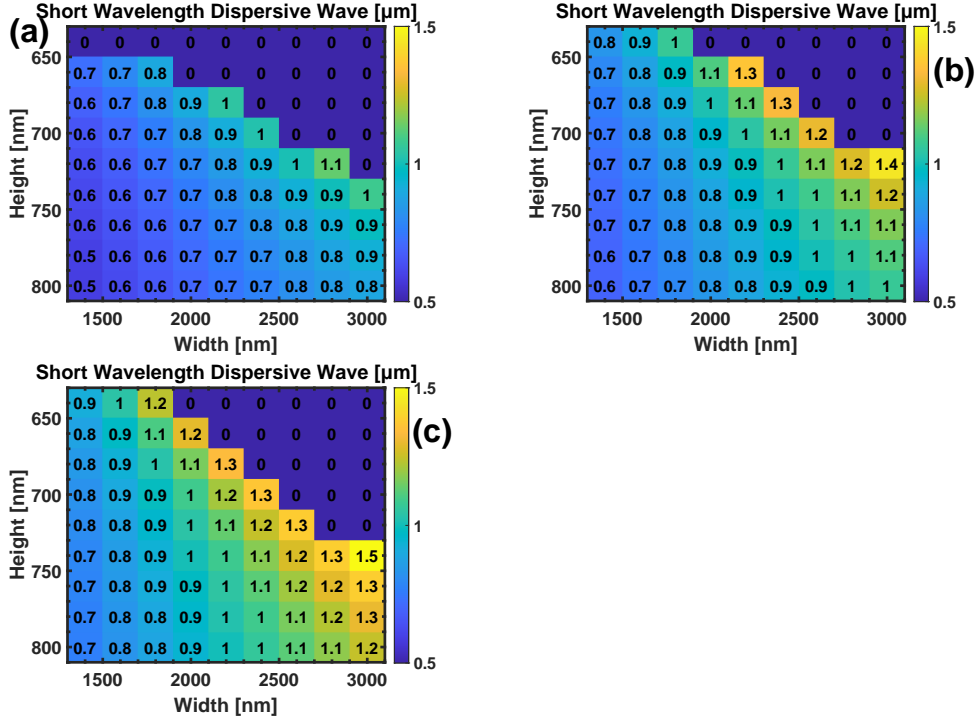


Figure 4.3: Phase matching wavelength of the short wavelength DW. (a) Si_3N_4 as core material, (b) SiRN3.9 as core material. (c) SiRN8 as core material.

on the simulated dispersion profile of the waveguide. But both loss and nonlinear coefficient changes as the silicon content is increased. The phase matching conditions gives no information on the necessary experimental conditions. To show the validity of the predictions, a GNLSE simulation is done for the waveguide with a height 800 nm for all three materials, with five different width. All simulations are performed with the simulated dispersion and effective area. A 50pJ pulse energy is used, and the input pulse is a transform limited 121fs gaussian pulse. The waveguide length simulated is 2cm. Figure 4.4(e,f) shows the results for the Si_3N_4 waveguides and their phase matching. As predicted the dispersive wave starts at $2.5\mu\text{m}$ and moves to $3.4\mu\text{m}$. All simulations fit well with the respective phase matching calculations. Only two waveguides generate dispersive wave on the short side. This is caused by the lack of overlap with the broadened soliton.

Figure 4.4(c,d) shows the simulated SC of a SiRN3.9 waveguide with a height of 800nm, and a width from 1400 nm to 3000nm. The supercontinuum has two dispersive waves, with the short wavelength dispersive wave moving from $1\mu\text{m}$ to $0.7\mu\text{m}$, while the long wavelength DW can be tuned from $3\mu\text{m}$ to $4\mu\text{m}$. The phase matching

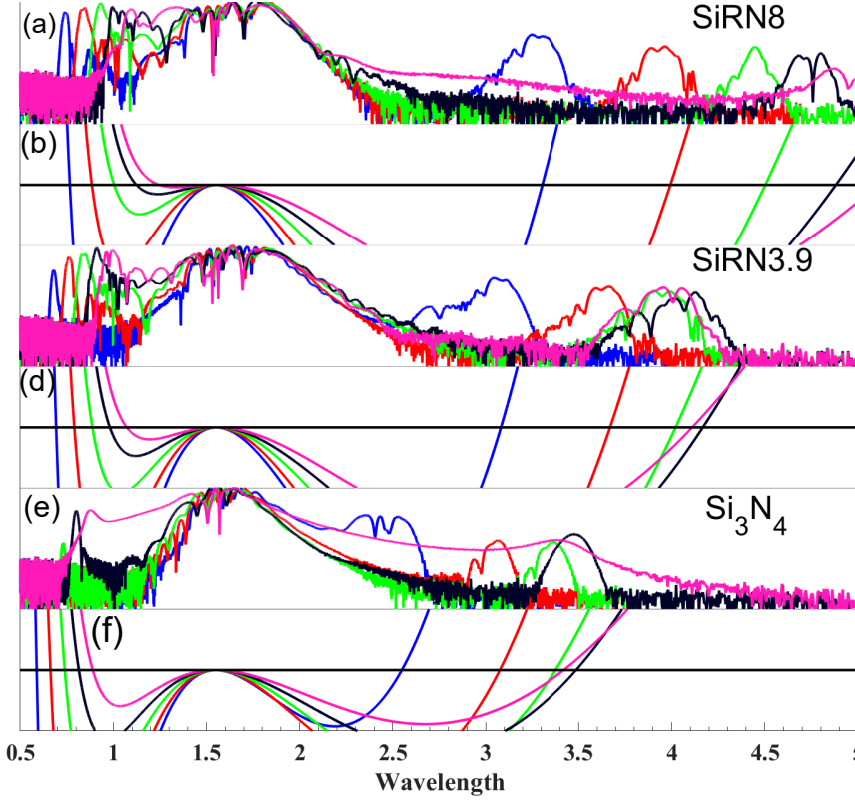


Figure 4.4: (a,c,e) Simulated supercontinuum from SiN waveguides with height 800nm and width 1400nm (Blue), 1800nm (Red), 2200nm(Green) 2600nm (Black) and 3000nm (Pink). 50pJ pulse energy, input pulse width is 120fs,waveguide length is 2cm. (b,d,f) Dispersive wave phase matching conditions of the waveguides. Phase matching occurs as the horizontal black is crossed.

conditions in Figure 4.4(d) show perfect agreement with simulation. The core material is then changed to SiRN8, and the simulations are rerun with all other parameters being the same. The result is seen in figure 4.4(a,b).

As expected, it is observed that the short wavelength dispersive waves are relatively unaffected by the change in material. On the other hand, the tuning of the dispersive wave from $3\ \mu\text{m}$ to $5\ \mu\text{m}$ is observed for the Mid IR dispersive wave. It is clear from these simulations that the previous dispersive wave calculation show good agreement with the GNLSE simulations. Furthermore, this allows the conclusion that the dispersive waves can be generated with realistic parameters in terms of pulse

width, waveguide length and pulse energy. Based on the phase matching calculations and the GNLSE simulation, it is concluded that adjusting the material dispersion is a powerful tool for dispersion engineering, when generating radiation in the Mid IR. A final illustration of this shown in figure 4.5. Where the DW phase matching for a 800nm by 3000nm waveguide is shown for the three different materials. This highlights that the DW phase matching can be tuned from 3.4 μm to 5.2 μm using only the silicon content of the core material.

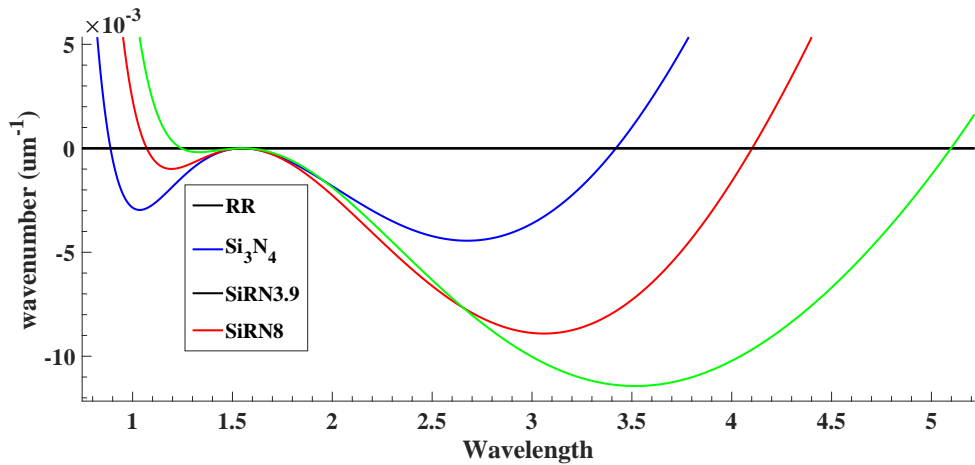


Figure 4.5: Phase matching condition of soliton dispersive waves in a 800nm by 3000nm waveguide for three different SiN compositions. The long wavelength DW tunes from 3.4 μm to 5 μm .

4.3 Experimental result

Here, measurements of SC from two waveguides with a length of 2.3cm are presented. One with a guiding material of SiRN3.9 and one with SiRN8. These experimental results serve as both a way of examining the validity of our numerical results, and as a way to discuss a few possible problems with the waveguides. The experiment works as follows: A 121 fs laser, with an average power of 280mW and a repetition rate of 90MHz, is coupled into the waveguide using a telescope and an aspheric lens. The image on the frontpage shows an example of the waveguide when generating SC. The polarization of the laser beam is adjusted to the TE mode of the waveguide using a halfwave plate. The coupling is optimized using 3D stages. The spectrum is recorded with an OSA. The incoupling efficiency to these waveguides were very low, with only

4.5 mW (50pJ) ending up in the fundamental mode. This is based on the measured output power and estimated loss of similar waveguides.

The first waveguide is a 640nm by 1750nm waveguide with a SiRN3.9 core. Based on results from the previous section, the waveguide should be anomalous dispersion at 1550nm. Dispersive waves are predicted at 1.1 μm and 1.9 μm . Figure 4.6 shows the measured supercontinuum(a), the simulated SC(b) and phase matching(c). The

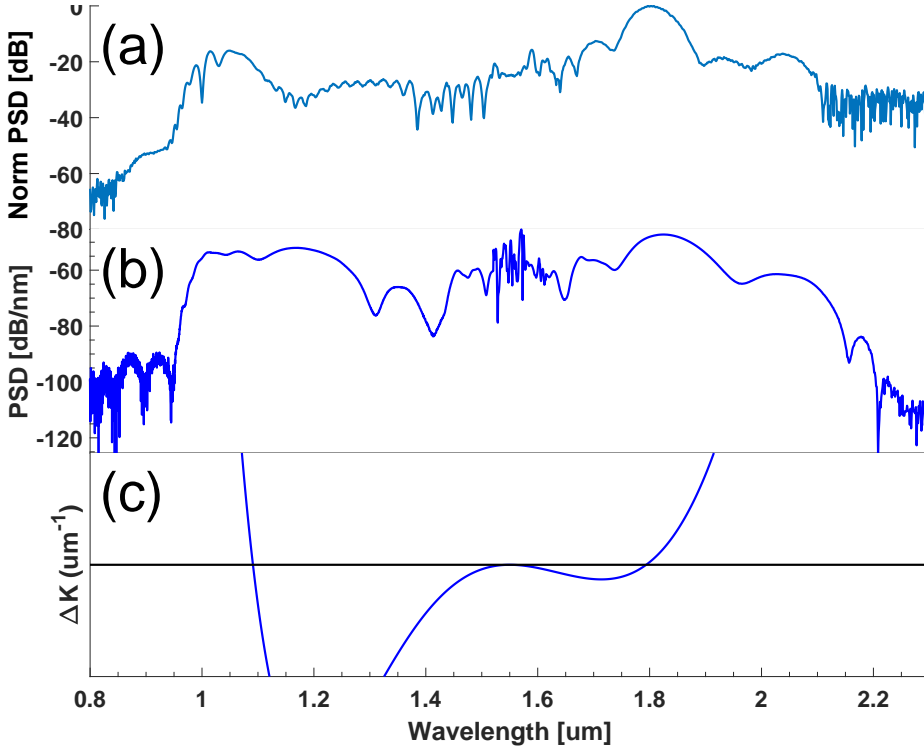


Figure 4.6: Supercontinuum from 640nm by 1750nm SiRN3.9 waveguide. The pulse energy in the waveguide was 50 pJ. (a) Experimentally measured SC(b) Simulated SC (c) Dispersive wave phasematching.

experimentally measured SC seems in good agreement with the the simulated SC in terms of bandwidth and shape. In both significant broadening is observed after the phasematching conditions at 1.1 μm and 1.9 μm . The SC extends from 1 μm to 2.1 μm covering an octave.

The second waveguide is a 700nm by 2150nm waveguide with a SiRN8 core. Based on results from the previous section, the waveguide should be anomalous dispersion at 1550nm. Dispersive waves are predicted at 1.1 μm and 2.8 μm

The measured SC is shown in figure 4.7(a). A dispersive wave is observed at 1 μm ,

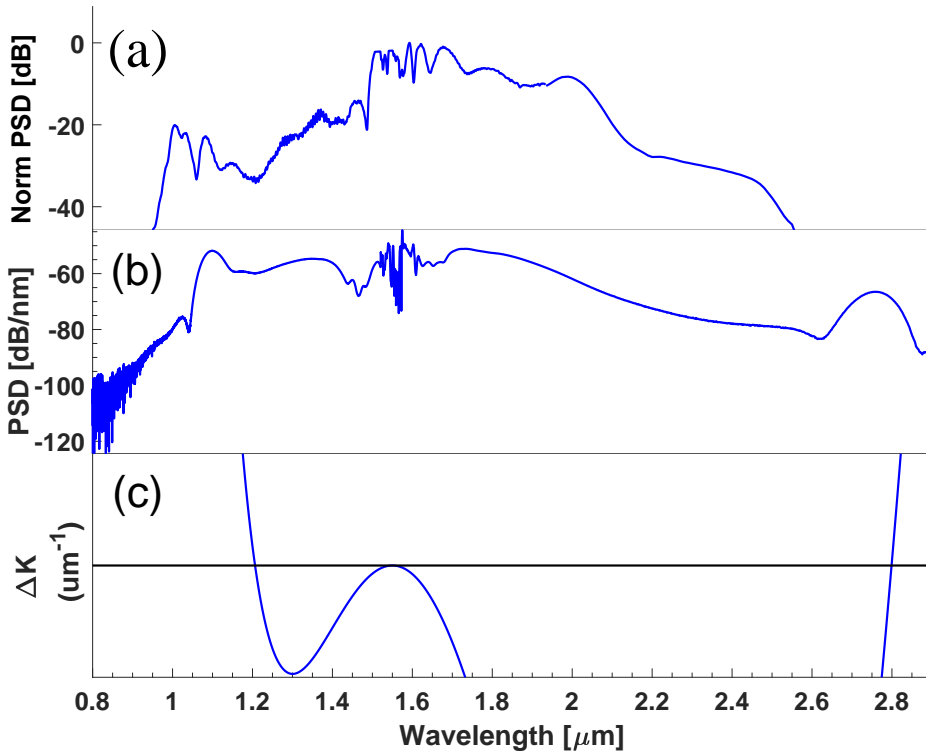


Figure 4.7: Supercontinuum from 700nm by 2150nm SiRN8 waveguide. The pulse energy in the waveguide was 50 pJ. (a) Experimentally measured SC (b) Simulated SC (c) Dispersive wave phase matching.

but no spectrum is observed beyond 2500nm. In comparison to the simulated SCG, it is clear that the dispersive wave at $2.8 \mu\text{m}$ is missing. Otherwise the spectrum is similar. With a dispersive wave at $1\mu\text{m}$ and the spectrum falling off towards $2.5\mu\text{m}$. Finally, it is observed that the differences between maximum spectrum and the dispersive waves are bigger than in simulation. This implies a strong wavelength dependent loss in the waveguide or outcoupling. A few reasons can explain the lack of a dispersive wave at $2.8 \mu\text{m}$. One explanation is that deviations in dispersion from the designed waveguide dispersion can shift the DW phase matching further into the MID-IR, lowering the efficiency of the DW generation. This in turn would make it more difficult to detect. Previous reports show a fabrication variation of around 3%, corresponding to 20nm variation in height. Combining this with the dispersive wave maps in figure 4.2(c), one should expect the DW from $2.6 \mu\text{m}$ to $3.1 \mu\text{m}$, which is easily inside the measurement range, and should be measurable. Furthermore, simulations in figure 4.4 show similar conversion efficiency for the different phase

matching wavelengths using realistic parameters. Another reason for the lack of a MID-IR DW could be a strongly wavelength dependent outcoupling loss, which coupled with low detector efficiency makes it difficult to measure the DW. Similarly a high loss at the MID-IR wavelengths in the waveguide, because of low confinement or material absorption, would make it difficult to generate and measure the DW.

4.3.1 Noise

For most applications the noise of the generated supercontinuum is vital. One way of quantifying the noise is the first order spectral coherence as given by

$$g_{12}^{(1)}(\omega) = \frac{|\langle E_j^*(\omega)E_i(\omega) \rangle|}{\sqrt{\langle |E_j(\omega)|^2 \rangle \langle |E_i(\omega)|^2 \rangle}}, i \neq j \quad (4.1)$$

where E_i and E_j are two different pulses. Another way to characterize the noise is the relative intensity noise (RIN). The RIN is a measure of the pulse to pulse intensity fluctuation in a given bandwidth. Here, RIN and coherence are simulated for the two waveguides used in the experiment. The simulations are performed using only quantum noise (QN) and including both (QN) and a 1% fluctuation of the input pulse power. Figure 4.8 shows the simulated coherence(a) and RIN(b) for the 640nm by 1750nm SiRN3.9 waveguide. If only QN is included in the simulation, the coherence is close to one for all wavelength. The coherence is also good for the case with QN and RIN included, but it is clear that including the 1% laser noise degrades the coherence slightly. The differences between QN and QN +1% fluctuations is much more pronounced in the RIN. Based on these simulations, it is clear that a good coherence is expected, but the RIN approaches 5% for most wavelengths. Figure 4.9 shows the simulated coherence(a) and RIN for the 700nm by 2150nm SiRN8 waveguide. Again the coherence is essentially one if only the QN is included. If the laser noise is included a clear drop in coherence is observed. In RIN a similar behaviour is seen, including the laser noise increases the simulated RIN significantly at all wavelengths. From these simulations, it is clear that it is necessary to take the intensity noise of the laser into account when simulating the noise properties of the SC. The effect is observed for both coherence and RIN, but especially the increase in RIN is significant. It is also apparent that regions with high RIN has lower coherence and vice versa. Further study of the RIN in SCG in different waveguides is performed in chapter 5.

4.4 Summary

In this chapter, numerical analysis of the phase matching conditions of silicon nitride waveguides with various silicon content and waveguide dimensions has been performed. It is shown that for the waveguide dimensions investigated, the phase

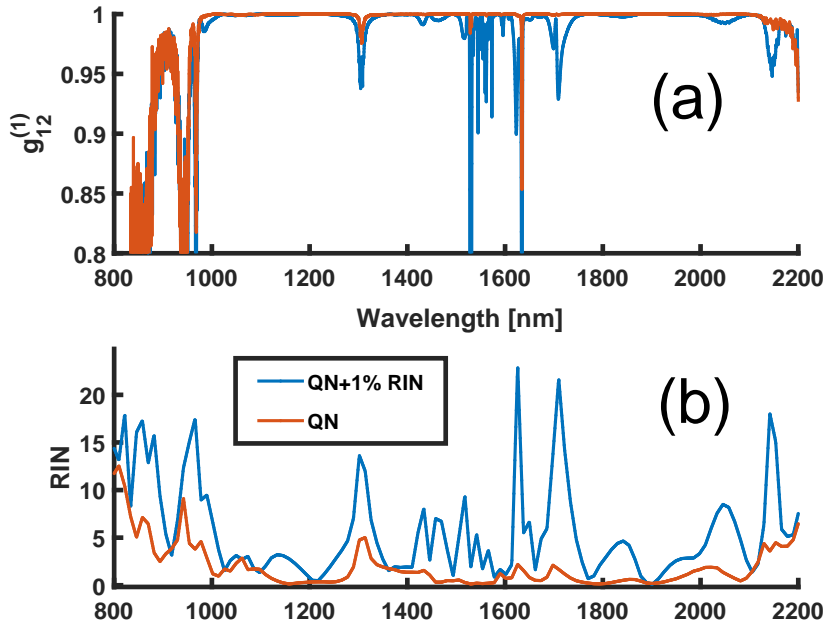


Figure 4.8: Simulated noise of supercontinuum generated in 640nm by 1750nm SiRN3.9 waveguide. (a) Coherence. (b) RIN.

matching conditions can be changed from a maximum of $3.4 \mu\text{m}$ in Si_3N_4 , to $4.1 \mu\text{m}$ in SiRN3.9, to $5.2 \mu\text{m}$ in SiRN8. This shows how adjusting the material content can potentially allow generation of dispersive waves further into the Mid IR. Comparing the influence of waveguide height and width to the material content shows that adjusting the core material is equally as effective. GNLSE simulations agree with the predicted phase matching conditions and show dispersive wave generation with a 50 pJ, 120fs gaussian pulse in a 2cm waveguide. Two 2.3 cm long waveguides, with different silicon content, were tested experimentally. Octave spanning supercontinuum was achieved in both SiRN3.9 and SiRN8 waveguides. The waveguide using SiRN3.9 generated an octave from $1 \mu\text{m}$ to $2 \mu\text{m}$, which is in good agreement with the predicted bandwidth. The SiRN8 sample with a height of 700 nm and width of 2150nm generated broadening from $1 \mu\text{m}$ to $2.5 \mu\text{m}$. but there was no sign of the predicted dispersive wave at $2.8 \mu\text{m}$. Based on this it is concluded that the waveguide loss at higher wavelengths could be an important parameter to investigate in regards to MID-IR generation. Additionally, further work should be done on optimizing out-coupling efficiency at long wavelengths. Simulations show that the generated SC should be

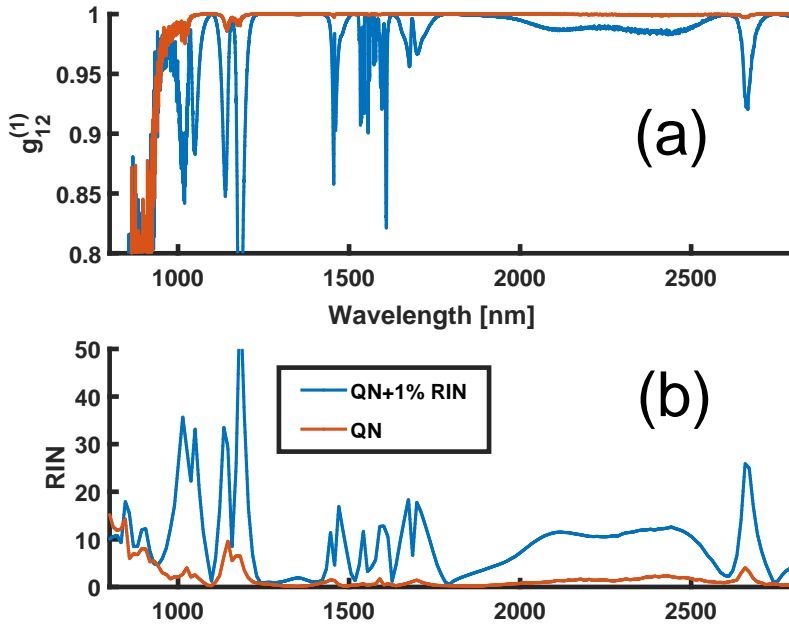


Figure 4.9: Noise of supercontinuum generated in 700nm by 2150nm SiRN8 waveguide. (a) Coherence. (b) RIN.

coherent. The importance of including the technical noise of the laser is highlighted. And it is shown that fluctuations in the RIN can be expected, even for reasonably high coherence.

CHAPTER 5

All Normal Dispersion Supercontinuum in Stoichiometric Silicon Nitride Waveguides

5.1 Introduction to all normal dispersion supercontinuum generation

5.1.1 Background

The generation of supercontinuum has received much attention in the last two decades. The interest in supercontinuum mainly stem from the introduction of the photonic crystal fibers [47]. Applications have been found in many areas. Perhaps most well known is the Nobel prize in physics in 2005 in optical frequency metrology. In the last decade, the field of on-chip supercontinuum has been heavily researched. Especially with the focus of generating broadband supercontinuum for f-2f self referencing [55, 85]. As discussed in chapter 4 many interesting results have been obtained. Previous on-chip SC has been focused on anomalous dispersion, which enables broadband tunable SC. But it suffers from two major problems. It has a complex temporal and spectral shape with large sections of spectrum and time with limited energy. This can be a limiting factor in applications such as pulse compression where a flat spectrum with a linear phase is ideal. Furthermore, anomalous dispersion supercontinuum can only retain low noise for very specific combinations of pulse width, propagation length and input power. These problems have also been encountered in PCF. Where all normal dispersion fiber has been investigated as a solution [86]. The first demonstration of octave spanning supercontinuum in ANDi fiber was a scientific breakthrough [87–89], and has enabled the use of SC in many areas where low noise

is a necessity [51, 90]. Careful study of the ANDi supercontinuum have identified key concepts such as optical wave breaking [54], the influence of Raman and polarization on noise [91]. ANDi fiber have shown great flexibility generating UV radiation [92] or supercontinuum spanning from 1.7 to 10 μm [93]. The use of all normal on-chip waveguides have nonetheless never been carefully studied. Frequency comb generation in ring resonators with normal dispersion has been a recent topic of investigation. But in straight waveguides mostly numerical work has been done [94, 95]. Very recently, ANDi SCG has been shown experimentally in both a Chalcogenide and a SiGe waveguide [96, 97]. Nevertheless, both of these experiments were done using pump laser at 4 μm . And no experimental results regarding the noise was obtained. Pumping in the normal dispersion region was also done in Liu et al. [33]. But here the waveguide had anomalous dispersion relatively close to the pump.

5.1.2 Motivation

In chapter 4 I presented a few results based on anomalous supercontinuum generation. This use of anomalous dispersion waveguides for supercontinuum has enabled low pulse energy octave spanning supercontinuum. Recent experiments have shown good noise performances in self frequency referencing, especially because of the decreased influence of Raman compared to fiber based supercontinuum [50]. On-chip anomalous dispersion SCG relies on two main mechanism to generate broadband spectrum, soliton fission and dispersive wave generation. But with these effects come several disadvantages. The complex temporal shape after soliton fission in general introduces a large amount of nonlinear interactions, which limits low noise supercontinuum to the soliton fission point. Therefore only an optimized peak power can be used for any specific waveguide length. Furthermore, the modulation instability present in anomalous dispersion limits the input pulse to below 150fs [35]. Finally, a key broadening mechanism in anomalous dispersion is dispersive waves, which are controlled by the solitons phase matching condition. Generally the resulting spectrum will have at least two large dips in the supercontinuum at the regions inbetween the soliton and the DW phase matching. Different schemes have been used to resolved these issues, mainly using more complex dispersion profiles, such as tapering the waveguide to continuously shift DW phase matching [98, 99], or using the supermodes of dual core waveguides [80]. A different solution to all three problems is well known in fiber based SCG. Namely the use of all normal dispersion fibers. Here, I present the use of a all normal dispersion waveguide, and evaluate its effect on all three problems. The broadening in ANDi waveguides is caused by self phase modulation and optical wave breaking and does not rely on any phasematching conditions. The key benefits from ANDi based supercontinuum are low noise for large input powers, long propagation length and long input pulse. On top of that it provides a smooth spectral and temporal shape that is easier to compress. To the best of our knowledge, this work demonstrates the first experimental verification of supercontinuum at telecom wavelengths in an ANDi nanophotonic waveguide characterising both dispersion and

noise properties.

In the following I will present SCG in ANDi waveguides based on a simple rectangular waveguide design. An optimized waveguide is designed, and supercontinuum based on all normal dispersion is generated. The waveguide was fabricated with a spiral design to enable 20 cm of propagation on a 1 cm chip. The long waveguides are only feasible because of the low loss of the Si_3N_4 waveguides. The spectrum and the wavelength dependent relative intensity noise are compared to SC generated in an anomalous waveguide. The spectrum and relative intensity noise in shorter straight waveguides are also compared. Here three kinds of waveguides are investigated, ANDi, anomalous, and a waveguide pumped almost directly on the zero dispersion wavelength. Finally, the influence of the Raman effect, and the pulse width of the input pulse is numerically examined.

5.1.3 Fundamental effects, and the influence of waveguide parameters

Based on the work in ANDi fibers, a few design criteria can be inferred for ANDi waveguides. The spectrum initially broadens because of self phase modulation. Disregarding dispersion the bandwidth of the SPM can then be estimated by $|\Delta\omega_{SPM}(z, t)| = \gamma P_0 \frac{\partial U(t)}{\partial t} z$ [48] as in chapter 2. As the bandwidth of increase because of SPM, the influences of dispersion becomes important. As the edges of the pulse steepen optical wavebreaking occurs. The distances for optical wave breaking can be estimated by $z_{OWB} = L_D/N = T_0 \sqrt{\frac{\gamma P_0}{|\beta_2|}}$ [54]. Now using that the maximum of $\frac{\partial U(t)}{\partial t} = 1/T_0$ the following expression can be derived $|\Delta\omega_{SPM}(z_{OWB})| \propto \sqrt{\frac{\gamma P_0}{|\beta_2|}}$. A few things can be concluded from this equation. The broadening can be improved by either increasing the peak power of the pulse, using a waveguide with higher nonlinearity or by lowering the dispersion of the waveguide. Furthermore, the flatness of the dispersion profile of the waveguide limits the achievable broadening. As the dispersion increases, the necessary power increases, and it becomes unfeasible to generate new wavelength. The spectral broadening caused by optical wave breaking is proportional to the broadening caused by SPM and will therefore follow a similar dependence.

Both soliton dynamics and modulation instability are suppressed in the ANDi dispersion regime. But two noise contribution exists. Polarization modulation instability (PMI) and Raman gain. PMI occurs as FWM phasematched between two weakly birefringent modes. PMI is completely suppressed because of the large propagation constant differences between the two polarization modes in the waveguide [100, 101]. In contrast to PCF, the rectangular waveguide structure is inherently strongly birefringent. It requires no further design to make the TE and TM modes nondegenerate. The Raman gain of silicon nitride is in general not well documented, and is commonly neglected. Experiments in fiber suggest that the Raman gain can be ignored until around 500fs pulses. A numerical investigation of this effect in waveguide will be performed at the end of this chapter. Finally, as the SCG in ANDi waveguides

does not benefit from soliton compression, which compresses the input pulses. It can require more input power and longer lengths of waveguide. Therefore, the loss of the waveguide becomes vital for the supercontinuum generated. This is especially true, when using longer input pulses, as the z_{owb} scales linearly with the pulse width. Based on these consideration we can conclude that to generate a broad supercontinuum in an all normal dispersion waveguide, it is necessary to have a close to zero dispersion, and preferably over a large bandwidth. The waveguide loss should be low, to ensure sufficient length for OWB and a rectangular waveguide ensures birefringence, thereby suppressing PMI. To find a waveguide with low dispersion around 1550nm and low dispersion over a large bandwidth Si_3N_4 waveguides are simulated at different height and widths to find the most suitable waveguide dimensions. Figure 5.1 shows the GVD at 1550nm for waveguides with different height and width. Figure 5.2 shows how much of the dispersion is below $100\text{fs}^2/\text{mm}$ given as a fraction of an octave. This quantifies the region in which the spectrum can be expected to continue to broaden.

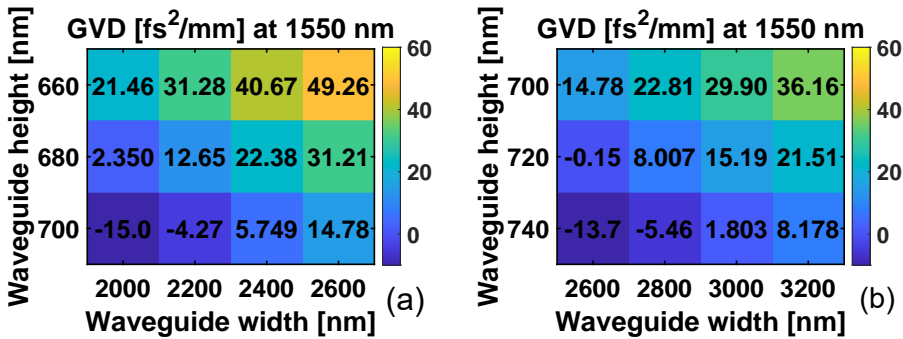


Figure 5.1: GVD at 1550nm for Si_3N_4 waveguides with varying height and width.

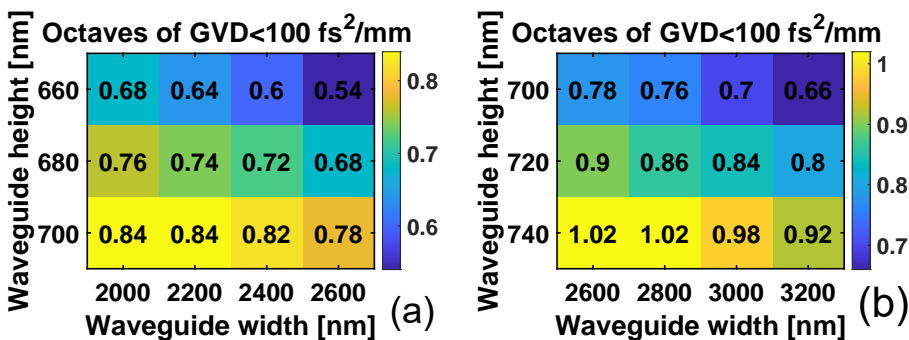


Figure 5.2: Ratio from octave of bandwidth below $100\frac{\text{fs}^2}{\text{mm}}$ for Si_3N_4 waveguides with varying height and width.

Figures 5.1 and 5.2 allow two main conclusions. Waveguides with an increased height have a larger range of wavelength with dispersion below $100\text{fs}^2/\text{mm}$. As the height increases, the dispersion at 1550nm approaches the anomalous dispersion regime. By increasing the width of the waveguide, the dispersion at 1550nm increases. And while this slightly lowers the effective bandwidth, it is still higher than for smaller waveguides. While it is important to have a low dispersion, a dispersion too close to zero, will start to deplete the region around the minimum dispersion wavelength (MDW), which will destroy the spectral flatness [102]. The exact optimal parameters depends on the expected input peak power.

Additionally, it has to be noted that increasing the size of the waveguide, will increase the effective mode area. This reduces the nonlinear coefficient, thus limiting the broadening. This effect can be partly offset by the fact it is easier to couple in power to large waveguides. As can be seen by these consideration, there are several trade off when considering the design of the waveguide. Finally, as the size of the waveguide increases, additional higher order modes can exist inside the waveguide. While the presence of higher order modes are not necessarily a problem, it is unknown what kind of effects they could introduce.

To illustrate the effect of the varying waveguide dimensions and thereby changing the dispersion, the simulated dispersion and supercontinuum for a waveguide with a height of 690nm , and a width of 1900nm , 2600nm , 3000nm , and 3400nm is presented in figure 5.3. For the first three waveguides the simulation input parameters are a pulse width of 121fs , pulse energy 200pJ , and waveguide length 4cm . Dispersion and effective area are found using Comsol Multiphysics. The final waveguide, with a width of 1900nm has anomalous dispersion. Therefore, a input pulse energy of 20pJ is used for that simulation. As the waveguide width is decreased, the dispersion

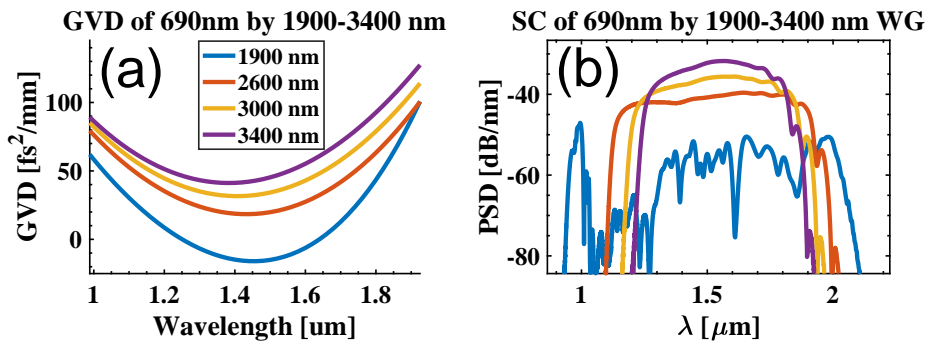


Figure 5.3: (a) GVD for waveguides with a height of 690nm and width of 1900nm (Blue), 2600nm (Orange), 3000nm (Yellow), 3400nm (Purple). (b) Simulated output spectrums from 20cm long waveguides. Input pulse width is 121fs . Pulse energies are 200pJ for the purple, yellow and orange graphs, while the blue spectrum is from a 20pJ input pulse.

goes towards the anomalous region. As expected this increases the final bandwidth of the supercontinuum. If the waveguide width is too small, the dispersion enters the anomalous dispersion regime. Here the supercontinuum is generated by the solitons and their dispersive waves, and requires an order of magnitude less pulse energy. For anomalous dispersion the spectrum varies a lot, and doesn't have the spectral flatness of the ANDi SC. To get a understanding of how these ANDi SC spectrum are gen-

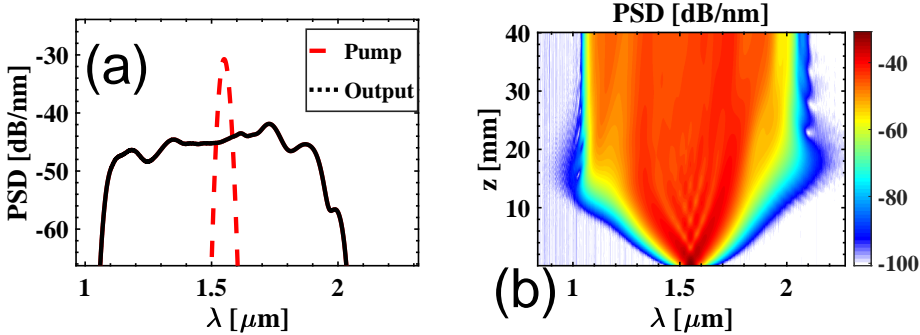


Figure 5.4: (a) Simulated supercontinuum generated by the 2600nm wide waveguide. (b) Simulated spectral evolution.

erated consider figure 5.4(b) In the first part of the propagation, it is seen that the broadening is dominated by self phase modulation as indicated by the characteristics peaks. At 18-20mm optical wave breaking at the short wavelength side is observed, and at 20-22mm we see OWB at the long wavelength edge. OWB is indicated by the appearances of the shoulders in the spectrum. In figures 5.4(a,b) it is observed how the combination of SPM and OWB creates a very flat supercontinuum. To gain further insight it is helpful to consider the following spectrograms. From the series of spectrogram in figure 5.5 we observe the key dynamics. Fig 5.5(a) shows the spectrogram after some SPM, but before OWB. The distinct S shape of SPM is seen in the spectrogram. This shape has similar wavelengths at different times, which cause large dips in the spectrum. As the pulse continues to propagate and broaden OWB converts the steepened part of the pulse to new frequencies at the edge of the pulse. This can be seen in figure 5.5(b) as light is converted from the central wavelength at the ends of temporal shape to new wavelengths. Finally, in figure 5.5(c) OWB has finished, and the shape of the spectrogram becomes an almost straight line. OWB has removed the overlapping frequencies from SPM, and the final pulse is smooth in both spectrum and time. The spectral flatness and smooth temporal shape are an very important improvement when compared to anomalous based SCG for many applications.

Simple waveguides have limited options for engineering the dispersion. The height and width can be tuned, but not much else can be done. This limits the flatness of the dispersion, and as a result, the expected supercontinuum is limited to around one

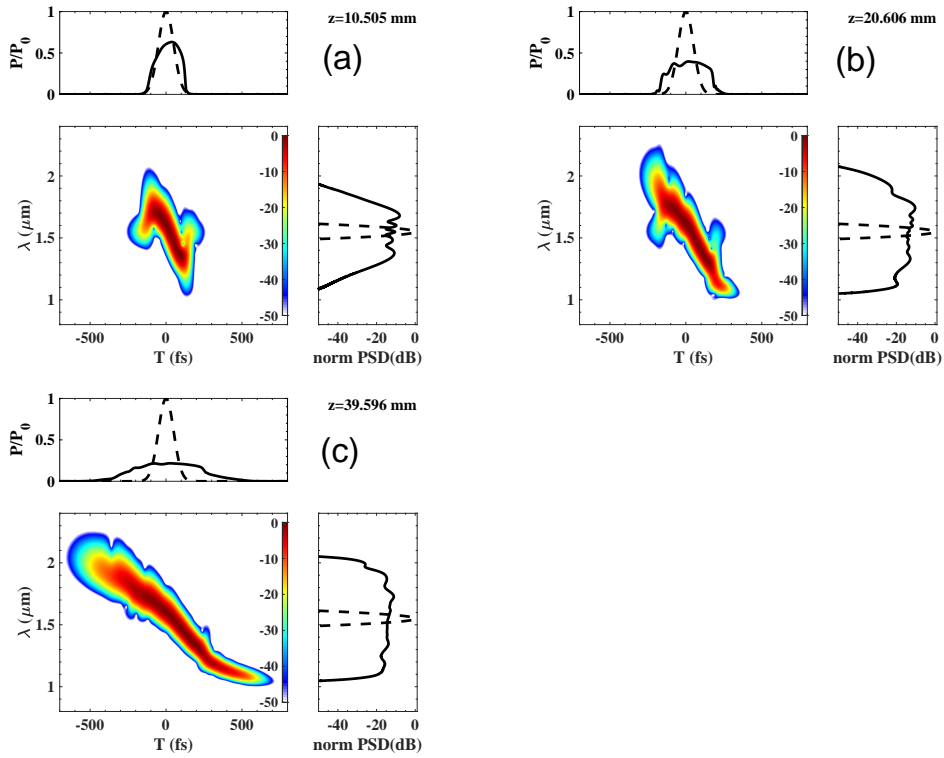


Figure 5.5: Spectrograms of simulation in figure 5.4. (a) Shows the initial SPM, and the characteristic S shape of the spectrogram. This causes dips in spectrum. (b) OWB is occurring at both ends of the pulses transferring power from the central wavelengths to the edges. (c) The final spectrogram is a nice straight line with smooth temporal and spectral shape..

octave. This problem is at the core of generating octave spanning supercontinuum in ANDi waveguides. Several techniques have been proposed as more advanced ways of dispersion engineering. While figure 5.2 suggest that increase the size of the waveguide can in large parts solve the flatness problem, larger waveguides are difficult to fabricate, they have lower nonlinearity and therefore requires more power and finally larger waveguides have more higher order modes, which can have an unknown effect on the performance of the waveguide. Simulations have shown that by constructing complex dual core waveguides the mode dispersion can be flattened [103]. These design have not been proven to work in practise and seem to be difficult to fabricate. Another method is the use of several cladding layers to modify the dispersion as in

[104]. Here waveguides have been fabricated and used and might be a possible avenue for increasing the SC bandwidth. The low dispersion necessary for ANDi SCG makes it necessary to accurately control the dispersion of the waveguide. Previous fabricated waveguides seemed to have a dispersion offset off around $20fs^2/mm$. To ensure at least one of the waveguides having normal dispersion. It is necessary to fabricate several waveguides. This results in five different waveguides.

- Waveguide 1. A 20 cm long spiral waveguide with height 690nm and width 3000nm.
- Waveguide 2. A 20 cm long spiral waveguide with height 690nm and width 2500nm.
- Waveguide 3. A 2.3 cm long straight waveguide with height 690nm and width 3000nm
- Waveguide 4. A 2.3 cm long straight waveguide with height 690nm and width 2500nm
- Waveguide 5. A 2.3cm long straight waveguide with height 690nm and width 1900nm.

Where both short straight waveguides and long spiraled waveguides have been fabricated.

5.2 Dispersion measurements

To generate broadband SC in an ANDi waveguide it is necessary to have a low minimum dispersion. On the other hand close to zero dispersion causes depletion at the MDW. As the waveguide has low dispersion, even small dispersion fluctuations can make the waveguide dispersion anomalous. This is seen in figure 5.1. As an example imagine attempting to fabricate a waveguide with height 700nm and width 2600nm. Previous work has shown fluctuations of the waveguide dimensions in the range of 3%. The fabricated height could then be 720nm and the waveguide would have anomalous dispersion. This is without any fluctuations in the material refractive index. Which can introduce even larger offsets from the designed dispersion. So a successful design of an ANDi waveguide requires an accurate measurement of the dispersion to ensure that the fabricated waveguide is all normal dispersion. Figure 5.6 shows a schematic drawing of the experimental setup used to measure the dispersion of the straight Si_3N_4 waveguides 3, 4 and 5. Waveguides 1 and 2 could not be measured in the experimental setup, as it would require a much longer delay arm. The dispersion of waveguide 1 and 2 was instead measured after fabrication using optical frequency domain reflectometry. The dispersion measurement setup is a broadband light interferometer, with the waveguide under test in one arm.

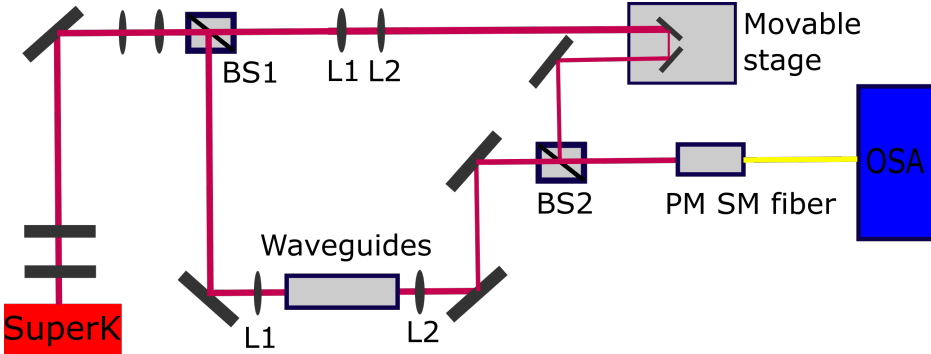


Figure 5.6: Experimental setup used to measure the dispersion of the waveguides.

The dispersion measurement works as follows: 110 mW of light with a bandwidth from 450-2400nm is sent from a broadband laser (Superk COMPACT). It is split in two at the first beamsplitter. Half the light goes through one arm, and is coupled through the waveguide, while the other half of the light is propagated through a equivalent section of air used as a delay. The exact length of the delay arm can be adjust using two mounted mirrors. All optical components in both arms are identical to ensure that the dispersion differences in the two arms are only caused by the waveguide under test. The two signals are recombined on the second beamsplitter and coupled into a polarization maintaining endless single mode fiber (LMA-PM-10). The spectrum of both arms individually and the combined spectrum are measured with an OSA. As the transmission efficiency is different between the two arms, it is

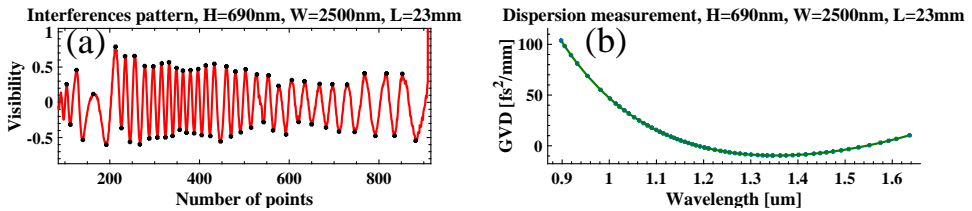


Figure 5.7: (a) Fringes in normalized spectrum of the interferometer. (b) Dispersion of 690 nm by 2500 nm waveguide calculated using fringes in (a).

necessary to normalize the combined spectrum using the spectrums of the individual arms. The result is seen in Figure 5.7(a). Essentially, the wavelength separation between fringes contains information about the dispersion. The phase matching point is identified, and using the peaks and valleys of the measurements, the dispersion is then calculated following the procedure in [105]. The resulting dispersion is seen in figure 5.7(b) By repeating the measurement with slightly different distances in the

references arm, an estimate of the accuracy can be made. The result of the dispersion measurements of waveguides 3,4 and 5 is shown in figure 5.8. The dispersion at 1550 nm of the waveguide 1 and 2 is plotted as a black circle in figure 5.8(b,c).

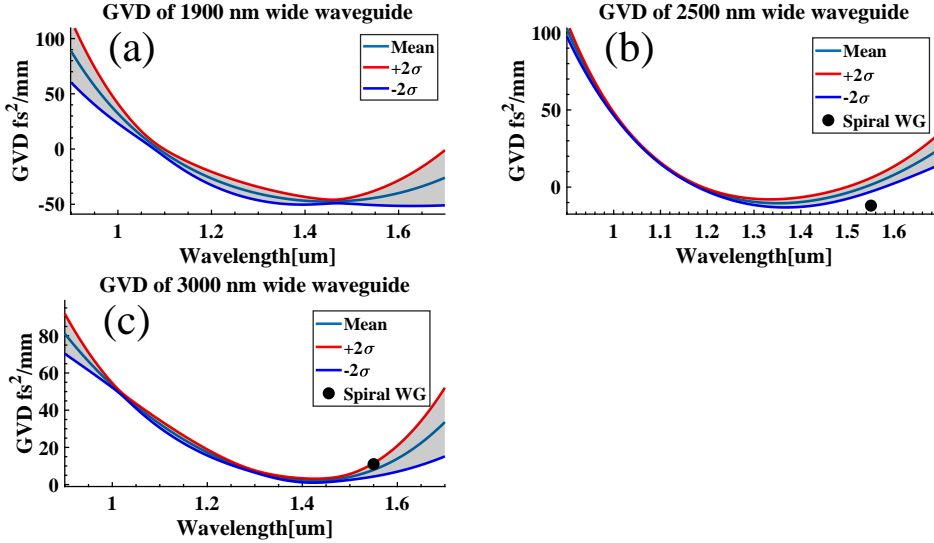


Figure 5.8: Measured GVD of waveguides with a length of 23mm, a designed height 690nm and designed width of (a) 1900nm (b) 2500nm (c) 3000nm. Grey area shows the estimated uncertainty in the measurement based on repeated measurements. Black circle in (b) and (c) show the dispersion measured for 20 cm spiral waveguide with the same dimensions.

A few things can be concluded from these measurement. Most importantly, the GVD of the waveguide 3 (width 3000 nm) is all normal. It has a minimum GVD of $\beta_2 = 2\text{fs}^2/\text{mm} \pm 1$ at 1425nm. The GVD at 1550nm is $\beta_2 = 8\text{fs}^2/\text{mm} \pm 3.5$. The dispersion of waveguide 1 at 1550 nm is slightly higher $\beta_2 = 11\text{fs}^2/\text{mm}$ at 1550nm. While the dispersion comes very close to anomalous dispersion, the measurement and their uncertainty imply that the waveguide should be all normal. Additionally, the dispersion of two interferometer arms is balanced, and should not be a concern. In Hlubina et al. [105] the measurement method itself was found able to measure the ZDW of a fiber with 1 nm error highlighting the great possible accuracy. Therefore it is concluded that both waveguide 1 and 5 are all normal dispersion. Waveguide 4 (width 2500 nm) is almost exactly 0 at 1550nm, and has a region with anomalous dispersion between 1550 nm and 1250 nm. Waveguide 2 has a dispersion of $\beta_2 = -12\text{fs}^2/\text{mm}$ at 1550nm, and is a weakly anomalous dispersion waveguide. The differences between waveguide 2 and 4, can most easily be explained by variations in wafer height during fabrication. As shown later, the difference between the two waveguides results in significantly different supercontinuum. Finally, waveguide 5

(width 1900) has highly anomalous dispersion with a dispersion of $\beta_2 = -45\text{fs}^2/\text{mm}$ at 1550nm.

5.3 Experimental setup

Before examining the experimental results obtained in waveguide 1-5, let us briefly have a look at the two experimental setups used to generate and measure the supercontinuum and RIN. The experimental setup used for supercontinuum generation can be seen in figure 5.9. A Toptica fiber based laser emits a 121 fs pulse centered at 1550nm. The repetition rate is 90 MHz, and it delivers an average power of 280mW. The polarization of the laser beam is adjusted using a halfwave plate, this allows selectively pumping TE or TM modes in the waveguide. The size of the laser beam is adjusted using a telescope to ensure an appropriate beamsize when hitting the incoupling lens. The beam is focused on the edge of the wafer, and efficient incoupling to the waveguide is apparent by the glowing of the waveguide. This can be seen in the image on the front page. Incoupling and outcoupling is optimized using 3D stages. Supercontinuum is generated in the waveguide, and then collected by an outcoupling lens and sent to a broadband fiber. The spectrum is measured on an OSA. It is important to note that the Toptica laser does not emit a perfect transform limited sech^2 pulse. The autocorrelation and spectrum of the laser is seen in figure 5.10. The autocorrelation shows 121 fs sech^2 pulse, but also a large pedestal, which contains one third of the total energy. Furthermore, the spectrum of the laser is obviously not smooth. The exact influence of the pedestal and imperfect spectrum is difficult to estimate, as the complete shape of the pulse is still unknown. Figure 5.9(b) shows the experimental setup used to characterize the (RIN) before and after the waveguide. The supercontinuum is filtered using a 12 nm bandpass filter, at the desired wavelength. The residual light is then sent to a fast photo detector. The resulting signal is measured and saved using a fast oscilloscope. Figure 5.9(c) shows a zoom in of the results of such a measurement. The peak of the pulses are marked with the red dots. To calculate the RIN the standard deviation of the peak values is calculated and normalized to the mean value. It is vital for the measurement that the detector operates in a linear regime, so that variations in the peak power of the detector response is equivalent to variations of the peak power of the output pulse. Figure 5.9(d) shows measurement of the laser RIN as the maximum voltage in the detector is varied. The laser RIN seems constant at voltages between 150mV and 800mV, so only measurements in the region is used. Finally, from these measurement it is concluded that the RIN of the Toptica laser is 1%.

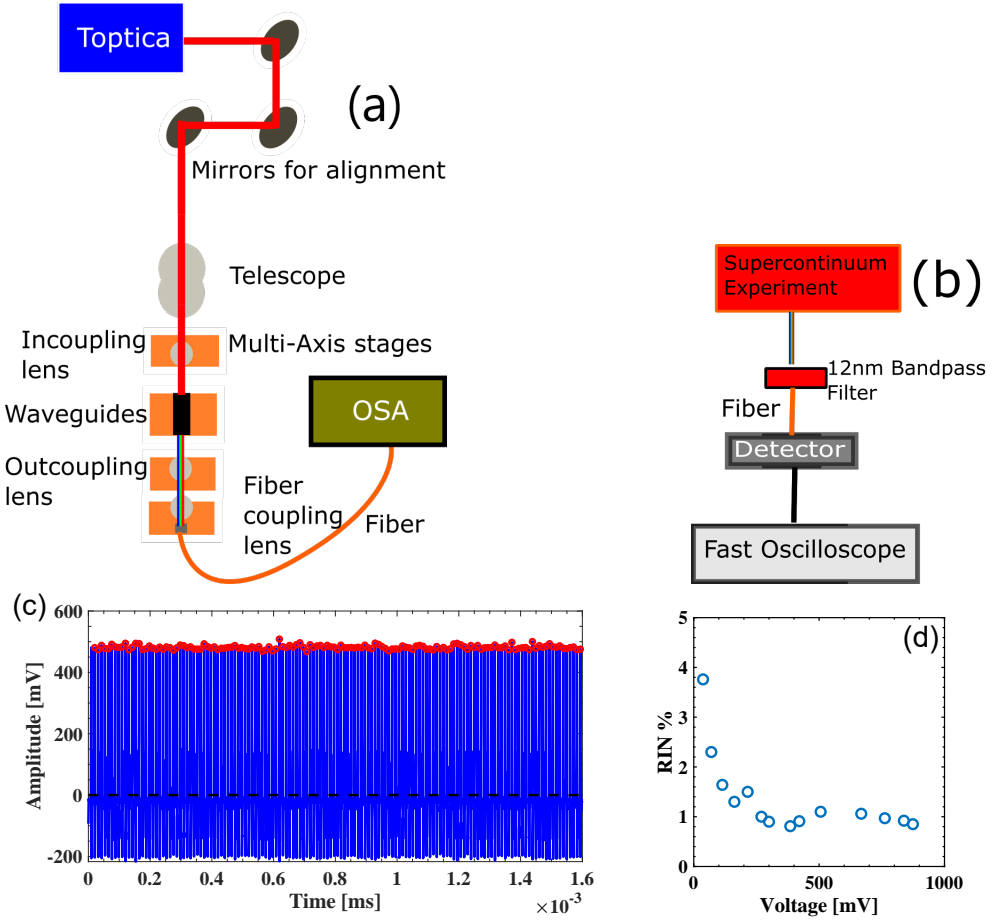


Figure 5.9: (a) Schematic drawing of experimental setup used to generate supercontinuum. (b) Schematic drawing of experimental setup used to measure RIN. (c) Example of a measurement using the setup in (b), the red dots show the peaks of the pulses. (d) RIN of the Toptica laser, measured for different peak voltages. Linear response happens from 150mV to 800mV.

5.4 Supercontinuum and RIN in 20cm Spiral Waveguides

To generate SC in the 20 cm ANDi spiral waveguide it is pumped with the Toptica laser as seen in figure 5.9(a). For an image of the waveguide in operation see the

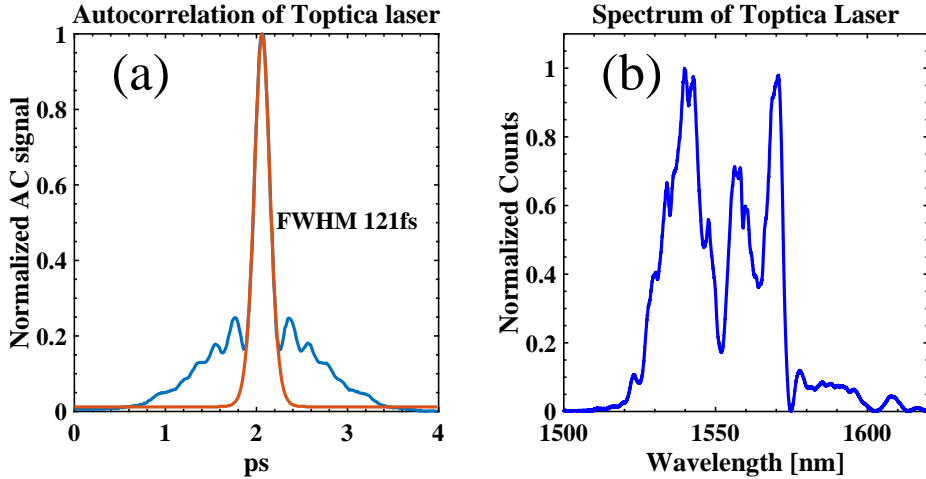


Figure 5.10: (a) Autocorrelation of Toptica laser, sech^2 fit of the measurement is shown in orange. Blue is measured autocorrelation. (b) Spectrum of the Toptica laser.

large image on frontpage c. Only a fraction of the 280mW of power is coupled into the fundamental mode of the waveguide. The incoupling loss is estimated to 10dB, with the remaining power coupling to both fundamental and higher order modes. We estimate that approximately 50% goes to the fundamental mode and the rest is coupled to higher order modes. Based on this, there is 14mW of power in the fundamental mode. Approximately a third of this power resides in the pedestal of the input pulse, and does therefore not contribute to the peak power of the pulse, or generate significant SC. 7mW of power is collected after the waveguide. This corresponds to a 3dB outcoupling loss. Furthermore, the power of the higher order modes doesn't seem to be collected. This is believed to be caused by the higher order modes having an increased bending loss as a result of the spiraling of the waveguide. The resulting spectrum and RIN is recorded for three different input powers, 1.4mW (16pJ), 7mW (78pJ) and 14mW (155pJ). See figure 5.11. The input power is adjusted using reflective neutral density filters after the output of the laser. The 14mW supercontinuum has a 20 dB bandwidth from 1150nm to 1975nm, corresponding to a 0.7 octave bandwidth. The PSD is never more than 20dB below the peak PSD inside this entire bandwidth. A number of sharp valleys are observed in the region from 1450nm to 1650nm. For lower input pulse energies a similar spectral shape is observed, but with a smaller bandwidth. Initial simulation seen in figure 5.4, suggest a maximum of 5dB deviation from the maximum power for an ANDi SC. In general, the reduced flatness of the spectrum can be explained by including imperfect spectrum of the Toptica laser in the simulations. Figure 5.12 shows the spectral evolution(a) and resulting spectrum(b) of the waveguide using the Toptica spectrum as input pulse

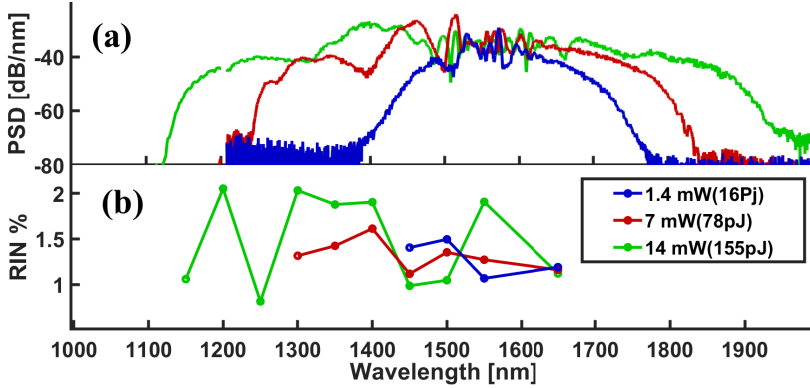


Figure 5.11: (a) Experimental spectrums from 3000nm width spiral waveguide.(b) Relative intensity noise measured at the same input pulse energies.

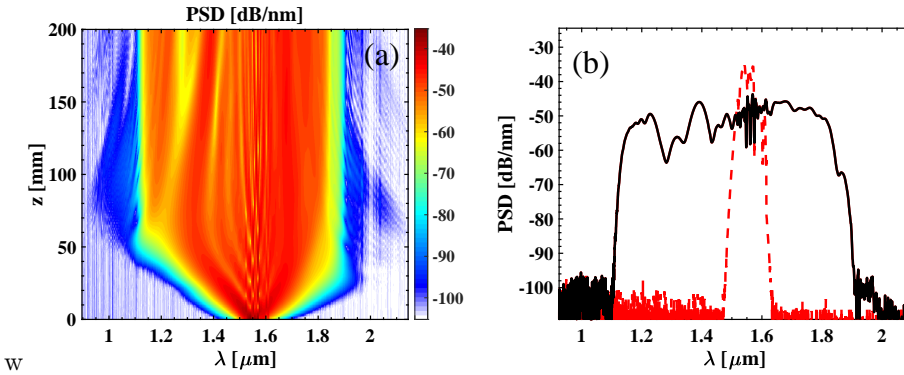


Figure 5.12: Simulation including Toptica laser spectrum. 100pJ, dispersion modified to equal spiral waveguide measurements at 1550nm. Toptica pulse is chirped until 121fs. (a) Spectral evolution along the length of the waveguide. (b) Output spectrum at z=20cm.

and a $GDD = 2600 [fs^2]$, so that the final pulse width is 121 fs. This reproduces both the sharp valleys in the in the 1450-1650nm region, and the larger 15-20dB deviations in the shorter wavelength side. Based on this it is concluded that the main cause of imperfect spectral shape is the initial pulse spectrum. When considering the RIN measurement, a few things are noteworthy. No measurement is above a RIN of 2.2 %. Furthermore, only a small increase in RIN is observed, when increasing the input pulse energies. Finally, no strong wavelength dependence is observed in noise measurements. From this we can conclude that the ANDi SC seem to retain low noise inside the full bandwidth of the SC. The increasing pulse power also does

not introduce noise, confirming that coherent ANDi SC is not limited to low pulse energies.

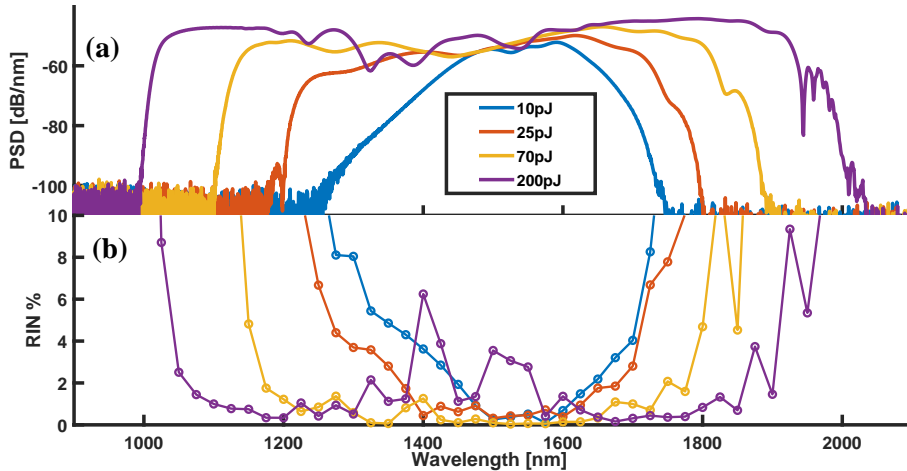


Figure 5.13: (a) Simulated spectrums from a 3000nm wide and 20cm long waveguide with different input pulse energies. (b) Relative intensity noise simulated at the same input pulse energies.

Now let's compare the experimental supercontinuum and RIN with simulations. The GNLSE is solved according to chapter 2. The measured dispersion of the 3000nm wide waveguide is used as dispersion. The effective area is computed using COMSOL. RIN calculations are based on an input pulse RIN of 1% as seen in the laser measurements. 20 simulations are performed, and simulated RIN is the standard deviation of the 12 nm bandpass filtering of the resulting spectrum. The resulting spectrum and RIN are shown in figure 5.13. The simulations reproduce the expected bandwidth. Furthermore, we see that the simulated RIN is relatively constant as a function of power and stays low over the full bandwidth of the supercontinuum. Only at the edges of the SC does the RIN increase dramatically. Similarly, the RIN measured in the experiment shows small fluctuations in the RIN is observed, but all of it is still around 1-2%. The only exception is the 200 pJ supercontinuum (Purple). Here a few peaks in the RIN is above 2%, with a maximum of 6%. This is caused by the depletion of power at 1550nm and 1400nm. It is observed that the 200 pJ input pulse SC is expected to generate an octave spanning supercontinuum, and RIN simulations suggest that it retains low noise. The depletion of power around the pump and MDW suggest that the dispersion of the waveguide is slightly to low compared to the optimal. Now the 20 cm spiral waveguide with a width of 2500nm is pumped in the same setup. As seen in the dispersion measurement, this waveguide has a weak anomalous dispersion. The dynamics are therefore expected to be dominated by solitons and dispersive waves. The resulting spectrum and RIN is seen in figure 5.14. The spectrum

and noise of anomalous SC is very dependent on input power. Therefore, the input pulse power is varied in small increments to ensure that the RIN and supercontinuum can be measured at various stages of propagation. At the initial low power of

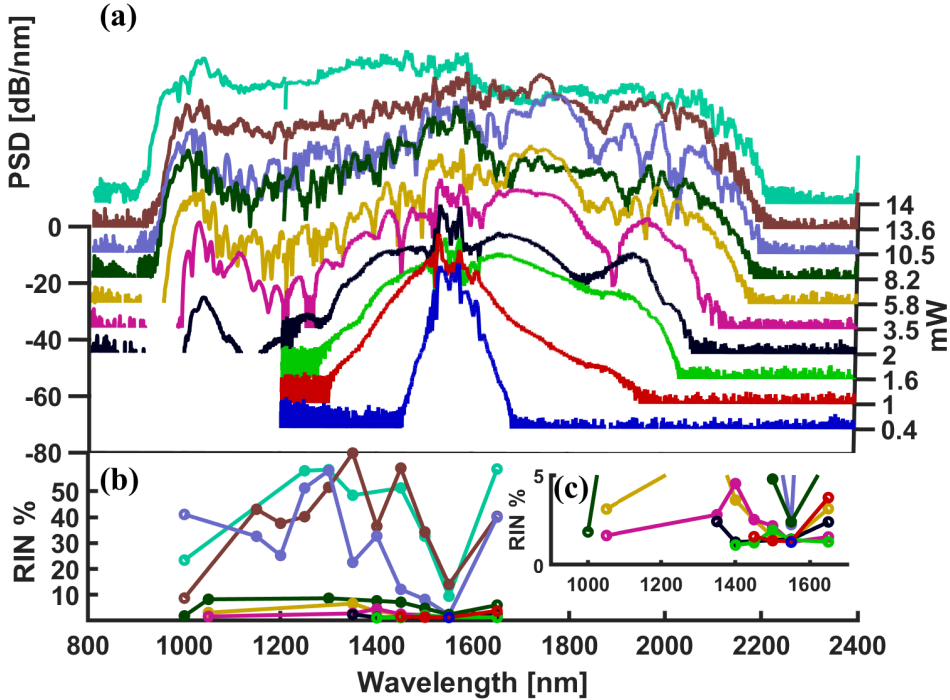


Figure 5.14: (a) Experimental spectrums from the 2500nm wide spiral waveguide. Average power in the waveguide shown on zaxis. (b) Relative intensity noise measured at the same input pulse energies. (c) Zoom in on (b) to illustrate behaviour at low RIN.

0.4mW (Blue, 4.4 pJ) little broadening is observed, but as the input power increases, the pulse broadens, and at 2 mW (Black, 22 pJ) dispersive waves are observed at 1 and 2 μm . This signals that the pulse has undergone soliton fission. As the input power increases, the supercontinuum has an increasing number of ripples, and the spectrum becomes flatter and flatter. The full power 14 mW (Cyan, 155 pJ) supercontinuum covers from 900nm to 2200nm, and is relatively flat. But as observed in the RIN measurement, it has a RIN of around 50%. As the measured supercontinuum is an average of many pulses, a very noisy SC will have a smooth spectrum as the differences average out. It is observed that as the power increases after the soliton fission (Black), the noise increases. This is as expected. Continued propagation after soliton fission is known to cause an increase in noise. This caused by the continued

interaction of the solitons. The increase in noise is significantly different from previous predictions based on only quantum noise such as in [33], where doubling the input pulse energy has no significant influence on the noise. Here it is experimentally observed that increasing the input power drastically increases the RIN. This is best seen in figure 5.14(c), when comparing 2mW (black, 22 pJ) and 3.5mW (pink, 37 pJ) and 5.8mW (Yellow, 64 pJ). This highlights the importance of including the intensity noise of the laser when simulating the noise of SCG. Interestingly the RIN of the dispersive wave at 1 μ m, seems to increase slower than the central part of the spectrum. Even at input powers four times the necessary power for soliton fission, the dispersive wave has a RIN of 2-3%. This is in contrast to the 10 % RIN observed over the rest of the spectrum. This relative low noise enables the spectrum at the dispersive waves to be used for noise sensitive application, even when the rest of the spectrum is noisy. Finally, it is clear from this observation that noise measurement performed on the dispersive waves cannot be used to infer the noise of the rest of spectrum. From this it is concluded that for the full power pulse, the noise of the anomalous waveguide is much higher than the ANDi waveguide. But if the power is reduced to only just allow soliton fission, a minimal increase in noise is found. One thing to highlight is the fact that an octave spanning supercontinuum is generated using a pulse energy of 22pJ, with noise similar to the laser. One caveat with RIN measurements is that the RIN is difficult to measure for wavelength with low power, and therefore the RIN cannot be measured in as broad a bandwidth for the low input pulse powers.

To verify the experimental result another simulation is performed investigating the RIN and supercontinuum, that can be expected from waveguide 2. The results are seen in 5.15. The RIN is calculated based on a 12nm bandpass filter, to make it comparable to the experiment. The RIN is calculated with the standard deviation of 20 simulations.

Comparing the RIN and SC of three simulation using different average input pulse energy(a,b), a few things can be observed. Similar to the experiment, it is observed that little noise is generated over the whole supercontinuum before the soliton fission (Blue). After soliton fission, the RIN increases, but it is still similar to the RIN before soliton fission at most wavelengths. At 70pJ the pulse has more power than necessary for soliton fission, and RIN above 50% is observed for most wavelengths. This further confirms the result that the noise of the anomalous SCG grows rapidly after the soliton fission. And therefore, the bandwidth of the supercontinuum is limited to what is seen in black graph in experiment, or orange in simulation, if a low RIN is desired. Finally, as observed in experiment, simulations show that the RIN at 1 and 2.2 μ m does not increase as rapidly as the rest of the SC. This is most easily observed in figure 5.15(b), where the RIN at the DWs are similar for 20pJ and 70pJ, while the RIN is vastly different at other wavelengths, confirming that observation the dispersive waves seem to be less influenced by the input pulse power fluctuations. This phenomenon is perhaps best understood by the fact that the dispersive waves wavelengths are mostly determined by the phase matching conditions, and therefore does not heavily depend on the input pulse power after soliton fission. It is interesting to consider the RIN and spectral evolution as the pulse propagates

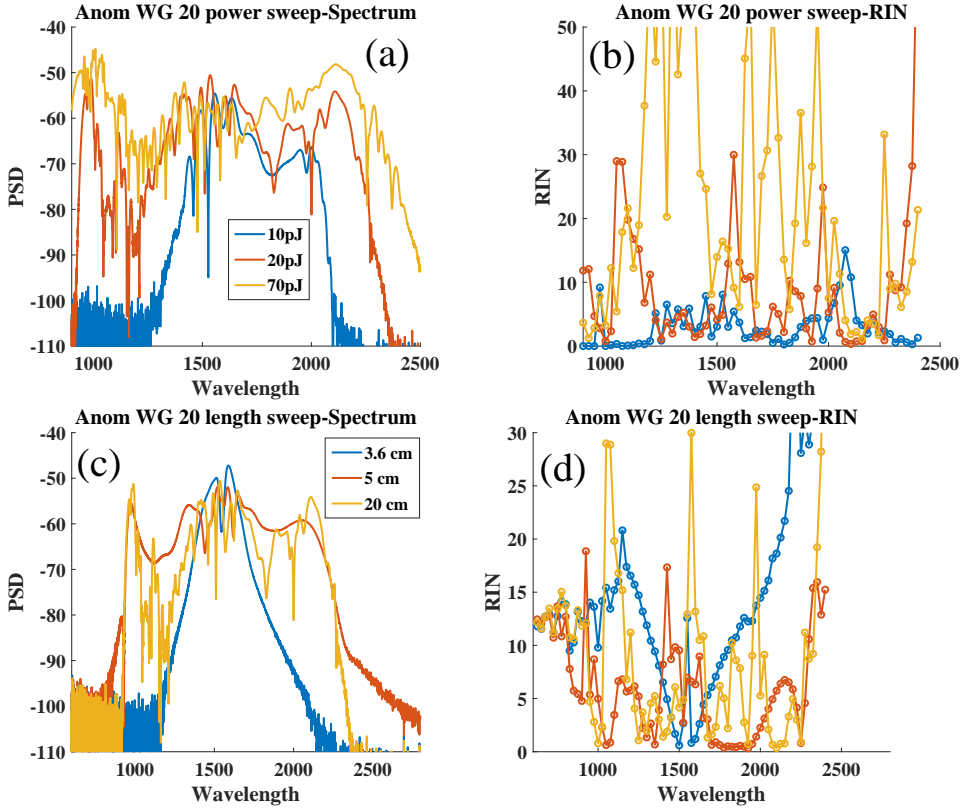


Figure 5.15: (a) Simulated spectrums from a 2500nm wide, 20 cm long waveguide, with different input pulse energies. (b) Relative intensity noise simulated at the same input pulse energies. (c) Spectrum at various propagation distance for the 20pJ simulation. (d) RIN at the same propagation distances.

along the waveguide. This is shown in figure 5.15(c,d). The spectrum and RIN is illustrated for three different lengths of the waveguide, corresponding to before soliton fission, right after fission, and at the end of the waveguide. As expected the RIN before fission, has low RIN. But it increases at the edges of the spectrum, as small variation in input power has an effect on the bandwidth, causing large fluctuations at the edges. If the RIN at soliton fission and after fission is compared, it is seen that the RIN increases as it propagates. But interestingly the RIN at the dispersive waves is higher at soliton fission. This is understood, when considering that variations in the input power changes the soliton fission length. This in turn means that the conversion of power to DW can be influenced quite heavily at exactly this length.

While further study of this effect is needed, it introduces an interesting dilemma. The RIN is not minimum for all wavelength at the same parameters. So the RIN can be minimized at different wavelengths dependent on the exact experimental setup. In general, it is difficult to reproduce the measured RIN in simulations. While the general behaviour is similar, the RIN is strongly dependent on the exact nonlinear dynamics and generated spectrum, which dependent on many relatively uncertain parameters, uch as the exact input pulse shape, and the waveguide dispersion. This is also illustrated by the fact that it is very difficult to predict the RIN at any given wavelength.

5.4.1 Comparison to anomalous

The RIN of the anomalous SC grows rapidly after soliton fission, therefore, it is most fair to compare the anomalous dispersion waveguide to the ANDi waveguide right after soliton fission. The supercontinuum and RIN of the ANDi waveguide using full input power(14 mW,155 pJ) is shown together with the SC and RIN of the anomalous waveguide right after soliton fission(2 mW, 22 pJ).

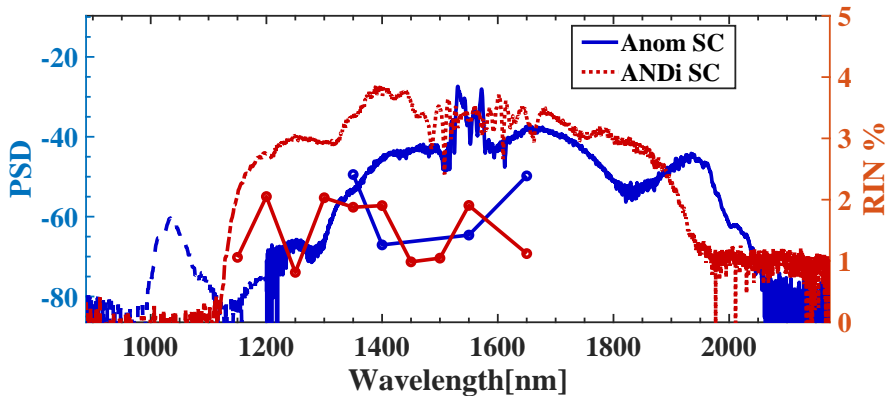


Figure 5.16: (Blue) Supercontinuum of 2500nm wide spiral waveguide, with 2mW (22 pJ) input power, to give soliton fission close to the end of the waveguide. (Red) Supercontinuum of 3000nm wide spiral waveguide with 14mW (155 pJ) input power. Circles show the corresponding RIN.

Figure 5.16 shows that at exactly the soliton fission, the two waveguides have similar noise, but the reduction in input pulse energy for the anomalous waveguide shows in the spectrum. The power at the 1 um dispersive wave is 30dB lower than the pump, and there is limited power in the region from 1300nm to 1100nm, with a 30-60 dB drop from the maximum. In comparison the ANDi SC is much smoother, and doesn't deviate more than 20 dB from the maximum over the full bandwidth.

The supercontinuum of the anomalous waveguide with the low input pulse power is broader than the ANDi SC, and covers around an octave from 1 μm to 2 μm . The normal dispersion SC doesn't cover an octave even at full power. To summarize: the ANDi supercontinuum is in general smoother, but requires higher input power to generate a similar bandwidth. The anomalous SC requires low power and generates a broader SC, but at the cost of the continuity of the spectrum.

5.5 Supercontinuum and RIN in 23mm Straight Waveguides

The comparison and investigation of ANDi and anomalous SCG was done in 20 cm long spiral waveguides. Most on-chip waveguide supercontinuum experiments are performed in shorter waveguides. Therefore, the experiment was repeated using the straight waveguides with a length of 23mm. As seen in the dispersion measurements in figure 5.8(a), the dispersion of the 3000nm waveguide is all normal. On the other hand it is clear from figure 5.8(b) that the dispersion of the 2500nm wide straight waveguide differs from the spiraled waveguide with 2500nm width, as it is very slightly normal dispersion at 1550nm, but is weakly anomalous in the region from 1200nm to 1500nm. Therefore, it cannot be easily compared to the 2500nm spiral waveguide. And it is not a good representative of a typical anomalous SC. The 1900nm waveguide on the other hand is anomalous at 1550nm, and is therefore a conventional anomalous waveguide. The dispersion of the 1900nm waveguide is seen in figure 5.8(c).

Figure 5.17 shows the supercontinuum and RIN of the 1900nm and 3000nm wide waveguides, both with a length of 23mm. The average power in the anomalous waveguide is adjusted to the point where soliton fission is observed(3.5mW). In the short waveguide it is observed that broadening of the ANDi waveguide is heavily reduced. This is caused by a lack of input power, and short length. The spectrum covers from 1350nm to 1700nm, and the RIN is around 1%. It is clear that if the goal is to generate octave spanning supercontinuum, a longer waveguide, or more input pulse power is necessary. This highlight the necessity of fabricating spiraled waveguides. The anomalous waveguide easily broadens during the short waveguide, as the necessary power is lower. Similar to the spiral waveguides it is observed that the noise remains low for both waveguides. The ANDi WG does slightly outperform the anomalous waveguide.

Figure 5.18(a) shows the supercontinuum and RIN in waveguide 5 for two different input powers, one right at soliton fission(Red), and one where there is room for some interaction after fission(Blue). The supercontinuum right after fission shows no increase in noise. It has two dispersive waves, one at 750nm and one at 2250nm, which corresponds to a 1.6 octave bandwidth. The high power SC, has similar broadening, but has an increased noise with RIN from 5-20%. This confirms the previous results in the spiral waveguides, that the noise increases after soliton fission. This is an

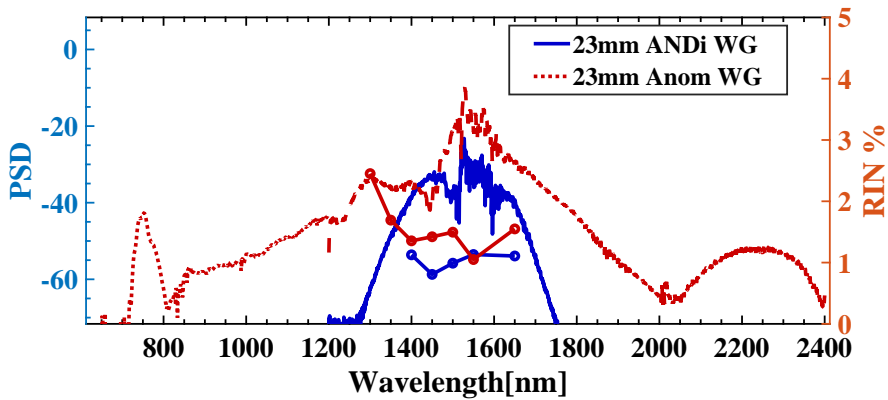


Figure 5.17: (Red) Supercontinuum of 1900nm wide straight waveguide with input power adjusted to give soliton fission close to the end of the waveguide. (Blue) Supercontinuum of 3000nm wide straight waveguide with full input power. Circles show the corresponding RIN. (Red) Anomalous dispersion, 4.5mW(50 pJ) input power. (Blue) Normal dispersion, 13mW(144 pJ) input power.

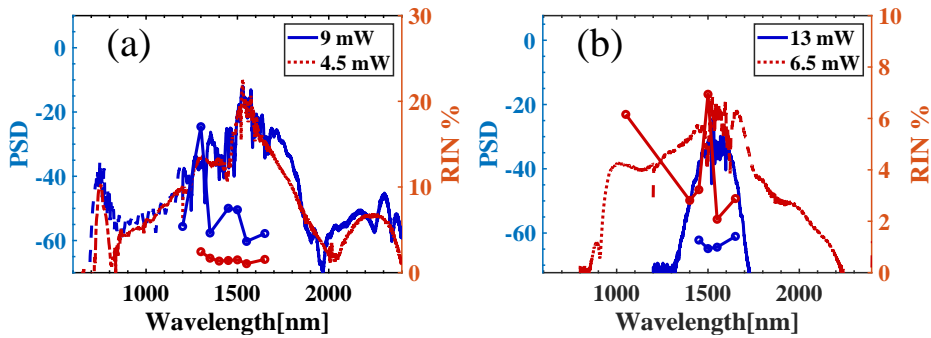


Figure 5.18: (a) Experimental supercontinuum generated in 1900nm wide waveguide with two different input pulse energies. (Red) 4.5mW (50 pJ), (Blue) 9mW (100 pJ). Circles show the measured RIN. (b) Experimental supercontinuum generated in 2500nm wide waveguide with two different input pulse energies. (Red) 13mW (144 pJ), (Blue) 6.5mW (72 pJ). Circles show the measured RIN.

important result, as it shows that even for the commonly used 1-2cm long waveguides, the noise of the SC increases rapidly with an increase in input power. Similar to the 20cm anomalous spiral waveguide, it is observed that the dispersive waves has 30dB

lower power than the pump, and some regions of the spectrum, such as 800 and 2000nm, has as much as 60dB less power. As mentioned previously the power from HOM is not collected in the spiral waveguides. In contrast, approximately double the output power is measured from the straight waveguides. And the output spectrum seem to include a fraction of the pump. Now, compare this to the simulated SC and RIN. Let's start with the simulated results from the 1900nm waveguide. Figure 5.19

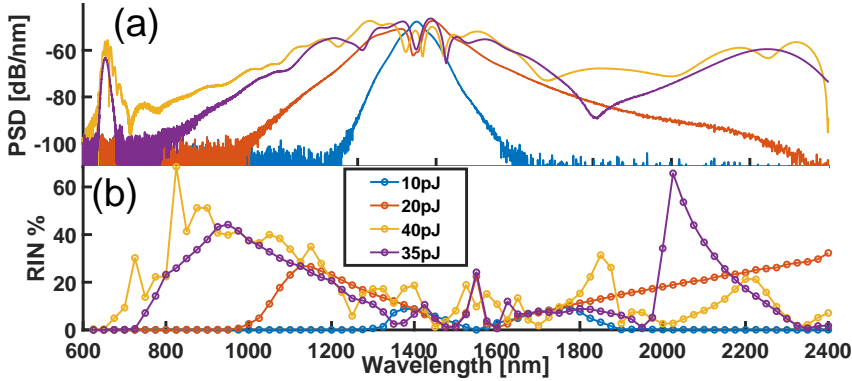


Figure 5.19: (a) Simulated spectrums from 1900nm width waveguide. (b) Simulated relative intensity noise. Pulse energies are shown in legend.

shows the SC at different input pulse energies. For pulse energies of 10pJ and 20pJ, soliton fission hasn't happen and the noise is low. At 35pJ soliton fission happens, and two dispersive waves are generated. RIN simulations confirm that the spectrum has low noise at dispersive waves, and at the central part of the spectrum. It is observed that at 1500 nm, the RIN approaches 30% which is not seen in measurements. As the input pulse energy increases from 35pJ to 40 pJ, an over all increase in RIN is observed. The RIN between the the soliton and the dispersive wave is high for all input pulse energies. It is difficult to generate SC with low RIN in the regions between the soliton and the dispersive waves. The effect is mainly caused by the lack of power in these regions. This finishes our investigation of the noise and SC of ANDi waveguides, and how they compare to anomalous dispersion waveguides. As a final curiosity, the noise and SC of the 2500nm waveguide, are investigated. This waveguide has a ZDW very close to the pump, and is in some sense a hybrid between a normal dispersion waveguide and an anomalous dispersion waveguide.

Figure 5.18(b) shows the SC and RIN for the 2500nm wide waveguide. It is seen that for low power(Blue) the spectrum has little broadening, and the noise is just the laser noise. But for maximum power an octave spanning SC is generated from 1-2um. The RIN is increased to between 2-8%. Interestingly, the SC is more continues than the anomalous SC. and it retains better noise when pumped with full power. The simulated RIN and SC for the 2500nm short waveguide is seen in figure 5.20

Simulations agrees with the spectral shape of the SC, and the RIN simulation

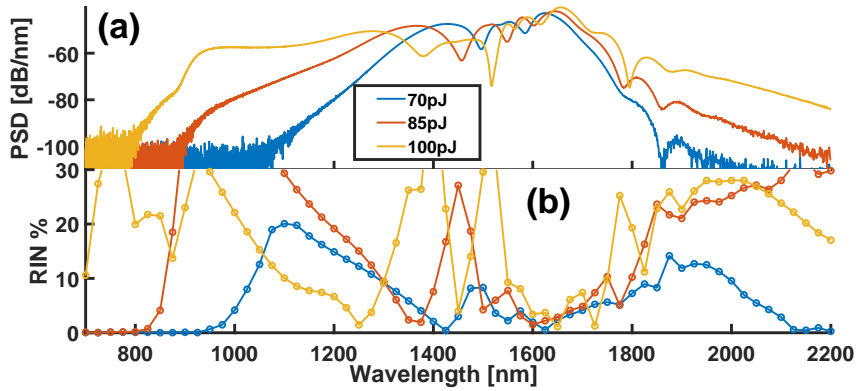


Figure 5.20: (a) Simulated spectrums from 2500nm straight waveguide. (b) Relative intensity noise calculated at the same input pulse energies. Pulse energies shown in legend.

show similar behaviour as in the experiment. A large increase in the RIN at 1500nm, and a RIN of 5-10% at 1100nm. The RIN is seen to increase further at wavelengths below 1100nm. In general, the simulated RIN is quite high for all SC except for the once generated in ANDi waveguides. The effect is mainly caused by insufficient powers at these high RIN wavelengths. These regions of high RIN are not confirmed experimentally. The reason for this is that it is exactly these regions of low power that cannot be measured in experimental setup.

5.6 Simulation of picosecond pumped supercontinuum

Generating coherent supercontinuum in the anomalous dispersion regime, is only really feasible for input pulses with a pulse width below 150 fs. Even then it is necessary to limit the pulse energy to retain coherence. ANDi SCG does not suffer from the same noise processes, and can generate coherent SC for longer pulses. Furthermore, by examining equation 5.1 SC

$$|\Delta\omega_{SPM}(z_{OWB})| \propto \sqrt{\frac{\gamma P_0}{|\beta_2|}} \quad (5.1)$$

it is observed that the SPM bandwidth is independent of the input pulse width, as long as the peak power remains constant. To illustrate this effect, supercontinuum generation is simulated in the all normal waveguide with four different pulse width from 120fs to 1.2 ps. The peak power is kept constant by increasing the pulse energy,

when the pulse width increases. The OWB distance increases linearly with the pulse width [54]. Therefore, the waveguide length has to be correspondingly increased. The result is seen in figure 5.21. The Raman effect has been ignored in these initial simulations.

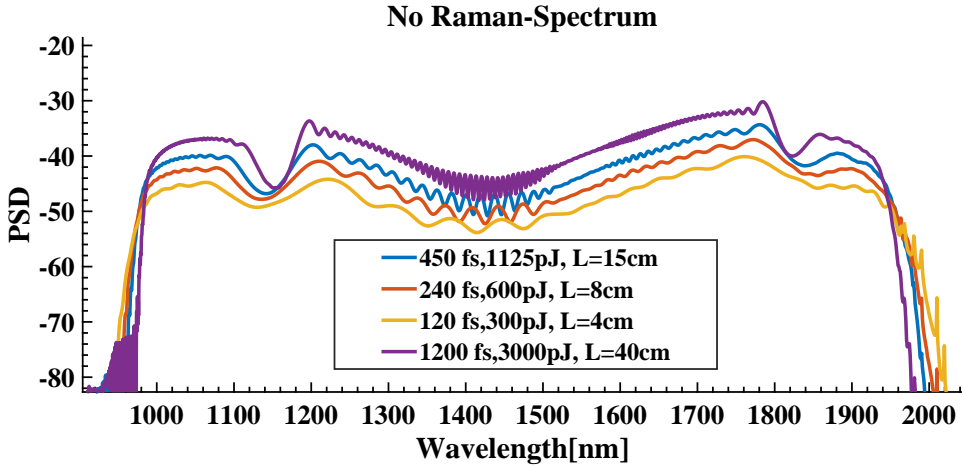


Figure 5.21: Simulated supercontinuum generated for different input pulse lengths. The Raman effect is neglected.

It is noteworthy, how similar the spectrum of the four different simulations are. This shows a great possibility of ANDi waveguide, the ability to use longer pump pulses and still obtain a flat coherent SC. When a input pulse width of 1200fs is used it is necessary to have 40cm of waveguide. This is clearly impractical in straight waveguides and again motivates the fabrication of low loss spiral waveguides. A few caveats have to be mentioned. Three possible methods of decoherences are known from generating ANDi SC in PCF. Modulation instability can occur if the dispersion profile has $\beta_4 < 0$ [52]. This effect is not seen in our waveguide, as $\beta_4 > 0$ at all relevant wavelengths. Polarization modulation instability can occur, if the peak power is to high, and the birefringence of the fiber is too small [100, 101]. This effect can be ignored, as the rectangular shape of the waveguide ensures a big difference between TE and TM modes. The final noise source is the Raman gain. As the pulse width becomes longer, the Raman gain is incoherently seeded and generates a noisy supercontinuum [51]. The effect is difficult to estimate in SiN waveguides, as the Raman gain and response function is largely unknown. Using the Raman response function previously introduced in 2.3.5, three different simulations are performed.

Figure 5.22 shows the effect of the Raman fraction on the supercontinuum. In (b) a Raman fraction of 0.2 is used, together with a pump pulse width of 120fs, little noise is observed in comparison between the spectrums. (c) shows the spectrums resulting

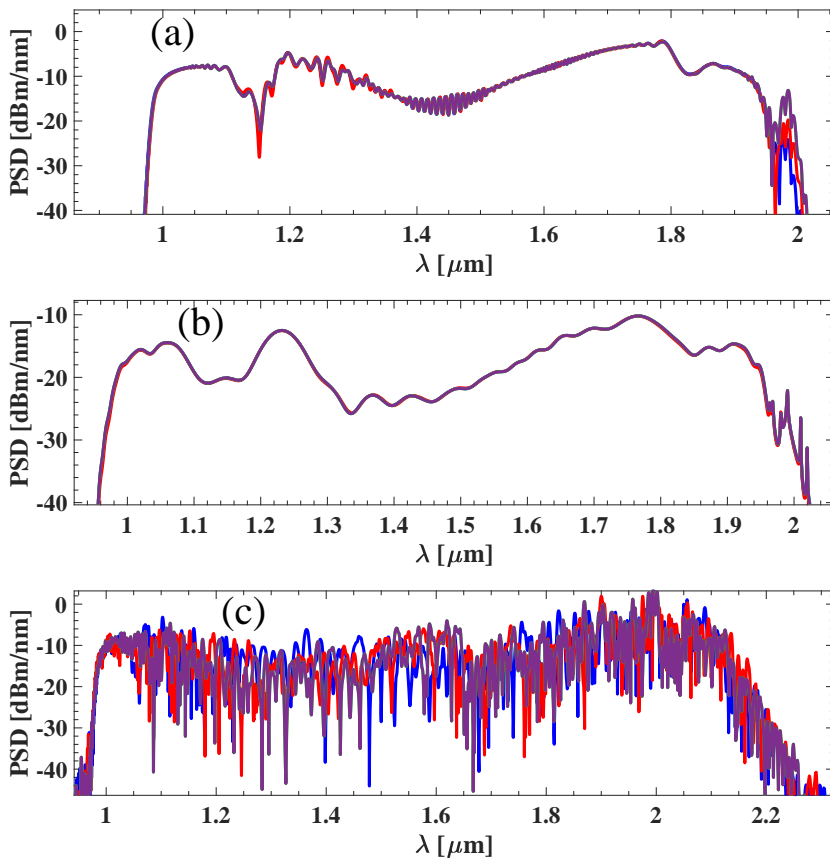


Figure 5.22: Simulated supercontinuum generated for three different input parameters. (a) Raman fraction 0.1, pulse width 885fs. (b) Raman fraction 0.2, pulse width 120fs. (c) Raman fraction 0.2, pulse width 885fs. Each figure contains four simulations for comparison.

from a simulation with a Raman fraction of 0.2, and a 885fs input pulse width. Here a very noisy spectrum is seen. (a) shows the results of using the same pulse width of 885fs, but with a Raman fraction of 0.1, Here little noise is observed. This confirms that the noise is strongly dependent on the pulse width and Raman fraction.

To quantify the influence of the Raman fraction and pulse width on the RIN, octave spanning supercontinuum were simulated in the ANDi waveguide. The peak power was kept constant. Raman fraction and pulse width were varied. Waveguide length and pulse energy were changed accordingly. The weighted average of the RIN

was computed based on 20 simulations, following equation 5.2.

$$\langle RIN \rangle = \frac{\int_{\omega_1}^{\omega_2} |RIN(\omega)| \langle |A_i(\omega)|^2 \rangle d\omega}{\int_{\omega_1}^{\omega_2} \langle |A_j(\omega)|^2 \rangle d\omega} \quad (5.2)$$

The input RIN of laser was 1%. The result is seen in figure 5.23

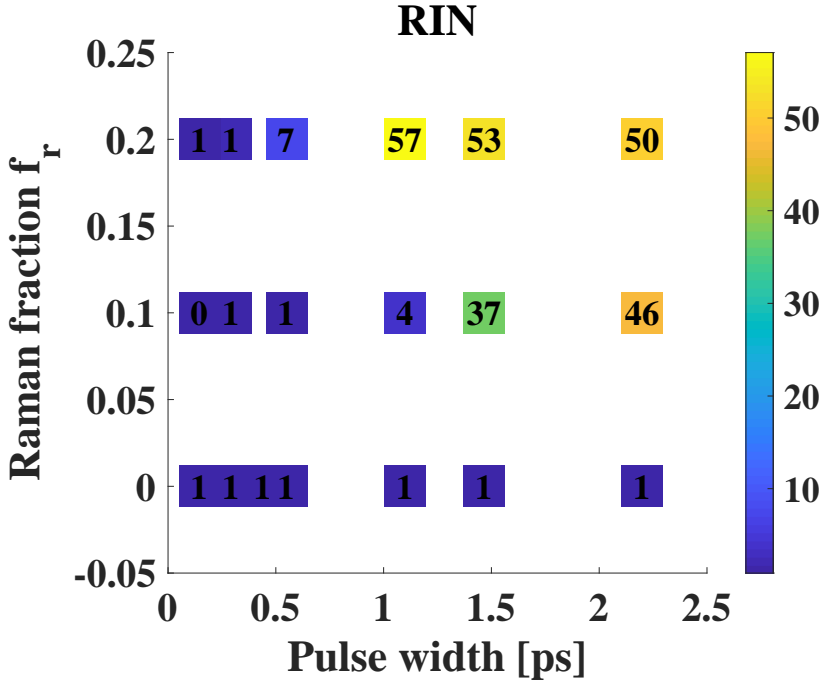


Figure 5.23: Numerical map of the weighted average of the RIN. As the Raman fraction and input pulse widths are varied, the RIN of the SC changes. RIN is calculated based on 20 simulations.

If the Raman effect is neglected (Raman fraction 0), no increase of the RIN is observed even for input pulse widths as long as 2.2ps. If the Raman fraction is increased to 0.1, it is observed that the noise starts to build around 1.2ps. It becomes very noisy at 1.5 ps. Finally if a Raman fraction of 0.2 is used, the increase in noise starts as early as 650fs, and it is completely noisy at 1.2 ps.

Based on this it is clear that the strength of the Raman effect is vital in limiting the pulse width that can be used for ANDi SCG. Previous work has reported a weak Raman effect in comparison to silica [106], which implies that SiN waveguides would have better noise performance at longer pulse length. Finally, it is important to realize that even for the case of the strongest Raman effect 0.2, which is similar

to the silica Raman effect, pump pulses as long as 600-800fs can be used with limited increase in the noise. This is a massive improvement compared to anomalous dispersion waveguides, and should be investigated further.

5.7 Octave-spanning frequency comb generation in silicon-rich silicon nitride waveguide

The following results were mainly obtained during an external stay at CUT. The majority of the results are published in Christensen et al. [37]. These results showcase the initial attempt at generating a frequency comb SC in an ANDi waveguide. A SiRN waveguide was used with a height of 660nm and width of 2300nm. The simulated dispersion of the fundamental TE mode is shown in figure 5.24(a). The simulated dispersion profile is ANDi. The waveguide is 4 cm long. A free space coupling setup is used to couple into the waveguide. The laser is a 45fs frequency comb fiber laser with a repetition rate of 250 MHz. The power in the waveguide is estimate to 32mW.

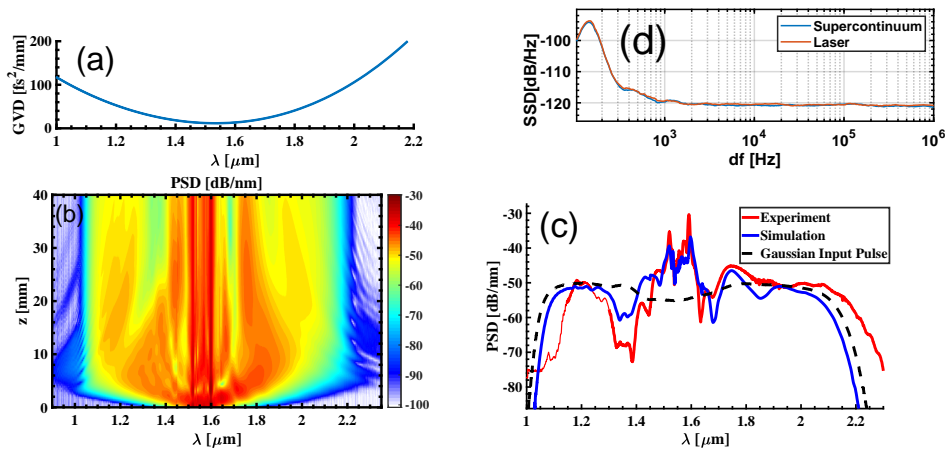


Figure 5.24: (a) Simulated dispersion profile of 660nm by 2300 nm SiRN3.9 waveguide. (b) Simulated spectral evolution. (c) Measured spectrum (red). Simulated spectrum with the input pulse being the experimental pulse (blue). Simulated spectrum from a Gaussian input pulse. (d) Single side phase noise of the repetition rate before and after SCG. It is filtered around 1551nm.

The simulated spectral evolution is seen in figure 5.24(b). The measured SC is compared with the simulated SC in figure 5.24(c). Additionally, the spectrum obtained, if the input pulse was a Gaussian, is also shown. It is clear that the input pulse shape nicely explains the large dips in the spectrum. The generated spectrum covers

and octave from 1100nm to 2200nm . To investigate whether the comb retains coherence, a portion of the spectrum is sent to a photo detector, and the single-sideband phase noise of the 250MHz signal is measured using a electrical spectrum analyzer. Figure 5.24(d) shows the phase noise before and after the waveguide. From this it is concluded that the comb retains coherence. Further investigation of this waveguide at DTU showed a small increase in the RIN compared to the laser. Furthermore, dispersion measurements indicated a weak anomalous dispersion at 1550nm. These results could not be bought into agreement with the generated SC. This inconsistency was the initial motivation for the fabrication of the waveguides measured in previous part of this chapter.

5.8 Summary

In this chapter a handful of different experimental and numerical results are shown. Most importantly a supercontinuum covering from 1150 to 1975nm was generated in a 20 cm long all normal dispersion Si_3N_4 spiral waveguide by pumping it with a 121 fs, 155pJ pulse centered at 1550nm. The resulting supercontinuum is shown to have RIN between 1-2%, which is very close to the laser RIN of 1%. Furthermore, the ANDi waveguide generates a supercontinuum with smooth spectrum, with the full bandwidth being inside a 20dB region. It is numerically shown that the dips in the measured supercontinuum is caused by the uneven shape of the input laser pulse. Simulations of RIN and SC, based on the measured dispersion, confirms this behaviour. Next a 20cm anomalous dispersion spiral waveguide is pumped in the same setup. The RIN and SC were measured as a function of input pulse power, and while propagation after soliton fission allows for a broader and more smooth spectrum, it introduces a very high RIN. At maximum power the RIN is around 50%. The smoothness of the spectrum is caused by the OSA averaging many pulses from the laser. The increase in RIN with input power is also observed in the DWs, but not as strongly as in the rest of the spectrum. It is further observed that right after soliton fission the anomalous waveguide supercontinuum has similar low noise as the ANDi SC. A comparison between the anomalous dispersion SC at fission and ANDi at full power show that while similar noise properties can be obtained, the anomalous SC suffers from most of broadening being from dispersive wave phasematching, which limit the spectrum in the regions between the pump and the dispersive waves. Nevertheless, the generated supercontinuum in the anomalous waveguide still generates wavelengths from 1-2um, and therefore outperforms the ANDi WG in terms of bandwidth. Interestingly, this octave spanning SC is generated with low pulse energy of 22pJ. The general behaviour of both the waveguides is confirmed numerically. The experiment and simulation is repeated for the order of magnitude smaller waveguides with a length of 2.3cm. It is concluded that the anomalous waveguide has low noise at soliton fission, but the RIN increases afterwards. Simulations of the RIN show a increased noise in the regions between the DWs and the soliton. This could not be confirmed experimentally, because of the lack of power. Additionally, a hybrid

waveguide is examined. This waveguide has a zero dispersion wavelength very close to the pump wavelength of 1550 nm. An octave spanning SC is generated, vastly outperforming the short ANDi waveguide in broadening. The hybrid waveguide has an a small increasing in noise overall to around 3% but towards the edges of the spectrum this increases rapidly. Also high RIN is observed at 1500nm in both simulation and experiment. Interestingly, this waveguide has a smoother spectrum than the anomalous waveguide, and requires lower pulse energies than the ANDi waveguide, but to suffers from an increased noise.

Finally, a numerical examination of using longer pulses for pumping ANDi waveguides is performed. Using pulses between 100fs to 2 ps, it is shown that very similar SC can be generated. The generated SC are independent of the input pulses width, and retains spectral flatness. It further shown that the limiting factor for long pulse pumping, is the Raman effect. By sweeping the Raman fraction and input pulse width, a map of the weighted average RIN is calculated. Even for Raman parameters similar to silica, a 600fs pump can be used while retaining low noise. For weaker Raman effects, it is shown that pulses as long as 1 to 2 ps can be used. The ANDi waveguide outperforms anomalous dispersion waveguides even if a strong Raman effect is included.

CHAPTER 6

Pumping Close to the Zero Dispersion Wavelengths: Directional Supercontinuum

6.1 Background

This chapter is a reprint of the paper Christensen et al. [36]. The reprint permission is found in Appendix A. In this paper, the waveguide dispersion is normal dispersion at the pump wavelength, but it resides close to the ZDW. Therefore, the broadening is a combination SPM and OWB in the normal dispersion region, and of soliton dynamics in the anomalous dispersion region. It shown that this combination of effects can be used to broaden the SC through the anomalous dispersion regime into another normal dispersion regime. This dispersion profile is of special interests as it is a combination of the normal and anomalous dispersion regimes which where investigated earlier.

6.2 Abstract

In this paper we numerically study supercontinuum generation by pumping a silicon nitride waveguide, with two zero-dispersion wavelengths, with femtosecond pulses. The waveguide dispersion is designed so that the pump pulse is in the normal dispersion regime. We show that because of self phase modulation, the initial pulse broadens into the anomalous dispersion regime, which is sandwiched between the two normal-dispersion regimes, and here a soliton is formed. The interaction of the

soliton and the broadened pulse in the normal dispersion regime causes additional spectral broadening through formation of dispersive waves by non-degenerate four-wave mixing and cross phase modulation. This broadening occurs mainly towards the second normal dispersion regime. We show that pumping in either normal dispersion regime allows broadening towards the other normal dispersion regime. This ability to steer the continuum extension towards the direction of the other normal dispersion regime, beyond the sandwiched anomalous dispersion regime underlies the directional supercontinuum notation. We numerically confirm the approach in a standard silica microstructured fiber geometry with two zero dispersion wavelengths.

6.3 Introduction

In the last two decades research in supercontinuum generation (SCG) has gained a massive amount of interest. Especially the use of highly confining waveguides has revolutionized the field. The two major platforms in play are microstructured fibers (MSF) and waveguides in nonlinear materials. Here we focus on SCG using femtosecond (fs) pump pulses because it can provide very low noise [6, 107]. Two key regions are important when considering group velocity dispersion (β_2) of the waveguide: the anomalous dispersion region (ADR), $\beta_2 < 0$ and the normal dispersion region (NDR), $\beta_2 > 0$. SCG with fs pulses in the NDR is caused by self-phase modulation (SPM) in the early stage and so-called optical wave-breaking in the later stage, a process caused by an interplay of chromatic dispersion and four-wave mixing (FWM) between the newly generated spectral components and the undepleted pump. This results in a simple spectral and temporal shape [89, 108]. SCG with fs pulses in the ADR is governed by solitons, whose interactions lead to a large bandwidth SC, but often a complex spectral and temporal shape. Dispersive waves (DWs) are one of the key effects when generating SC in the ADR [109–112]. The DWs are generated by degenerate FWM of the soliton photons, and are generally phase matched outside the ADR. This significantly extends the SC bandwidth. The DW part of a supercontinuum (SC) has been used in many applications, such as confocal microscopy [113], frequency combs [114], lidar [115] and spectroscopy [116].

A general quest is to broaden the SC, perhaps even towards non-traditional wavelength regimes. There has been significant effort in using the interaction between two pump pulses or solitons [117, 118], and between a soliton and a dispersive wave [119–122]. Two pulse collision by means of a soliton and a dispersive wave was theoretically shown to produce a coherent SC, which enables the compression of the spectrum. This was achieved by using cross phase modulation (XPM) between waves as the broadening mechanism, therefore avoiding soliton fission and modulation stability [123]. The effect of XPM on Raman solitons was investigated in [124] and the shift was shown to depend on the dispersion slope of the fiber. Two color pulse collisions were also studied as event horizon analogies [125–127] and for making an all-optical transistor [128]. A key weakness of these schemes is the need for two input pulses, which complicates them. Here we show that using a single pump pulse in the NDR leads to a soliton

in the ADR. The interaction of the NDR pulse and the ADR soliton share great similarity with the two color studies. A similar idea based on an input pulse of dark solitons was investigated in [129]. An interesting prospect would be to use DWs to enhance the SC bandwidth and extend it into new regions when pumping in the NDR. While it was shown to be possible to generate DWs even without solitons [130–133], the generated DWs are extremely weak. However, an interesting recent experiment used a silicon nitride waveguide with two zero dispersion wavelengths (ZDW) [134]: here the ADR is sandwiched between two NDRs. When pumped in the IR NDR, the authors found a cascade process eventually generated DWs in the visible NDR. It was also shown that the generated spectrum is coherent. The cascade process was explained by considering dispersive waves generated by both the initial pulse and a compressed dispersive wave in the ADR. Here we investigate this scheme further and show that wave interaction in the ADR plays an important role. The starting point was silicon-rich nitride (SiRN) waveguides with two ZDWs. In such a waveguide one of us recently experimentally observed a continuum generating when pumping in the IR NDR [33]. Numerical simulations (not published) indeed indicated a similar behavior as later found in [134], namely a directional extension of the SC into the second NDR in the visible. This coins the phrase directional SCG and in this work we use numerical simulations to investigate the nonlinear processes behind directional SCG. We find that the edge of the SPM broadened pump pulse in the NDR will leak into the ADR, in which solitons can form. The soliton will then be repulsed from the ZDW and move across the ADR, which happens due to XPM from the pulse in the NDR. It is the degenerate and non-degenerate FWM between the soliton and the continuum in the pump NDR that will lead to the formation of DWs with significant spectral densities in the second NDR. By choosing to pump in the NDR located either at shorter or longer wavelength than the ADR, one can "direct" the SCG process towards the other NDR.

We show that by tailoring the SiRN waveguide dispersion profile a 1.3 octave SC spanning from $0.750 \mu\text{m}$ to $1.85 \mu\text{m}$ can be generated by using a $1.56 \mu\text{m}$ femtosecond pump laser. Importantly, the same waveguide generates a SC from $0.750 \mu\text{m}$ to $2.0 \mu\text{m}$ when pumped at $0.94 \mu\text{m}$, i.e. when the SCG process is directed towards the longer wavelengths. The similar bandwidth with very different input wavelengths clearly demonstrates the directional broadening of the scheme. It is shown that the chosen dispersion profile allows for the generation of two pulse interactions by generating a soliton in the ADR, even when pumped in the NDR. To show the generality of the scheme a silica MSF geometry is simulated and nonlinear interactions, similar to that in the waveguide is observed. As the spectrum mainly broadens through the ADR, the direction of the spectral broadening can be controlled by either changing the pump wavelength or the dispersion profile of the waveguide. The tunability of the spectrum allows the generation of broadband spectrum in the spectral area needed for a specific application.

6.4 Numerical simulations

The directional SCG process was studied by numerically solving the generalized non-linear Schrödinger equation (GNLSE) [48]. The time domain GNLSE with electric field envelope $A(z, T)$ and $\tilde{A}(z, \omega)$ is transformed to frequency domain interaction picture (IP) [135]. The electric field envelope in the IP is denoted by $C(z, T)$ and $\tilde{C}(z, \omega)$. The relation to $\tilde{A}(z, \omega)$ is $\tilde{C}(z, \omega) = [A_{eff}(\omega)/A_{eff}(\omega_0)]^{-\frac{1}{4}} \tilde{A}(z, \omega)$. Here z is the propagation distance, ω is the angular frequency, ω_0 is the angular frequency at the pump and A_{eff} is the effective area.

The GNLSE in the IP can be written as Eq. (6.1) [46, 47].

$$\begin{aligned} \frac{\partial \tilde{C}}{\partial z} - i\{\beta(\omega) - [\beta(\omega_0) + \beta_1(\omega_0)(\omega - \omega_0)]\} \tilde{C} + \frac{\alpha(\omega)}{2} \tilde{C} \\ = i\bar{\gamma}(\omega) \left[1 + \frac{\omega - \omega_0}{\omega_0}\right] \mathcal{F} \left\{ C \int_{-\infty}^{\infty} R(T') |C(T - T')|^2 dT' \right\} \end{aligned} \quad (6.1)$$

Here T is the time in the frame co-moving with the pump, \mathcal{F} denotes the Fourier transform operator, $\beta(\omega)$ is the propagation constant, β_1 is the inverse pump group velocity, $\alpha(\omega)$ is the linear loss coefficient, $\bar{\gamma}(\omega)$ is the modified nonlinear coefficient all as a function of frequency,

$$\bar{\gamma}(\omega) = \frac{n_2 n_0 \omega_0}{c n_{eff}(\omega) \sqrt{A_{eff}(\omega) A_{eff}(\omega_0)}}. \quad (6.2)$$

$$A_{eff} = \frac{(\int \int_{-\infty}^{\infty} |F(x, y)|^2 dx dy)^2}{\int \int_{-\infty}^{\infty} |F(x, y)|^4 dx dy} \quad (6.3)$$

In the case of the waveguide, the nonlinear coefficient has to include the vectorial components, and it is calculated following [43]. For the fiber the definition in equation 6.3 is used. Note that when the effective area (A_{eff}), and the effective refractive index (n_{eff}) are independent of the frequency, $\bar{\gamma}(\omega)$ becomes the usual nonlinear coefficient $\gamma = \frac{n_2 \omega_0}{c A_{eff}(\omega_0)}$. n_2 is the nonlinear refractive index of the material, $n_0 = n_{eff}(\omega_0)$ and c is the speed of light in free space. $R(T)$ is the material response function, with a single Lorentzian lineshape model, $R(T) = (1 - f_R)\delta(T) + f_R(\tau_1^{-2} + \tau_2^{-2})\tau_1 \exp(-T/\tau_2) \sin(T/\tau_1)$. Where f_R is the fractional contribution of the delayed Raman response τ_1 is the Raman oscillation period and τ_2 is the Raman decay time. The pulse evolution is found by solving Eq. (6.1), using an ODE solver.

6.4.1 Silicon-rich nitride waveguide

The waveguide considered here is a 900 by 650 nm SiRN waveguide using the composition characterized by a DCS:NH₃ gas ratio of 3.9 [82]. The SiRN waveguide has a γ of 2.9 W⁻¹m⁻¹ at 1.56 μ m. The Raman effect was also modeled [48]. We use a single Lorentzian lineshape model with $f_R = 0.2$, $\tau_1 = 13$ fs, and $\tau_2 = 150$ fs [33]. The

dispersion profile of the waveguide is optimized to ensure that the 1.56 μm pump laser is in the NDR, but close to the ADR. The waveguide and dispersion profile of interest are shown in Fig. 6.1. The modes were found by using Comsol Multiphysics. The ZDWs are located at 1.02 μm and 1.47 μm . For convenience the wavelength region below 1.02 μm is called NDR I, the wavelength region between 1.02 μm and 1.47 μm is called ADR I and the wavelength region above 1.47 μm is called NDR II as labeled in Fig. 6.1. The circles mark the two pump wavelengths used in the simulations, 1.56 μm and 0.94 μm . A wavelength independent loss of 1.35 dB/cm is used in the simulations [32, 33].

The input pulse considered for the study has a sech² profile with time domain full width at half maximum (T_{FWHM}) of 125 fs and a pulse energy of 82 pJ (58 W peak power) centered at 1.56 μm . The repetition rate used is 90 MHz, which is used to calculate the power spectral density. The spectral evolution along the length of the waveguide is plotted in Fig. 6.2(b). Initially the spectrum broadens from SPM in NDR II and the shorter wavelength part of the spectrum leaks into the ADR I. The leaked pulse will in the ADR I develop into a soliton, which is subsequently repelled from the NDR II continuum. The repulsion can be explained by the cross phase modulation (XPM) between the two pulses [127], resulting in the frequency change

$$\partial\omega(T) \propto -\frac{\gamma_1 L}{\pi} \frac{\partial}{\partial T} |A_2(L, T)|^2 \quad (6.4)$$

where L is the interaction length for the two pulses, $\partial\omega(T)$ denotes change in instantaneous frequency of the first pulse, γ_1 is the nonlinear coefficient at the wavelength of the first pulse. $|A_2|^2$ is the power of the second pulse. As seen by the derivative in Eq. (6.4), the change in the frequency caused by the interaction with the second

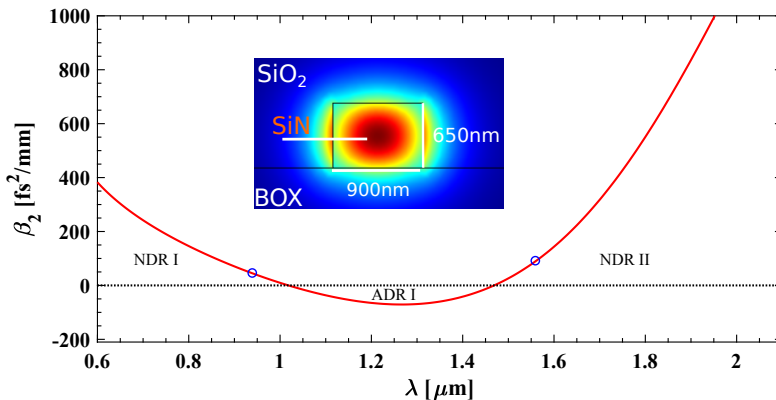


Figure 6.1: GVD (β_2) for the SiRN waveguide. The circles mark the pump wavelengths used in the paper. The inset represents the Comsol simulation of the waveguide and the mode obtained.

pulse depends on the whether the interaction happens at the leading or the trailing edge of the second pulse. By properly locating (delaying or advancing) the ADR pulse with respect to the NDR pulse, efficient blue-shift or red-shift of the ADR pulse is achieved. As seen in figure 6.2 (d) the soliton overlaps in time domain with trailing edge of the NDR II pulse, therefore the soliton blue shifts because of XPM. As the soliton reaches the edge of the ADR I it sees a barrier [136] and the soliton stops blue shifting. By this time the initial pump pulse in the NDR II has temporally spread, greatly reducing the peak power. Therefore the XPM felt by the soliton is reduced. At around $z = 22$ mm we see the formation of several DWs. Generation of DWs by a soliton is controlled by phase matching conditions. A consequence of the specific phase matching condition is that the DWs are generated outside the ADR. The soliton only phase matches one DW on each side of the ADR. Therefore it is observed that DWs from the soliton alone do not explain all the DWs present in the spectrum. Here we explain the origin of the new DWs as nondegenerate FWM of the soliton and the pulse in the NDR II. The phase matching conditions of both the degenerate and nondegenerate case is given by [137]

$$\beta_{lin}(\omega_d) = J[\beta_{lin}(\omega_p) - \beta_{sol}(\omega_p)] + \beta_{sol}(\omega_d); \text{ for } J = -1, 0, 1 \quad (6.5)$$

$$\text{where, } \beta_{sol}(\omega) = \beta_{lin}(\omega_s) + \beta_1(\omega_s)[\omega - \omega_s] + q_{sol} \quad (6.6)$$

Here β_{lin} is the dispersion relation of the medium, ω_p denotes the center of the broadened pump spectrum that overlaps with the soliton in time, ω_s denotes the center frequency of the soliton, ω_d denotes the frequency of the DW and q_{sol} is the soliton wavenumber. q_{sol} has negligible contribution towards the calculated phase matching wavelengths and is not included in the calculations.

The phase matching points for the case at $z = 22$ mm is graphically represented in Fig. 6.2(c). The points intersecting the dispersion relation of the waveguide in the soliton's group velocity frame ($\beta_{lin}(\omega) - \beta_1(\omega_s)[\omega - \omega_s]$) with the $J = 0$ line are the wavelengths at which the DWs directly from the soliton are generated. The empty circles plotted in Fig. 6.2(b) marks the calculated phase matching points where the DWs are expected to be generated. It can be seen that calculated points agree very well with the DWs that are generated. The phase matching wavelength obtained from $J = -1$ condition is marked as triangles pointing down in Fig. 6.2(b). It is important to note the presence of another DW at a shorter wavelength, in NDR I next to the one generated by the soliton. This DW is the result of non-degenerate FWM of the soliton at $1.120 \mu\text{m}$ and the part of the pump that overlaps in time at $1.635 \mu\text{m}$ which leads to a phase matching at $0.772 \mu\text{m}$. It can be seen that $J = -1$ condition explains very well the origin of the DW next to the soliton's DW. The spectrum obtained after 40 mm is plotted in Fig. 6.2(a). The spectrum at the end of the waveguide spans from 0.750 to $1.85 \mu\text{m}$. 290 nm broadening towards the longer wavelengths, and 790 nm towards the shorter wavelengths from the $1.56 \mu\text{m}$ pump. An enhanced spectral broadening towards the shorter wavelengths is observed. The directionality of the broadening is caused by the blue shifting of the wavelengths in the ADR, and the emission of DW in the visible wavelengths.

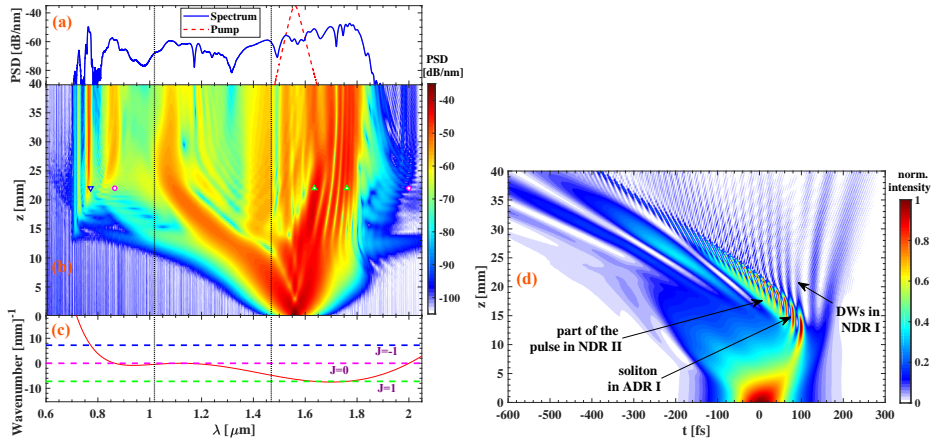


Figure 6.2: Directional SCG in the SiRN waveguide pumped at $1.56 \mu\text{m}$ with 0.58 kW peak power. (a) The power-spectral density (PSD) at the beginning (dashed) and end of the SiRN waveguide (full). (b) The spectral evolution in the waveguide as a function of propagation distance, along with the phase matched wavelengths from Eq. (6.5) after 22 mm of propagation in the waveguide, marked as downward pointing triangle ($J = -1$), empty circles ($J = 0$), and triangles pointing upwards ($J = 1$). (c) Dispersion relation of the waveguide in the soliton's group velocity frame (full). The dashed line are the wavenumbers for $J = -1, 0, 1$ cases as labeled. The dotted lines in all the figures are the ZDWs. (d) Temporal evolution in the waveguide. Key spectral regions are marked.

In Fig. 6.3 we show a calculated spectrogram at 22 mm propagation distance. At this stage the continuum in NDR II is well developed, and the blue trailing front has leaked into the ADR, generating the soliton. The soliton has experienced repulsion from the long-wavelength ZDW. Also, being on the other side of the ZDW its group velocity has increased, so it is no longer overlapping with the tail of the continuum, but is moving towards the center. At this stage it has already generated several DWs in NDR I. In the plot we also show the accumulated dispersion delay $T(\omega, z) = [\beta_1(\omega) - \beta_1(\omega_0)]z$ where $\beta_1(\omega)$ is the frequency-dependent inverse group velocity. This line indicates where the colors will be if they were all injected at $z = 0$. Observing this line, it is clear that this allows the soliton to eventually interact with the entire continuum as it propagates along the waveguide: as the leaking front enters the ADR, the pulse will namely experience an acceleration and thereby be pulled through the continuum from the trailing to the leading edge. It is during this process that XPM between the continuum and the soliton will keep transferring energy to the DWs in NDR I.

In the initial reporting on directional SCG [134], the process was interpreted as

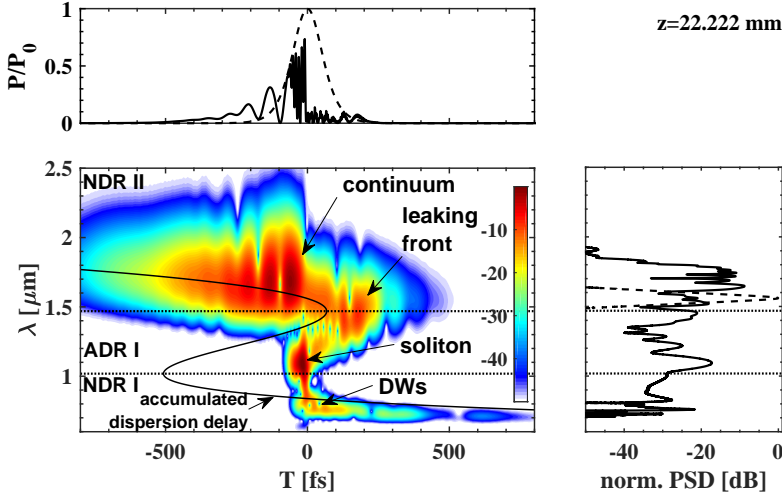


Figure 6.3: Spectrogram at 22 mm calculated with a 16 fs gating pulse. The full black line shows the accumulated dispersion delay.

a cascade DW phenomenon. Below it will be argued that exciting a soliton in the ADR is important for understanding the outcome of the phase-matching conditions. To confirm this, the launching of two pulses were implemented in our simulations. As a test case we modeled the collision of a strong pump in the NDR with an $N = 1$ soliton in the ADR, where N is the soliton order. Specifically, we simulated a 20 pJ 125 fs Gaussian pulse (140 W peak power) centered at $1.56 \mu\text{m}$ in NDR II colliding with a 2.5 pJ 55 fs soliton pulse (40 W peak power) centered at $1.25 \mu\text{m}$ in the ADR I. The low power is chosen for clarity of the interactions. The pulses are initially offset by 100 fs.

Fig. 6.4(b) shows the spectral evolution of the two pulses as they interact in the waveguide. First we see that the pulse in NDR II broadens to a continuum because of SPM, at the same time the soliton in the ADR I is blue shifted towards shorter wavelengths. This happens as the soliton is overlapping with the trailing edge of the pulse in NDR II. Therefore the XPM induced spectral chirp is towards the short wavelengths. At around $z = 12$ mm a clear peak emerges at $1.8 \mu\text{m}$, which is the typical shoulder found after the onset of wave-breaking of the red pulse front of the NDR I non-solitonic continuum. This process occurs due to FWM between the SPM-broadened continuum and the un-depleted pump that is temporally broadened due to dispersion. Later, at around $z = 15$ mm the soliton completely overlaps with the pump and we observe the generation in NDR I of a strong DW below 800 nm. This is the non-degenerate FWM case with $J = -1$ between the soliton and the SPM-broadened pulse in the NDR II regime. The process quickly saturates when the latter depletes and all the photons are converted into the continuum [108]. At $z = 25$ mm

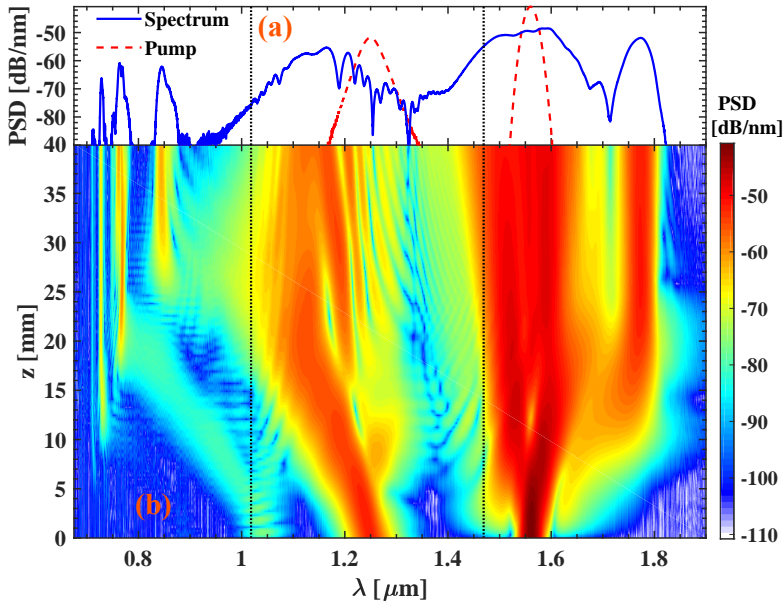


Figure 6.4: Two-pulse model where the SiRN waveguide is pumped at $1.56 \mu\text{m}$ with 125 fs 140 W peak power and a soliton state is injected at $1.25 \mu\text{m}$ with 55 fs 40 W peak power. (a) Spectrum at the output of the SiRN waveguide (full) and the input (dashed). (b) Simulation of spectral evolution of a fundamental soliton colliding with a pulse in the NDR II. The vertical dotted lines mark the ZDWs in both the figures.

the soliton emits another dispersive wave caused by degenerate FWM. The overall evolution is similar to the evolution in the single pulse simulation seen in Fig. 6.2. Fig. 6.4(a) shows the spectrum (full) after 40 mm of propagation in the waveguide, and qualitatively the generated spectrum is similar to the single pump spectrum, both in terms of bandwidth and spectral shape with DWs in the $0.70\text{--}0.90 \mu\text{m}$ region, and a bandwidth from $0.70 \mu\text{m}$ to $1.85 \mu\text{m}$. This confirms our interpretation that the spectral broadening observed in the single pulse simulation is well understood by considering the two color interactions between a soliton in the ADR I and a non-solitonic continuum in NDR II.

We have observed that the $1.56 \mu\text{m}$ pulse propagating through the waveguide broadens towards the visible. To investigate the cause of directionality of the SCG, the wavelength of the single pulse simulation is now changed to $0.94 \mu\text{m}$, with $T_{FWHM} = 125 \text{ fs}$ and 0.70 kW peak power. The spectral evolution and final spectrum can be seen in Fig. 6.5. Similar to the $1.56 \mu\text{m}$ case, the spectrum initially broadens because of SPM in NDR I. As it broadens it spreads into the ADR I. At $z = 13 \text{ mm}$ the pulse in the ADR separates into two distinct peaks, and a DW with a wavelength of $2.0 \mu\text{m}$

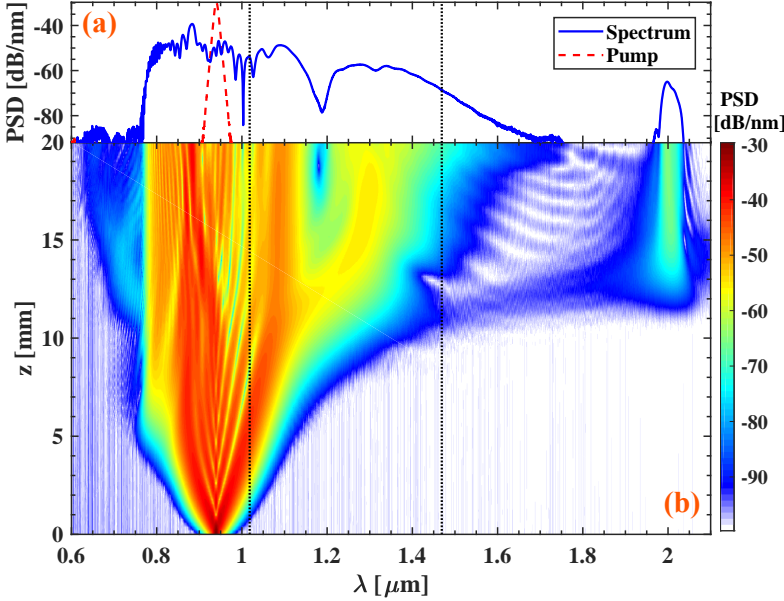


Figure 6.5: Directional SCG in the SiRN waveguide pumped at $0.94 \mu\text{m}$ with 0.7 kW peak power. (a) Spectrum at the end of the waveguide (full) and the pump (dashed). (b) The spectrum evolution in the waveguide as a function of propagation distance for the waveguide pumped at $0.94 \mu\text{m}$. The vertical dashed lines marks the ZDWs in both the figures. For this pump wavelength the nonlinear coefficient is $\gamma = 7.2 \text{ W}^{-1}\text{m}^{-1}$.

is created by FWM between the ADR peak and the NDR pulse. The second peak is red shifted by XPM to $1.30 \mu\text{m}$. The final spectrum has a bandwidth from $0.80 \mu\text{m}$ to $2.0 \mu\text{m}$. This gives a broadening of 140 nm towards the shorter wavelengths, and 1060 nm broadening towards the longer wavelength. Less power is transferred into the region between the IR dispersive wave and the $1.47 \mu\text{m}$ ZDW. A similar spectral evolution as in the $1.56 \mu\text{m}$ case is observed, but this time it is directed towards the IR. From this it is concluded that the spectrum mainly broadens towards the direction of the ADR.

6.4.2 Microstructured fiber

MSFs have facilitated the study of SCG owing to the flexibility in obtaining a desired dispersion profile and ease in handling the fibers. SCG with fiber as a nonlinear medium has an additional advantage that it can be used to build an all fiber compact set up with ease of alignment and portability. Due to their wide spread use

in telecommunications various silica fiber fabrication techniques are well understood. Silica fibers can have a low loss transmission window from $0.4 \mu\text{m}$ to $2.0 \mu\text{m}$. Thus silica MSF would be a natural choice for study of directional SC using a table top femtosecond fiber laser at $1.56 \mu\text{m}$. To extend our understanding to that of fibers, we here analyze directional SC in a silica fiber with a dispersion profile similar to that studied in the SiRN waveguide.

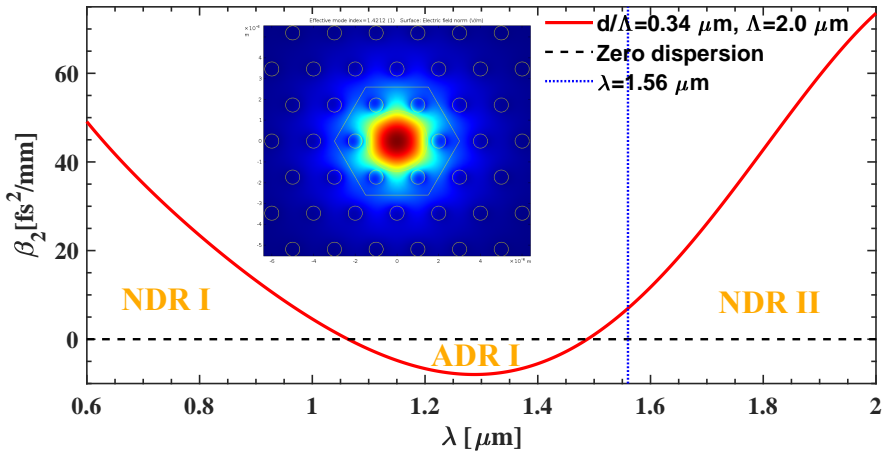


Figure 6.6: GVD (β_2) of the MSF as a function of wavelength. The dashed horizontal line is the zero dispersion and the dotted vertical line marks the pump wavelength at $1.56 \mu\text{m}$. The inset represents the Comsol simulation of the fiber and the mode obtained.

The pure silica fiber we consider has a pitch (Λ) of $2.0 \mu\text{m}$ and a hole diameter (d) of $0.680 \mu\text{m}$. The modes in the fiber were found by using Comsol Multiphysics. The numerically calculated dispersion of the fiber is plotted in Fig. 6.6, the fiber has ZDWs at $1.063 \mu\text{m}$ and $1.488 \mu\text{m}$ as shown in Fig. 6.6. The fiber has a γ of $7.65 \text{ W}^{-1}\text{km}^{-1}$ and an A_{eff} of $13.8 \mu\text{m}^2$ at the pump wavelength of $1.56 \mu\text{m}$. Both the material loss and the confinement loss of the fiber were included in the GNLSE. The material loss accounts for the loss arising from pure silica as described in [138].

The GNLSE is solved in the frequency domain IP as done in the case of waveguide discussed previously. The complete $\beta(\omega)$ profile is included and $f_R = 0.18$, $\tau_1 = 12.2 \text{ fs}$, and $\tau_2 = 32 \text{ fs}$ are used [139]. The same pump pulse configuration as in the SiRN case was used, except now the peak input power is 9 kW , corresponding to a pulse energy of 1.28 nJ . The spectrum obtained after 1 m of the fiber is plotted in Fig. 6.7(a), while (b) shows the spectral evolution.

Fig. 6.7(c) shows the plot of dispersion relation of the fiber in the soliton's group velocity frame. The center wavelength of the soliton is $1.20 \mu\text{m}$ at 0.5 m of the fiber. The distinct features of the spectral evolution shown in Fig. 6.7(b) can be explained as follows. The pump is in the NDR II and the spectrum initially broadens from SPM.

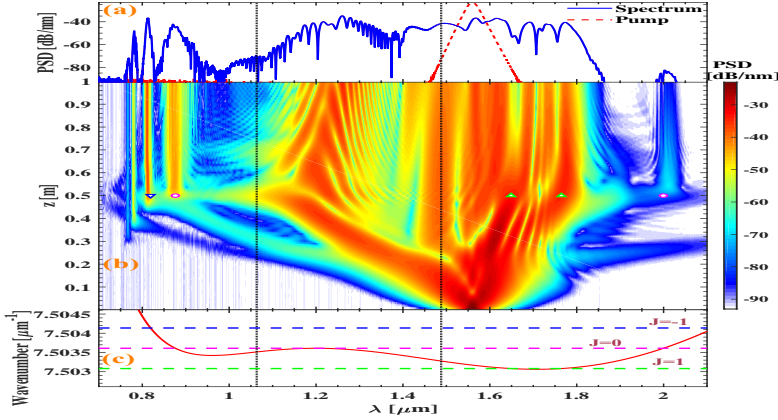


Figure 6.7: Directional SCG in an MSF pumped at $1.56 \mu\text{m}$ with 9 kW peak power. (a) The PSD at the beginning (dashed) and end of the fiber (full) (b) Spectral evolution along the length of the fiber. The empty circle at $0.876 \mu\text{m}$ and $1.999 \mu\text{m}$ are the calculated wavelength at which the DWs are generated from phase matching condition for the soliton at $1.20 \mu\text{m}$ alone, after 0.5 m of propagation in the fiber. The downward pointing triangle at $0.819 \mu\text{m}$ is the calculated wavelength with $J = -1$ condition in Eq. (6.5), at which DW are generated from the non-degenerate FWM of the part of the pump at $1.649 \mu\text{m}$ in the NDR II and the soliton after 0.5 m of the fiber. The triangles pointing upwards at $1.649 \mu\text{m}$ and $1.765 \mu\text{m}$ are the calculated wavelength with $J = 1$ condition in equation 6.5, at which DW are generated after 0.5 m of the fiber. (c) Dispersion relation of the waveguide in the soliton's group velocity frame after 0.5 m of propagation in the fiber(full). The dashed lines are the wavenumbers for $J = -1, 0, 1$ cases as labeled. The intersection points between the full line and the dashed lines are calculated phase matching wavelengths for the generation of DWs. The dotted vertical lines in all three figures are the ZDWs.

A part of the spectrum spreads into the ADR I and develops into a soliton. Initially the soliton blue shifts from XPM induced from a part of the pump in NDR II that overlaps in time. The soliton shifts towards the shorter ZDW. After around 0.5 m of propagation four DWs are generated, two on NDR I and two in NDR II. Further propagation spreads out the power in the NDR II and the soliton does not experience XPM from the pulse in the NDR II region anymore. The soliton, which is at the edge of the ADR I, begins to red shift from Raman induced self frequency shift. As in the case of the waveguide the DWs from the soliton alone does not explain all the DWs observed in the spectral evolution at 0.5 m of propagation in the fiber, as can be seen in Fig. 6.7(b). The new DWs are well explained by considering them as DWs generated

from the nondegenerate FWM of the part of the pump at $1.649 \mu\text{m}$ in NDR II that overlaps in time with the soliton at $1.20 \mu\text{m}$. This is shown in Eq. (6.5) and explained in Fig. 6.7. It is interesting to note that the band of wavelength generated at around $1.75 \mu\text{m}$ can be explained as a dispersive wave generated from the nondegenerate FWM of the soliton at $1.20 \mu\text{m}$ and the part of the pump that overlaps in time at $1.649 \mu\text{m}$. To further study the effect of XPM induced by the part of pump pulse in

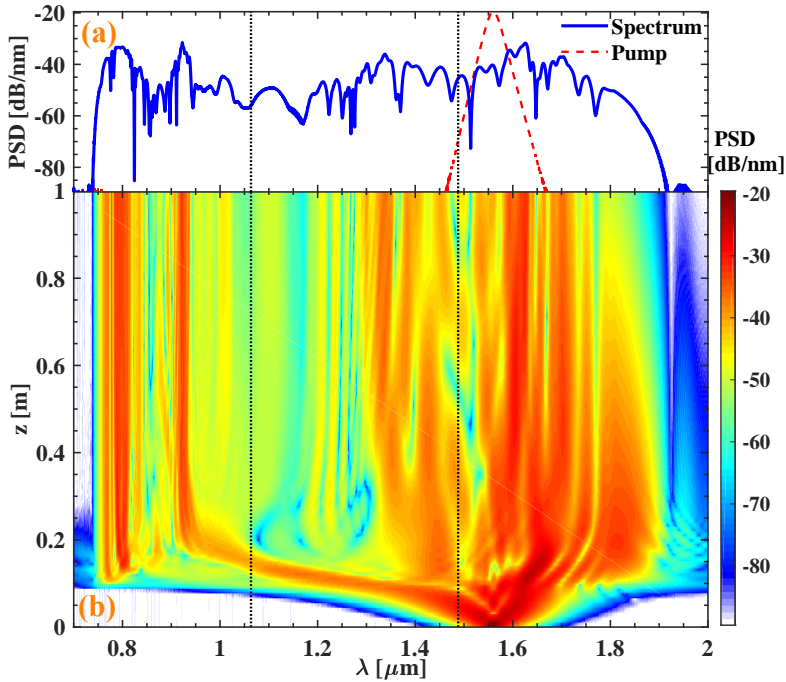


Figure 6.8: Directional SCG in an MSF pumped at $1.56 \mu\text{m}$ with 20 kW peak power. (a) The PSD at the beginning (dashed) and end of the MSF (full). (b) Spectral evolution along 1 m of the fiber. The vertical dotted lines in both the figures are the ZDWs.

the NDR II overlapping in time with the soliton, the peak power is increased to 20 kW with all the other parameters remaining the same. The spectrum obtained after propagating 1 m of fiber is plotted in Fig. 6.8(a) and the spectral evolution is shown (b). It can be observed that similar to the 9 kW case the spectrum initially broadens from SPM in NDR II and a part of the spectrum spreads in to the ADR I. There it forms a soliton, which is repulsed by XPM from the NDR II continuum resulting in a soliton blue shift just like in the previous cases. The spectrogram at $z = 0.122$ m in the fiber is shown in Fig. 6.9(a). It can be seen from the Fig. 6.9(a) that the co-propagating broad pulse in NDR II overlaps in time with the soliton in ADR I

and that it emits DW's on the short wavelength side. The spectrogram calculated at $z=0.122$ m is bandpass filtered from $1.1 \mu\text{m}$ to $1.5 \mu\text{m}$ to see the pulse in ADR I. The temporal profile and the spectrogram in Fig. 6.9 (c) shows that the pulse at $1.16 \mu\text{m}$ is indeed a soliton. Interestingly, as the soliton encounters the ZDW barrier, it does not recoil as seen in the previous cases, but continues through. This can be qualitatively explained as follows: Compared to the 9 kW case the repulsion velocity in this case is much higher as a higher peak power (20 kW) is launched into the fiber. This makes the pulse in NDR II much stronger than in the 9 kW case. Thus the XPM experienced by the soliton is much greater, resulting in a higher repulsion velocity towards the shorter wavelengths. The spectrogram in Fig. 6.9(b) shows the soliton being 'pushed' into the NDR I. Once in NDR I the pulse continues to blue shift until the power in the NDR II spreads out and there is no more XPM experienced by the pulse. As more of the spectrum from the NDR II spreads into the ADR I it develops into solitons and gradually red shift from Raman induced self frequency shift.

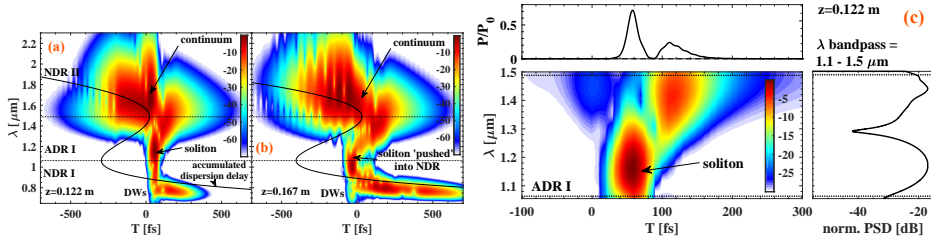


Figure 6.9: Spectrograms for an input peak power of 20 kW calculated with a gating function of 20 fs: (a) at $z=0.122$ m, shows the soliton in the ADR I and the co-propagating pulse in NDR II (b) at $z=0.167$ m, shows the soliton being pushed into the NDR I. (c) Spectrogram numerically bandpass filtered from $1.1 \mu\text{m}$ to $1.5 \mu\text{m}$ to show the spectral and temporal profile in the ADR I at $z=0.122$ m.

A future challenge is to understand why the soliton passes the ZDW barrier and how come it does not recoil: we did confirm that it is a soliton in the ADR that we see in the spectrum as shown in Fig. 6.9(c), but as soon as it encounters the ZDW it passes through and starts developing a chirp due to the normal dispersion. A possible explanation is that due to the higher repulsion velocity the soliton encounters the ZDW at a more rapid pace than the previous cases, and while it starts to shed energy into the DW just above $0.8 \mu\text{m}$ in NDR I, the accompanying spectral recoil is not enough to stop the soliton from passing the ZDW.

6.5 Conclusion

We have investigated a directional SCG scheme where the waveguide has an anomalous dispersion region (ADR) surrounded by two normal dispersion regions (NDRs).

When pumping in one of the NDRs, the SC broadening is directed mainly through the ADR and towards the other NDR. This directional broadening is shown to be caused by a 3-step process: First, since the pump is in the NDR, it broadens due to SPM into a typical normal-dispersion continuum where each pulse front broadens both spectrally and temporally. The second step is when one of the pulse fronts reaches the ZDW. It leaks into the ADR, and a soliton forms in the ADR as the anomalous dispersion compensates for the accumulated nonlinear phase. The soliton is repulsed spectrally from the continuum in the NDR due to XPM between them. The third step is formation of DWs in the other NDR, which occurs either as direct FWM with the soliton or as non-degenerate FWM between the soliton and the continuum in the other NDR (i.e. an XPM-initiated process). In this process the soliton repulsion is stopped and it recoils at the second ZDW.

The directional SCG process was investigated through numerical simulations in a silicon-rich nitride waveguide with the ADR between 1.02-1.47 μm . We found that when pumping at 1.56 μm with a femtosecond laser, the SC was directed towards shorter wavelengths, while when using a 0.94 μm femtosecond pump the SC was directed towards longer wavelengths. To show the generality of the scheme, we also showed simulations of a MSF fiber geometry based on conventional silica fiber technology, where the hole pitch and diameter are selected to give a similar dispersion landscape. Qualitatively identical results were obtained concerning the nonlinear dynamics, with the main differences stemming from the different dispersion profiles. Finally we also investigated using a higher pump power, and found that the soliton gained a stronger repulsion velocity and higher peak power, and instead of recoiling at the other ZDW it simply crosses the ZDW into the NDR. It remains to be discovered exactly why this happens, it is believed to be caused by the high repulsion velocity not allowing the soliton to emit enough dispersive waves for the spectral recoil to overcome the XPM repulsion.

One main conclusion is that directional SCG is observable both in fibers and integrated photonics waveguides. This is welcome since these nonlinear platforms offer complementary solutions (transverse size, length, nonlinearity, dispersion engineering) for different communities. By choosing a suitable dispersion profile and using the required pump power this technique could be used as a method to efficiently transfer pump power into a given wavelength region of interest. One exciting prospect could be to design the dispersion such that the ADR lies above the 1.56 μm pump wavelength, either in a SiRN waveguide or a soft-glass MSF. The SC would then directionally broaden towards the mid-IR where both of these waveguides have transmission.

6.6 Funding Information

European Union's Horizon 2020 research and innovation program under the Marie Skłodowska-Curie grant agreement No. 722380 (SUPUVIR).

CHAPTER 7

Conclusion

The main goal of this thesis was to investigate how the different dispersion profiles influenced the SCG in SiN waveguides. This work resulted in three major topics of research.

In chapter 4 SCG in the anomalous dispersion regime was investigated with the key goal of generating wavelengths in the MID-IR. It was numerically shown that by adjusting the silicon content in SiN from Si_3N_4 to SiN8, the DW in the MID-IR can be tuned from $3.4 \mu\text{m}$ in Si_3N_4 , to $4.1 \mu\text{m}$ in SiRN3.9, to $5.2 \mu\text{m}$ in SiRN8. Comparing this to the DW tuning obtained by adjusting waveguide height and width, it is clear that varying the silicon content is equally as effective. These results show how adjusting the silicon content could be a key enabler in generating DWs further into the MID-IR. The DW wavelengths are confirmed by solving the GNLSE. Two waveguides with a length of 2.3cm are tested. An octave spanning SC was experimentally confirmed in both a SiRN3.9 waveguide and a SiRN8 waveguide. The SiRN3.9 waveguide generated a SC from $1 \mu\text{m}$ to $2 \mu\text{m}$ in good agreement with the simulation. The SiRN8 waveguide generated SC from $1 \mu\text{m}$ to $2.5 \mu\text{m}$, but there was no sign of the predicted DW at $2.8 \mu\text{m}$. The cause of the lack of a DW in MID-IR is unknown. But a strong wavelength dependent loss in either the waveguide or the outcoupling would make it difficult to generate or measure the DW. By comparing the simulated RIN and coherence using only quantum noise, or using both quantum noise and laser noise it is shown that including the technical noise is critical for the RIN of the SC. The key take away from this chapter is that increasing the silicon content of a SiN waveguide results not only in a increased nonlinearity but can be used to heavily adjust the possible phase matching conditions of the DW in the MID-IR.

In chapter 5 a 20 cm long ANDi spiral waveguide is designed. SC is generated from 1150 nm to 1975nm using a 121fs pump laser centered at 1550 nm. The SC is found to have a RIN similar to the laser with 1-2% RIN over the full bandwidth. The RIN is largely independent on the input pulse energy. This highlights the fact that ANDi waveguides retains very low noise irrespective of waveguide length and input pulse energy. The measured SC is relatively smooth with no dips below 20dB from the maximum inside the full bandwidth. Simulations show that at 200pJ input pulse power, an octave spanning SC is expected. For comparison a 20cm anomalous dispersion waveguide is pumped with the same laser. The SC and RIN are measured at various pulse energies. It is observed that the spectrum retains low RIN until soliton fission. After soliton fission, when DWs are observed, the RIN increases as

the input power is increased. At maximum power the RIN is around 50%. An interesting phenomenon is observed, while increasing the input power increases the RIN at all wavelengths, the effect is much weaker at the DWs. Therefore, the DW can be expected to have low noise for a large range of input pulse energies. This means that for applications where only the spectrum at the DW is necessary, higher input powers can be used. This effect is also important, when attempting to determine the noise of a generated SC. It is not in general sufficient to measure the noise at the DW and then conclude, that the whole spectrum is low noise. While the ANDi SC and the anomalous dispersion SC at the soliton fission point both have low noise. The requirement for low input pulse energy limits the broadening of the anomalous dispersion SC. Nevertheless, the generated SC in the anomalous waveguide still generates wavelengths from 1-2 μm . This is an octave spanning SC generated with only 22 pJ of pulse energy in the waveguide. The experiment and simulations are repeated with shorter waveguides with a length of 2.3cm. Again it is concluded that the anomalous waveguide has low noise at soliton fission, but afterwards the RIN increases. The short waveguides do not have sufficient length for a strong broadening in the ANDi regime. The spectrum is limited to a 350 nm bandwidth from 1350nm to 1700nm. This shows that ANDi waveguides require long waveguides or higher peak power. The need for long waveguides is even more apparent when SCG using long input pulses is considered as the necessary length scales linearly with pulse width. Therefore, the fabrication of high quality spiral waveguides is needed for generating picosecond pulse SC. In general the ANDi waveguide SC retains low noise for all powers and over the full bandwidth of the SC. In contrast, the anomalous dispersion SC only has low RIN at soliton fission. Even at soliton fission simulations show an increased RIN at regions between the solitons and the DW. The ANDi SC is relatively flat, and simulations show that an improved flatness can be achieved by shaping the input pulse.

It is well known that coherent anomalous based SC is limited to pulses shorter than approximately 150 fs. A numerical investigation of long pulse pumping in an ANDi waveguide was performed. It was shown that octave spanning SC can be generated for a wide range of input pulse widths, with little effect on the resulting SC. The size of the Raman fraction is varied, and the resulting RIN for different pulses width is simulated. It is shown that the strength of the Raman effect is the key parameter limiting the usable pulse widths. For Raman effects similar to silica, a 600 fs pump can be used while retaining low noise. For weaker Raman effects, it is shown that pulses as long as 1 ps to 2 ps can be used. These results predict that flat octave spanning SC could be generated with picosecond input pulses.

In chapter 6 a directional SCG scheme is investigated. The waveguide has an ADR surrounded by two NDRs. When pumped in either of the two NDR, the spectrum broadens through the ADR to the opposite NDR. Through numerical simulations the key dynamics enabling this SCG is found. It is observed that the mechanism is the generation of a soliton in the ADR. The soliton is created when peaks of the SPM broadened pulse enters the ADR. This newly generated soliton is pushed towards the opposite ZDW by cross-phase modulation from the continuum in the NDR, and as

it approaches the second ZDW it generates DWs. Two kinds of DWs are generated. One by direct FWM from the soliton, and one as non-degenerate FWM between the soliton and the continuum in the other NDR. Interestingly, for increased input peak powers, the soliton gains higher velocity towards the opposite ZDW. Instead of recoiling at the other ZDW it passes through the ZDW into the NDR. It is believed to be the results of the high velocity causing the soliton to have insufficient time to generate a large DW. Therefore it experiences a insufficient recoil effect. This technique could be used as a method to efficiently transfer pump power into a given wavelength region of interest. One possibility would be to design either a fiber or waveguide with ZDW above the pump at 1550 nm, and then use the directionality to generate spectrum in the MID-IR.

It is impossible determine a best overall waveguide, as it depends on the specific application and the experimental parameters. In terms of waveguide materials it is clear that as the silicon content is increased, the nonlinearity and loss of the waveguide increases. Therefore, the low loss Si_3N_4 is necessary for longer waveguides, while the increased nonlinearity of SiRN is preferred for shorter waveguides, where the loss is less significant. Anomalous dispersion waveguides produce a broader spectrum for lower input pulse energies, and the bandwidth can be tuned using the dispersion engineering. From the results in both chapters 4 and 5 it is concluded that the anomalous dispersion waveguides are superior when the goal is to generate wavelengths far from the pump. But chapter 5 clearly highlight the weakness of this dispersion regime. It can only be at low noise for limited input pulse energy, waveguide length and pulse width. Even at the optimum parameters, it does not retain low noise over the whole bandwidth. Furthermore, while the anomalous waveguides are superior in terms of broadening. They are lacking when considering the flatness of the spectral and temporal shape. If the goal is low noise SC it is clear that ANDi SC is best. Furthermore, if the goal is To generate coherent SC using picosecond pulses ANDi waveguides must be used. The directional supercontinuum scheme shows potential in broadening SC towards the MID-IR. Additionally, the interaction between soliton and pump pulse could perhaps be used to generate a tunable soliton source. It promise a large amount broadening. But similar to the anomalous dispersion SC it suffers from a uneven spectrum and temporal distribution, as a results of the soliton dynamics.

Bibliography

- [1] *Mid-Infrared Coherent Sources and Applications*. Springer Netherlands, 2008. DOI: 10.1007/978-1-4020-6463-0.
- [2] Steve Buckley. “Broadband High-Brightness Sources for Spectroscopy”. In: *Spectroscopy-01-01-2019* 34 (1 Jan. 2019), pp. 16–23.
- [3] R. R. Alfano and S. L. Shapiro. “Observation of Self-Phase Modulation and Small-Scale Filaments in Crystals and Glasses”. In: *Phys. Rev. Lett.* 24 (11 Mar. 1970), pp. 592–594. DOI: 10.1103/PhysRevLett.24.592.
- [4] Jinendra K. Ranka, Robert S. Windeler, and Andrew J. Stentz. “Visible continuum generation in air–silica microstructure optical fibers with anomalous dispersion at 800 nm”. In: *Opt. Lett.* 25.1 (Jan. 2000), pp. 25–27. DOI: 10.1364/OL.25.000025.
- [5] D. Mogilevtsev, T. A. Birks, and P. St. J. Russell. “Group-velocity dispersion in photonic crystal fibers”. In: *Opt. Lett.* 23.21 (Nov. 1998), pp. 1662–1664. DOI: 10.1364/OL.23.001662.
- [6] John M Dudley, Goëry Genty, and Stéphane Coen. “Supercontinuum generation in photonic crystal fiber”. In: *Reviews of Modern Physics* 78.4 (2006), p. 1135.
- [7] Chinlon Lin and R. H. Stolen. “New nanosecond continuum for excited-state spectroscopy”. In: *Applied Physics Letters* 28.4 (1976), pp. 216–218. DOI: 10.1063/1.88702. eprint: <https://doi.org/10.1063/1.88702>.
- [8] M. Saruwatari. “Nearly penalty-free, 1t;4 ps supercontinuum Gbit/s pulse generation over 1535–1560 nm”. English. In: *Electronics Letters* 30 (10 May 1994), 790–791(1). ISSN: 0013-5194.
- [9] Brian R. Washburn, Scott A. Diddams, Nathan R. Newbury, Jeffrey W. Nicholson, Man F. Yan, and Carsten G. Jørgensen. “Phase-locked, erbium-fiber-laser-based frequency comb in the near infrared”. In: *Opt. Lett.* 29.3 (Feb. 2004), pp. 250–252. DOI: 10.1364/OL.29.000250.
- [10] L. F. Mollenauer, R. H. Stolen, and J. P. Gordon. “Experimental Observation of Picosecond Pulse Narrowing and Solitons in Optical Fibers”. In: *Phys. Rev. Lett.* 45 (13 Sept. 1980), pp. 1095–1098. DOI: 10.1103/PhysRevLett.45.1095.

- [11] Steven T. Cundiff and Jun Ye. “Colloquium: Femtosecond optical frequency combs”. In: *Rev. Mod. Phys.* 75 (1 Mar. 2003), pp. 325–342. DOI: 10.1103/RevModPhys.75.325.
- [12] A. S. Mayer, A. Klenner, A. R. Johnson, K. Luke, M. R. E. Lamont, Y. Okawachi, M. Lipson, A. L. Gaeta, and U. Keller. “Frequency comb offset detection using supercontinuum generation in silicon nitride waveguides”. In: *Opt. Express* 23.12 (June 2015), pp. 15440–15451. DOI: 10.1364/OE.23.015440.
- [13] Christopher Doerr. “Silicon photonic integration in telecommunications”. In: *Frontiers in Physics* 3 (2015), p. 37. ISSN: 2296-424X. DOI: 10.3389/fphy.2015.00037.
- [14] J. F. Bauters, M. J. R. Heck, D. John, M. Tien, A. Leinse, R. G. Heideman, D. J. Blumenthal, and J. E. Bowers. “Ultra-low loss silica-based waveguides with millimeter bend radius”. In: *36th European Conference and Exhibition on Optical Communication*. 2010, pp. 1–3. DOI: 10.1109/ECOC.2010.5621341.
- [15] José Capmany and Dalma Novak. “Microwave photonics combines two worlds”. In: *Nature Photonics* 1.6 (June 2007), pp. 319–330. ISSN: 1749-4893. DOI: 10.1038/nphoton.2007.89.
- [16] David Marpaung, Chris Roeloffzen, René Heideman, Arne Leinse, Salvador Sales, and José Capmany. “Integrated microwave photonics”. In: *Laser & Photonics Reviews* 7.4 (2013), pp. 506–538. DOI: <https://doi.org/10.1002/lpor.201200032>. eprint: <https://onlinelibrary.wiley.com/doi/pdf/10.1002/lpor.201200032>.
- [17] Glen A. Sanders, Steven J. Sanders, Lee K. Strandjord, Tiequn Qiu, Jianfeng Wu, Marc Smiciklas, Derek Mead, Sorin Mosor, Alejo Arrizon, Waymon Ho, and Mary Salit. “Fiber optic gyro development at Honeywell”. In: *Fiber Optic Sensors and Applications XIII*. Ed. by Eric Udd, Gary Pickrell, and Henry H. Du. Vol. 9852. International Society for Optics and Photonics. SPIE, 2016, pp. 37–50. DOI: 10.1117/12.2228893.
- [18] Andrew D. Ludlow, Martin M. Boyd, Jun Ye, E. Peik, and P. O. Schmidt. “Optical atomic clocks”. In: *Rev. Mod. Phys.* 87 (2 June 2015), pp. 637–701. DOI: 10.1103/RevModPhys.87.637.
- [19] Katrien De Vos, Irene Bartolozzi, Etienne Schacht, Peter Bienstman, and Roel Baets. “Silicon-on-Insulator microring resonator for sensitive and label-free biosensing”. In: *Opt. Express* 15.12 (June 2007), pp. 7610–7615. DOI: 10.1364/OE.15.007610.
- [20] Martijn Boerkamp, Thijs van Leest, Jeroen Heldens, Arne Leinse, Marcel Hoekman, Rene Heideman, and Jacob Caro. “On-chip optical trapping and Raman spectroscopy using a TripleX dual-waveguide trap”. In: *Opt. Express* 22.25 (Dec. 2014), pp. 30528–30537. DOI: 10.1364/OE.22.030528.

- [21] Ian Coddington, Nathan Newbury, and William Swann. “Dual-comb spectroscopy”. In: *Optica* 3.4 (Apr. 2016), pp. 414–426. DOI: 10.1364/OPTICA.3.000414.
- [22] Myoung-Gyun Suh, Qi-Fan Yang, Ki Youl Yang, Xu Yi, and Kerry J. Vahala. “Microresonator soliton dual-comb spectroscopy”. In: *Science* 354.6312 (2016), pp. 600–603. ISSN: 0036-8075. DOI: 10.1126/science.aah6516. eprint: <https://science.sciencemag.org/content/354/6312/600.full.pdf>.
- [23] Alexander L. Gaeta, Michal Lipson, and Tobias J. Kippenberg. “Photonic-chip-based frequency combs”. In: *Nature Photonics* 13.3 (Mar. 2019), pp. 158–169. ISSN: 1749-4893. DOI: 10.1038/s41566-019-0358-x.
- [24] Xin Gai, Yi Yu, Bart Kuyken, Pan Ma, Steve Madden, Joris Van Campenhout, Peter Verheyen, Gunther Roelkens, Roel Baets, and Barry Luther-Davies. “Nonlinear absorption and refraction in crystalline silicon in the mid-infrared”. In: *Laser Photonics Reviews* 7 (Nov. 2013). DOI: 10.1002/lpor.201300103.
- [25] Ryan K. W. Lau, Michael R. E. Lamont, Austin G. Griffith, Yoshitomo Okawachi, Michal Lipson, and Alexander L. Gaeta. “Octave-spanning mid-infrared supercontinuum generation in silicon nanowaveguides”. In: *Opt. Lett.* 39.15 (Aug. 2014), pp. 4518–4521. DOI: 10.1364/OL.39.004518.
- [26] Neetesh Singh, Darren D. Hudson, Yi Yu, Christian Grillet, Stuart D. Jackson, Alvaro Casas-Bedoya, Andrew Read, Petar Atanackovic, Steven G. Duvall, Stefano Palomba, Barry Luther-Davies, Stephen Madden, David J. Moss, and Benjamin J. Eggleton. “Midinfrared supercontinuum generation from 2 to 6 μm in a silicon nanowire”. In: *Optica* 2.9 (Sept. 2015), pp. 797–802. DOI: 10.1364/OPTICA.2.000797.
- [27] R. Halir, Y. Okawachi, J. S. Levy, M. A. Foster, M. Lipson, and A. L. Gaeta. “Ultrabroadband supercontinuum generation in a CMOS-compatible platform”. In: *Opt. Lett.* 37.10 (May 2012), pp. 1685–1687. DOI: 10.1364/OL.37.001685.
- [28] Jörn P. Epping, Tim Hellwig, Marcel Hoekman, Richard Mateman, Arne Leinse, René G. Heideman, Albert van Rees, Peter J.M. van der Slot, Chris J. Lee, Carsten Fallnich, and Klaus-J. Boller. “On-chip visible-to-infrared supercontinuum generation with more than 495 THz spectral bandwidth”. In: *Opt. Express* 23.15 (July 2015), pp. 19596–19604. DOI: 10.1364/OE.23.019596.
- [29] Marco A. G. Porcel, Florian Schepers, Jörn P. Epping, Tim Hellwig, Marcel Hoekman, René G. Heideman, Peter J. M. van der Slot, Chris J. Lee, Robert Schmidt, Rudolf Bratschitsch, Carsten Fallnich, and Klaus-J. Boller. “Two-octave spanning supercontinuum generation in stoichiometric silicon nitride waveguides pumped at telecom wavelengths”. In: *Opt. Express* 25.2 (Jan. 2017), pp. 1542–1554. DOI: 10.1364/OE.25.001542.

- [30] Haolan Zhao, Bart Kuyken, Stéphane Clemmen, François Leo, Ananth Subramanian, Ashim Dhakal, Philippe Helin, Simone Severi, Edouard Brainis, Gunther Roelkens, and Roel Baets. “Visible-to-near-infrared octave spanning supercontinuum generation in a silicon nitride waveguide”. In: *Opt. Lett.* 40.10 (May 2015), pp. 2177–2180. DOI: 10.1364/OL.40.002177.
- [31] Hairun Guo, Clemens Herkommer, Adrien Billat, Davide Grassani, Chuankun Zhang, Martin H. P. Pfeiffer, Wenle Weng, Camille-Sophie Brès, and Tobias J. Kippenberg. “Mid-infrared frequency comb via coherent dispersive wave generation in silicon nitride nanophotonic waveguides”. In: *Nature Photonics* 12.6 (June 2018), pp. 330–335. ISSN: 1749-4893. DOI: 10.1038/s41566-018-0144-1.
- [32] Clemens J. Krüchel, Attila Fülöp, Thomas Klintberg, Jörgen Bengtsson, Peter A. Andrekson, and Víctor Torres-Company. “Linear and nonlinear characterization of low-stress high-confinement silicon-rich nitride waveguides”. In: *Optics Express* 23.20 (Oct. 2015), pp. 25827–25837. DOI: 10.1364/OE.23.025827.
- [33] Xing Liu, Minhao Pu, Binbin Zhou, Clemens J. Krüchel, Attila Fülöp, Victor Torres-Company, and Morten Bache. “Octave-spanning supercontinuum generation in a silicon-rich nitride waveguide”. In: *Optics Letters* 41.12 (2016), pp. 2719–2722. DOI: 10.1364/OL.41.002719.
- [34] Zhichao Ye, Krishna Twayana, Peter A. Andrekson, and Victor Torres-Company. “High-Q Dispersion-Engineered Si₃N₄ Microresonators Based on a Subtractive Processing Technique”. In: *Conference on Lasers and Electro-Optics*. Optical Society of America, 2020, JTh2F.24. DOI: 10.1364/CLEO_AT.2020.JTh2F.24.
- [35] John M. Dudley and Stéphane Coen. “Coherence properties of supercontinuum spectra generated in photonic crystal and tapered optical fibers”. In: *Opt. Lett.* 27.13 (July 2002), pp. 1180–1182. DOI: 10.1364/OL.27.001180.
- [36] Simon Christensen, Shreesha Rao D. S., Ole Bang, and Morten Bache. “Directional supercontinuum generation: the role of the soliton”. In: *J. Opt. Soc. Am. B* 36.2 (Feb. 2019), A131–A138. DOI: 10.1364/JOSAB.36.00A131.
- [37] Simon Christensen, Zhichao Ye, Morten Bache, and Victor Torres Company. “Octave-spanning frequency comb generation in all-normal-dispersion silicon-rich silicon nitride waveguide”. In: *Conference on Lasers and Electro-Optics*. Optical Society of America, 2020, STu3H.7. DOI: 10.1364/CLEO_SI.2020.STu3H.7.
- [38] Simon Christensen and Morten Bache. “Directional supercontinuum generation”. In: *Advanced Photonics 2018 (BGPP, IPR, NP, NOMA, Sensors, Networks, SPPCom, SOF)*. Optical Society of America, 2018, NpTh4C.5. DOI: 10.1364/NP.2018.NpTh4C.5.
- [39] K. J. Blow and D. Wood. “Theoretical description of transient stimulated Raman scattering in optical fibers”. In: *IEEE Journal of Quantum Electronics* 25.12 (1989), pp. 2665–2673. DOI: 10.1109/3.40655.

- [40] Thomas Brabec and Ferenc Krausz. “Nonlinear Optical Pulse Propagation in the Single-Cycle Regime”. In: *Phys. Rev. Lett.* 78 (17 Apr. 1997), pp. 3282–3285. DOI: 10.1103/PhysRevLett.78.3282.
- [41] P. Kinsler, S. B. P. Radnor, and G. H. C. New. “Theory of directional pulse propagation”. In: *Phys. Rev. A* 72 (6 Dec. 2005), p. 063807. DOI: 10.1103/PhysRevA.72.063807.
- [42] P. Kinsler. “Limits of the unidirectional pulse propagation approximation”. In: *J. Opt. Soc. Am. B* 24.9 (Sept. 2007), pp. 2363–2368. DOI: 10.1364/JOSAB.24.002363.
- [43] Shahraam Afshar V. and Tanya M. Monro. “A full vectorial model for pulse propagation in emerging waveguides with subwavelength structures part I: Kerr nonlinearity”. In: *Opt. Express* 17.4 (Feb. 2009), pp. 2298–2318. DOI: 10.1364/OE.17.002298.
- [44] Francesco Poletti and Peter Horak. “Description of ultrashort pulse propagation in multimode optical fibers”. In: *J. Opt. Soc. Am. B* 25.10 (Oct. 2008), pp. 1645–1654. DOI: 10.1364/JOSAB.25.001645.
- [45] P. V. Mamyshev and S. V. Chernikov. “Ultrashort-pulse propagation in optical fibers”. In: *Opt. Lett.* 15.19 (Oct. 1990), pp. 1076–1078. DOI: 10.1364/OL.15.001076.
- [46] Jesper Laegsgaard. “Mode profile dispersion in the generalized nonlinear Schrödinger equation”. In: *Optics Express* 15.24 (2007), pp. 16110–16123.
- [47] John M Dudley and James Roy Taylor. *Supercontinuum generation in optical fibers*. Cambridge University Press, 2010.
- [48] Govind P Agrawal. *Nonlinear Fiber Optics*. 5th ed. Academic Press, 2012.
- [49] Maxim Karpov, Hairun Guo, Arne Kordts, Victor Brasch, Martin H. P. Pfeiffer, Michail Zervas, Michael Geiselmann, and Tobias J. Kippenberg. “Raman Self-Frequency Shift of Dissipative Kerr Solitons in an Optical Microresonator”. In: *Phys. Rev. Lett.* 116 (10 Mar. 2016), p. 103902. DOI: 10.1103/PhysRevLett.116.103902.
- [50] Alexander Klenner, Aline S. Mayer, Adrea R. Johnson, Kevin Luke, Michael R. E. Lamont, Yoshitomo Okawachi, Michal Lipson, Alexander L. Gaeta, and Ursula Keller. “Gigahertz frequency comb offset stabilization based on supercontinuum generation in silicon nitride waveguides”. In: *Opt. Express* 24.10 (May 2016), pp. 11043–11053. DOI: 10.1364/OE.24.011043.
- [51] Alexander M. Heidt, James S. Feehan, Jonathan H. V. Price, and Thomas Feurer. “Limits of coherent supercontinuum generation in normal dispersion fibers”. In: *J. Opt. Soc. Am. B* 34.4 (Apr. 2017), pp. 764–775. DOI: 10.1364/JOSAB.34.000764.

- [52] Stéphane Pitois and Guy Millot. “Experimental observation of a new modulational instability spectral window induced by fourth-order dispersion in a normally dispersive single-mode optical fiber”. In: *Optics Communications* 226.1 (2003), pp. 415–422. ISSN: 0030-4018. DOI: <https://doi.org/10.1016/j.optcom.2003.09.001>.
- [53] D. Anderson, M. Desaix, M. Lisak, and M. L. Quiroga–Teixeiro. “Wave breaking in nonlinear-optical fibers”. In: *J. Opt. Soc. Am. B* 9.8 (Aug. 1992), pp. 1358–1361. DOI: 10.1364/JOSAB.9.001358.
- [54] Christophe Finot, Bertrand Kibler, Lionel Provost, and Stefan Wabnitz. “Beneficial impact of wave-breaking for coherent continuum formation in normally dispersive nonlinear fibers”. In: *J. Opt. Soc. Am. B* 25.11 (Nov. 2008), pp. 1938–1948. DOI: 10.1364/JOSAB.25.001938.
- [55] Bart Kuyken, Takuro Ideguchi, Simon Holzner, Ming Yan, Theodor W. Hänsch, Joris Van Campenhout, Peter Verheyen, Stéphane Coen, Francois Leo, Roel Baets, Gunther Roelkens, and Nathalie Picqué. “An octave-spanning mid-infrared frequency comb generated in a silicon nanophotonic wire waveguide”. In: *Nature Communications* 6.1 (Feb. 2015), p. 6310. ISSN: 2041-1723. DOI: 10.1038/ncomms7310.
- [56] Jeff Chiles et al. “Multifunctional integrated photonics in the mid-infrared with suspended AlGaAs on silicon”. In: *Optica* 6.9 (Sept. 2019), pp. 1246–1254. DOI: 10.1364/OPTICA.6.001246.
- [57] Bart Kuyken, Maximilien Billet, Francois Leo, Kresten Yvind, and Minhao Pu. “Octave-spanning coherent supercontinuum generation in an AlGaAs-on-insulator waveguide”. In: *Opt. Lett.* 45.3 (Feb. 2020), pp. 603–606. DOI: 10.1364/OL.45.000603.
- [58] Michael R.E. Lamont, Barry Luther-Davies, Duk-Yong Choi, Steve Madden, and Benjamin J. Eggleton. “Supercontinuum generation in dispersion engineered highly nonlinear ($\gamma = 10$ /W/m) As₂S₃ chalcogenide planar waveguide”. In: *Opt. Express* 16.19 (Sept. 2008), pp. 14938–14944. DOI: 10.1364/OE.16.014938.
- [59] M. D. Pelusi, F. Luan, T. D. Vo, M. R. E. Lamont, S. J. Madden, D.-Y. Choi, D. A. P. Bulla, B. Luther-Davies, and B. J. Eggleton. “Ultra-Broadband (THz) RF Spectrum Monitoring of High-Speed Optical Signals using a Chalcogenide Waveguide Chip”. In: *Optical Fiber Communication Conference and National Fiber Optic Engineers Conference*. Optical Society of America, 2009, OThH6. DOI: 10.1364/OFC.2009.0ThH6.
- [60] Mohammad R. Karim, B. M. A. Rahman, and Govind P. Agrawal. “A broadband mid-infrared supercontinuum generation using Ge_{11.5}As₂₄Se_{64.5} channel waveguide”. In: *Advanced Photonics 2015*. Optical Society of America, 2015, JM3A.15.

- [61] B. B. Zhou, A. Chong, F. W. Wise, and M. Bache. “Ultrafast and Octave-Spanning Optical Nonlinearities from Strongly Phase-Mismatched Quadratic Interactions”. In: *Phys. Rev. Lett.* 109 (4 July 2012), p. 043902. DOI: 10.1103/PhysRevLett.109.043902.
- [62] Binbin Zhou, Hairun Guo, and Morten Bache. “Energetic mid-IR femtosecond pulse generation by self-defocusing soliton-induced dispersive waves in a bulk quadratic nonlinear crystal”. In: *Opt. Express* 23.5 (Mar. 2015), pp. 6924–6936. DOI: 10.1364/OE.23.006924.
- [63] B. B. Zhou, X. Liu, H. R. Guo, X. L. Zeng, X. F. Chen, H. P. Chung, Y. H. Chen, and M. Bache. “Parametrically Tunable Soliton-Induced Resonant Radiation by Three-Wave Mixing”. In: *Phys. Rev. Lett.* 118 (14 Apr. 2017), p. 143901. DOI: 10.1103/PhysRevLett.118.143901.
- [64] Hairun Guo, Xianglong Zeng, Binbin Zhou, and Morten Bache. “Few-cycle solitons and supercontinuum generation with cascaded quadratic nonlinearities in unpoled lithium niobate ridge waveguides”. In: *Opt. Lett.* 39.5 (Mar. 2014), pp. 1105–1108. DOI: 10.1364/OL.39.001105.
- [65] Hairun Guo, Binbin Zhou, Xianglong Zeng, and Morten Bache. “Highly coherent mid-IR supercontinuum by self-defocusing solitons in lithium niobate waveguides with all-normal dispersion”. In: *Opt. Express* 22.10 (May 2014), pp. 12211–12225. DOI: 10.1364/OE.22.012211.
- [66] Mian Zhang, Cheng Wang, Rebecca Cheng, Amirhassan Shams-Ansari, and Marko Lončar. “Monolithic ultra-high-Q lithium niobate microring resonator”. In: *Optica* 4.12 (Dec. 2017), pp. 1536–1537. DOI: 10.1364/OPTICA.4.001536.
- [67] Abijith S. Kowligy, Alex Lind, Daniel D. Hickstein, David R. Carlson, Henry Timmers, Nima Nader, Flavio C. Cruz, Gabriel Ycas, Scott B. Papp, and Scott A. Diddams. “Mid-infrared frequency comb generation via cascaded quadratic nonlinearities in quasi-phase-matched waveguides”. In: *Opt. Lett.* 43.8 (Apr. 2018), pp. 1678–1681. DOI: 10.1364/OL.43.001678.
- [68] C. R. Phillips, Carsten Langrock, J. S. Pelc, M. M. Fejer, J. Jiang, Martin E. Fermann, and I. Hartl. “Supercontinuum generation in quasi-phase-matched LiNbO₃ waveguide pumped by a Tm-doped fiber laser system”. In: *Opt. Lett.* 36.19 (Oct. 2011), pp. 3912–3914. DOI: 10.1364/OL.36.003912.
- [69] Mengjie Yu, Boris Desiatov, Yoshitomo Okawachi, Alexander L. Gaeta, and Marko Lončar. “Coherent two-octave-spanning supercontinuum generation in lithium-niobate waveguides”. In: *Opt. Lett.* 44.5 (Mar. 2019), pp. 1222–1225. DOI: 10.1364/OL.44.001222.
- [70] Yoshitomo Okawachi, Mengjie Yu, Boris Desiatov, Bok Young Kim, Tobias Hansson, Marko Lončar, and Alexander L. Gaeta. “Chip-based self-referencing using integrated lithium niobate waveguides”. In: *Optica* 7.6 (June 2020), pp. 702–707. DOI: 10.1364/OPTICA.392363.

- [71] P. Temple-Boyer, C. Rossi, E. Saint-Etienne, and E. Scheid. “Residual stress in low pressure chemical vapor deposition SiNx films deposited from silane and ammonia”. In: *Journal of Vacuum Science & Technology A* 16.4 (1998), pp. 2003–2007. DOI: 10.1116/1.581302. eprint: <https://doi.org/10.1116/1.581302>.
- [72] Alexander Gondarenko, Jacob S. Levy, and Michal Lipson. “High confinement micron-scale silicon nitride high Q ring resonator”. In: *Opt. Express* 17.14 (July 2009), pp. 11366–11370. DOI: 10.1364/OE.17.011366.
- [73] Martin H. P. Pfeiffer, Arne Kordts, Victor Brasch, Michael Zervas, Michael Geiselmann, John D. Jost, and Tobias J. Kippenberg. “Photonic Damascene process for integrated high-Q microresonator based nonlinear photonics”. In: *Optica* 3.1 (Jan. 2016), pp. 20–25. DOI: 10.1364/OPTICA.3.000020.
- [74] Kevin Luke, Avik Dutt, Carl B. Poitras, and Michal Lipson. “Overcoming Si₃N₄ film stress limitations for high quality factor ring resonators”. In: *Opt. Express* 21.19 (Sept. 2013), pp. 22829–22833. DOI: 10.1364/OE.21.022829.
- [75] David J. Moss, Roberto Morandotti, Alexander L. Gaeta, and Michal Lipson. “New CMOS-compatible platforms based on silicon nitride and Hydex for nonlinear optics”. In: *Nature Photonics* 7.8 (Aug. 2013), pp. 597–607. ISSN: 1749-4893. DOI: 10.1038/nphoton.2013.183.
- [76] Jacob S. Levy, Alexander Gondarenko, Mark A. Foster, Amy C. Turner-Foster, Alexander L. Gaeta, and Michal Lipson. “CMOS-compatible multiple-wavelength oscillator for on-chip optical interconnects”. In: *Nature Photonics* 4.1 (Jan. 2010), pp. 37–40. ISSN: 1749-4893. DOI: 10.1038/nphoton.2009.259.
- [77] Kazuhiro Ikeda, Robert E. Saperstein, Nikola Alic, and Yeshiahu Fainman. “Thermal and Kerr nonlinear properties of plasma-deposited silicon nitride/silicon dioxide waveguides”. In: *Opt. Express* 16.17 (Aug. 2008), pp. 12987–12994. DOI: 10.1364/OE.16.012987.
- [78] J.P. Epping, T. Hellwig, M. Hoekman, R. Mateman, A. Leinse, R.G. Heideman, A. van Rees, P.J.M. van der Slot, C.J. Lee, C. Fallnich, and K.-J. Boller. “Simultaneous Supercontinuum and Third Harmonic Generation in Si₃N₄ waveguides”. In: *2015 European Conference on Lasers and Electro-Optics - European Quantum Electronics Conference*. Optical Society of America, 2015, CK₅₄.
- [79] Dmitry Martyshkin, Vladimir Fedorov, Taylor Kesterson, Sergey Vasilyev, Hairun Guo, Junqiu Liu, Wenle Weng, Konstantin Vodopyanov, Tobias J. Kippenberg, and Sergey Mirov. “Visible-near-middle infrared spanning supercontinuum generation in a silicon nitride (Si₃N₄) waveguide”. In: *Opt. Mater. Express* 9.6 (June 2019), pp. 2553–2559. DOI: 10.1364/OME.9.002553.
- [80] Hairun Guo, Wenle Weng, Junqiu Liu, Fan Yang, Wolfgang Hänsel, Camille Sophie Brès, Luc Thévenaz, Ronald Holzwarth, and Tobias J. Kippenberg. “Nanophotonic supercontinuum-based mid-infrared dual-comb spectroscopy”. In: *Optica* 7.9 (Sept. 2020), pp. 1181–1188. DOI: 10.1364/OPTICA.396542.

- [81] Davide Grassani, Eirini Tagkoudi, Hairun Guo, Clemens Herkommer, Fan Yang, Tobias J. Kippenberg, and Camille-Sophie Brès. “Mid infrared gas spectroscopy using efficient fiber laser driven photonic chip-based supercontinuum”. In: *Nature Communications* 10.1 (Apr. 2019), p. 1553. ISSN: 2041-1723. DOI: 10.1038/s41467-019-09590-3.
- [82] Clemens J. Krüchel, Attila Fülöp, Zhichao Ye, Peter A. Andrekson, and Victor Torres-Company. “Optical bandgap engineering in nonlinear silicon nitride waveguides”. In: *Optics Express* 25.13 (June 2017), pp. 15370–15380. DOI: 10.1364/OE.25.015370.
- [83] K. J. A. Ooi, D. K. T. Ng, T. Wang, A. K. L. Chee, S. K. Ng, Q. Wang, L. K. Ang, A. M. Agarwal, L. C. Kimerling, and D. T. H. Tan. “Pushing the limits of CMOS optical parametric amplifiers with USRN:Si7N3 above the two-photon absorption edge”. In: *Nature Communications* 8.1 (Jan. 2017), p. 13878. ISSN: 2041-1723. DOI: 10.1038/ncomms13878.
- [84] Zhichao Ye, Attila Fülöp, Óskar Bjarki Helgason, Peter A. Andrekson, and Victor Torres-Company. “Low-loss high-Q silicon-rich silicon nitride microresonators for Kerr nonlinear optics”. In: *Opt. Lett.* 44.13 (July 2019), pp. 3326–3329. DOI: 10.1364/OL.44.003326.
- [85] Stéphane Coen, Alvin Hing Lun Chau, Rainer Leonhardt, John D. Harvey, Jonathan C. Knight, William J. Wadsworth, and Philip St. J. Russell. “White-light supercontinuum generation with 60-ps pump pulses in a photonic crystal fiber”. In: *Opt. Lett.* 26.17 (Sept. 2001), pp. 1356–1358. DOI: 10.1364/OL.26.001356.
- [86] Robert R. Alfano, ed. *The Supercontinuum Laser Source*. Springer-Verlag, 2006. DOI: 10.1007/b106776.
- [87] Jun Takayanagi and Norihiko Nishizawa. “Generation of Widely and Flatly Broadened, Low-Noise and High-Coherence Supercontinuum in All-Fiber System”. In: *Japanese Journal of Applied Physics* 45.No. 16 (Apr. 2006), pp. L441–L443. DOI: 10.1143/jjap.45.1441.
- [88] Norihiko Nishizawa and Jun Takayanagi. “Octave spanning high-quality supercontinuum generation in all-fiber system”. In: *J. Opt. Soc. Am. B* 24.8 (Aug. 2007), pp. 1786–1792. DOI: 10.1364/JOSAB.24.001786.
- [89] Alexander M Heidt. “Pulse preserving flat-top supercontinuum generation in all-normal dispersion photonic crystal fibers”. In: *Journal of the Optical Society of America B* 27.3 (2010), pp. 550–559.
- [90] Shreesha Rao D. S., Rasmus D. Engelsholm, Iván B. Gonzalo, Binbin Zhou, Patrick Bowen, Peter M. Moselund, Ole Bang, and Morten Bache. “Ultra-low-noise supercontinuum generation with a flat near-zero normal dispersion fiber”. In: *Opt. Lett.* 44.9 (May 2019), pp. 2216–2219. DOI: 10.1364/OL.44.002216.

- [91] Iván Bravo Gonzalo, Rasmus Dybbro Engelsholm, Mads Peter Sørensen, and Ole Bang. “Polarization noise places severe constraints on coherence of all-normal dispersion femtosecond supercontinuum generation”. In: *Scientific Reports* 8.1 (Apr. 2018), p. 6579. ISSN: 2045-2322. DOI: 10.1038/s41598-018-24691-7.
- [92] Alexander Hartung, Alexander M. Heidt, and Hartmut Bartelt. “Nanoscale all-normal dispersion optical fibers for coherent supercontinuum generation at ultraviolet wavelengths”. In: *Opt. Express* 20.13 (June 2012), pp. 13777–13788. DOI: 10.1364/OE.20.013777.
- [93] Nan Zhang, Xuefeng Peng, Yingying Wang, Shixun Dai, Yuan Yuan, Jingxiang Su, Guangtao Li, Peiqing Zhang, Peilong Yang, and Xunsi Wang. “Ultra-broadband and coherent mid-infrared supercontinuum generation in Te-based chalcogenide tapered fiber with all-normal dispersion”. In: *Opt. Express* 27.7 (Apr. 2019), pp. 10311–10319. DOI: 10.1364/OE.27.010311.
- [94] Jintao Lai, Jinhui Yuan, Yujun Cheng, Chao Mei, Xian Zhou, Qiang Wu, Binbin Yan, Kuiru Wang, Keping Long, Chongxiu Yu, and Xinzhu Sang. “Dispersion-engineered T-type germanium waveguide for mid-infrared supercontinuum and frequency comb generations in all-normal dispersion region”. In: *OSA Continuum* 3.9 (Sept. 2020), pp. 2320–2331. DOI: 10.1364/OSAC.399941.
- [95] M. R. Karim, H. Ahmad, S. Ghosh, and B. M. A. Rahman. “Design of dispersion-engineered As₂Se₃ channel waveguide for mid-infrared region supercontinuum generation”. In: *Journal of Applied Physics* 123.21 (2018), p. 213101. DOI: 10.1063/1.5033494. eprint: <https://doi.org/10.1063/1.5033494>.
- [96] Yi Yu, Xin Gai, Pan Ma, Khu Vu, Zhiyong Yang, Rongping Wang, Duk-Yong Choi, Steve Madden, and Barry Luther-Davies. “Experimental demonstration of linearly polarized 2-μm supercontinuum generation in a chalcogenide rib waveguide”. In: *Opt. Lett.* 41.5 (Mar. 2016), pp. 958–961. DOI: 10.1364/OL.41.000958.
- [97] Milan Sinobad, Alberto DellaTorre, Remi Armand, Barry Luther-Davies, Pan Ma, Stephen Madden, Arnan Mitchell, David J. Moss, Jean-Michel Hartmann, Jean-Marc Fedeli, Christelle Monat, and Christian Grillet. “Mid-infrared supercontinuum generation in silicon-germanium all-normal dispersion waveguides”. In: *Opt. Lett.* 45.18 (Sept. 2020), pp. 5008–5011. DOI: 10.1364/OL.402159.
- [98] Junxiong Wei, Charles Ciret, Maximilien Billet, François Leo, Bart Kuyken, and Simon-Pierre Gorza. “Supercontinuum Generation Assisted by Wave Trapping in Dispersion-Managed Integrated Silicon Waveguides”. In: *Phys. Rev. Applied* 14 (5 Nov. 2020), p. 054045. DOI: 10.1103/PhysRevApplied.14.054045.
- [99] Neetesh Singh, Diedrik Vermulen, Alfonso Ruocco, Nanxi Li, Erich Ippen, Franz X. Kärtner, and Michael R. Watts. “Supercontinuum generation in varying dispersion and birefringent silicon waveguide”. In: *Opt. Express* 27.22 (Oct. 2019), pp. 31698–31712. DOI: 10.1364/OE.27.031698.

- [100] Scott R. Domingue and Randy A. Bartels. “Overcoming temporal polarization instabilities from the latent birefringence in all-normal dispersion, wave-breaking-extended nonlinear fiber supercontinuum generation”. In: *Opt. Express* 21.11 (June 2013), pp. 13305–13321. DOI: 10.1364/OE.21.013305.
- [101] Stefan Wabnitz. “Modulational polarization instability of light in a nonlinear birefringent dispersive medium”. In: *Phys. Rev. A* 38 (4 Aug. 1988), pp. 2018–2021. DOI: 10.1103/PhysRevA.38.2018.
- [102] Igor A. Sukhoivanov, Sergii O. Iakushev, Oleksiy V. Shulika, Jose Amparao Andrade-Lucio, Antonio Díez, and Miguel Andrés. “Supercontinuum generation at 800 nm in all-normal dispersion photonic crystal fiber”. In: *Opt. Express* 22.24 (Dec. 2014), pp. 30234–30250. DOI: 10.1364/OE.22.030234.
- [103] Yuxi Fang, Changjing Bao, Zhi Wang, Bo Liu, Xu Han, Yuxuan He, Hao Huang, Yongxiong Ren, Zhongqi Pan, and Yang Yue. “Flat and Coherent Supercontinuum Generation in Si₃N₄ Slot Waveguide with All-normal Dispersion”. In: *Asia Communications and Photonics Conference (ACPC) 2019*. Optical Society of America, 2019, M4A.251.
- [104] J. M. Chavez Boggio, D. Bodenmüller, T. Fremberg, R. Haynes, M. M. Roth, R. Eisermann, M. Lisker, L. Zimmermann, and M. Böhm. “Dispersion engineered silicon nitride waveguides by geometrical and refractive-index optimization”. In: *J. Opt. Soc. Am. B* 31.11 (Nov. 2014), pp. 2846–2857. DOI: 10.1364/JOSAB.31.002846.
- [105] P. Hlubina, M. Kadulová, and D. Ciprian. “Spectral interferometry-based chromatic dispersion measurement of fibre including the zero-dispersion wavelength”. In: *Journal of the European Optical Society - Rapid publications* 7.0 (2012). ISSN: 1990-2573.
- [106] Maxim Karpov, Hairun Guo, Arne Kordts, Victor Brasch, Martin H. P. Pfeifer, Michail Zervas, Michael Geiselmann, and Tobias J. Kippenberg. “Raman Self-Frequency Shift of Dissipative Kerr Solitons in an Optical Microresonator: Supplemental Material”. In: *Physical Review Letters* 116 (10 Mar. 2016), p. 103902. DOI: 10.1103/PhysRevLett.116.103902.
- [107] Iván Bravo Gonzalo, Rasmus Dybbro Engelsholm, Mads Peter Sørensen, and Ole Bang. “Polarization noise places severe constraints on coherence of all-normal dispersion femtosecond supercontinuum generation”. In: *Scientific Reports* 8 (2018), p. 6579.
- [108] Christophe Finot, Bertrand Kibler, Lionel Provost, and Stefan Wabnitz. “Beneficial impact of wave-breaking for coherent continuum formation in normally dispersive nonlinear fibers”. In: *Journal of the Optical Society of America B* 25.11 (2008), pp. 1938–1948.
- [109] Nail Akhmediev and Magnus Karlsson. “Cherenkov radiation emitted by solitons in optical fibers”. In: *Physical Review A* 51.3 (1995), p. 2602.

- [110] T Schreiber, TV Andersen, D Schimpf, J Limpert, and A Tünnermann. “Supercontinuum generation by femtosecond single and dual wavelength pumping in photonic crystal fibers with two zero dispersion wavelengths”. In: *Optics Express* 13.23 (2005), pp. 9556–9569.
- [111] G Genty, M Lehtonen, H Ludvigsen, and M Kaivola. “Enhanced bandwidth of supercontinuum generated in microstructured fibers”. In: *Optics Express* 12.15 (2004), pp. 3471–3480.
- [112] Christian Rosenberg Petersen, Rasmus D Engelholm, Christos Markos, Laurent Brilland, Céline Caillaud, Johann Trolès, and Ole Bang. “Increased mid-infrared supercontinuum bandwidth and average power by tapering large-mode-area chalcogenide photonic crystal fibers”. In: *Optics Express* 25.13 (2017), pp. 15336–15348.
- [113] Kebin Shi, Peng Li, Shizhuo Yin, and Zhiwen Liu. “Chromatic confocal microscopy using supercontinuum light”. In: *Optics Express* 12.10 (2004), pp. 2096–2101.
- [114] D.V. Skryabin and Y.V. Kartashov. “Self-locking of the frequency comb repetition rate in microring resonators with higher order dispersions”. In: *Optics Express* 25.22 (Oct. 2017), pp. 27442–27451. DOI: 10.1364/OE.25.027442.
- [115] P. Trocha, M. Karpov, D. Ganin, M. H. P. Pfeiffer, A. Kordts, S. Wolf, J. Krockenberger, P. Marin-Palomo, C. Weimann, S. Randel, W. Freude, T. J. Kippenberg, and C. Koos. “Ultrafast optical ranging using microresonator soliton frequency combs”. In: *Science* 359.6378 (2018), pp. 887–891. ISSN: 0036-8075. DOI: 10.1126/science.aao3924. eprint: <http://science.sciencemag.org/content/359/6378/887.full.pdf>.
- [116] Avik Dutt, Chaitanya Joshi, Xingchen Ji, Jaime Cardenas, Yoshitomo Okawachi, Kevin Luke, Alexander L. Gaeta, and Michal Lipson. “On-chip dual-comb source for spectroscopy”. In: *Science Advances* 4.3 (2018). DOI: 10.1126/sciadv.1701858. eprint: <http://advances.sciencemag.org/content/4/3/e1701858.full.pdf>.
- [117] Dieter Schadt and Bozena Jaskorzynska. “Suppression of the Raman self-frequency shift by cross-phase modulation”. In: *Journal of the Optical Society of America B* 5.11 (1988), pp. 2374–2378.
- [118] G Genty, M Lehtonen, and H Ludvigsen. “Route to broadband blue-light generation in microstructured fibers”. In: *Optics Letters* 30.7 (2005), pp. 756–758.
- [119] G Genty, M Lehtonen, and H Ludvigsen. “Effect of cross-phase modulation on supercontinuum generated in microstructured fibers with sub-30 fs pulses”. In: *Optics Express* 12.19 (2004), pp. 4614–4624.
- [120] Ayhan Demircan, Shalva Amiranashvili, Carsten Brée, Uwe Morgner, and Günter Steinmeyer. “Supercontinuum generation by multiple scatterings at a group velocity horizon”. In: *Optics Express* 22.4 (2014), pp. 3866–3879.

- [121] Xing Liu, Binbin Zhou, Hairun Guo, and Morten Bache. “Mid- IR femtosecond frequency conversion by soliton-probe collision in phase-mismatched quadratic nonlinear crystals”. In: *Optics Letters* 40.16 (2015), pp. 3798–3801.
- [122] A. Efimov, A. V. Yulin, D. V. Skryabin, J. C. Knight, N. Joly, F. G. Omenetto, A. J. Taylor, and P. Russell. “Interaction of an Optical Soliton with a Dispersive Wave”. In: *Physical Review Letters* 95 (21 Nov. 2005), p. 213902. DOI: 10.1103/PhysRevLett.95.213902.
- [123] Ayhan Demircan, Shalva Amiranashvili, Carsten Brée, and Günter Steinmeyer. “Compressible octave spanning supercontinuum generation by two-pulse collisions”. In: *Physical Review Letters* 110.23 (2013), p. 233901.
- [124] Samudra Roy, Shyamal K. Bhadra, Kunimasa Saitoh, Masanori Koshiba, and Govind P. Agrawal. “Dynamics of Raman soliton during supercontinuum generation near the zero-dispersion wavelength of optical fibers”. In: *Opt. Express* 19.11 (May 2011), pp. 10443–10455. DOI: 10.1364/OE.19.010443.
- [125] Karen E Webb, Miro Erkintalo, Yiqing Xu, Neil GR Broderick, John M Dudley, Goëry Genty, and Stuart G Murdoch. “Nonlinear optics of fibre event horizons”. In: *Nature Communications* 5 (2014), p. 4969.
- [126] Thomas G Philbin, Chris Kuklewicz, Scott Robertson, Stephen Hill, Friedrich König, and Ulf Leonhardt. “Fiber-optical analog of the event horizon”. In: *Science* 319.5868 (2008), pp. 1367–1370.
- [127] Jie Gu, Hairun Guo, Shaofei Wang, and Xianglong Zeng. “Probe-controlled soliton frequency shift in the regime of optical event horizon”. In: *Optics Express* 23.17 (2015), pp. 22285–22290.
- [128] A Demircan, Sh Amiranashvili, and G Steinmeyer. “Controlling light by light with an optical event horizon”. In: *Physical Review Letters* 106.16 (2011), p. 163901.
- [129] C. Milián, T. Marest, A. Kudlinski, and D. V. Skryabin. “Spectral wings of the fiber supercontinuum and the dark-bright soliton interaction”. In: *Opt. Express* 25.9 (May 2017), pp. 10494–10499. DOI: 10.1364/OE.25.010494.
- [130] K. E. Webb, Y. Q. Xu, M. Erkintalo, and S. G. Murdoch. “Generalized dispersive wave emission in nonlinear fiber optics”. In: *Optics Letters* 38.2 (2013), pp. 151–153. DOI: 10.1364/OL.38.000151.
- [131] Quan Sun, Hidenori Asahi, Yoshiaki Nishijima, Naoki Murazawa, Kosei Ueno, and Hiroaki Misawa. “Pulse duration dependent nonlinear propagation of a focused femtosecond laser pulse in fused silica”. In: *Opt. Express* 18.24 (Nov. 2010), pp. 24495–24503. DOI: 10.1364/OE.18.024495.
- [132] M. Kolesik, E. M. Wright, and J. V. Moloney. “Dynamic Nonlinear X Waves for Femtosecond Pulse Propagation in Water”. In: *Phys. Rev. Lett.* 92 (25 June 2004), p. 253901. DOI: 10.1103/PhysRevLett.92.253901.

-
- [133] A. Couairon, E. Gai žauskas, D. Faccio, A. Dubietis, and P. Di Trapani. “Non-linear X-wave formation by femtosecond filamentation in Kerr media”. In: *Phys. Rev. E* 73 (1 Jan. 2006), p. 016608. DOI: 10.1103/PhysRevE.73.016608.
- [134] Yoshitomo Okawachi, Mengjie Yu, Jaime Cardenas, Xingchen Ji, Michal Lipson, and Alexander L Gaeta. “Coherent, directional supercontinuum generation”. In: *Optics Letters* 42.21 (2017), pp. 4466–4469.
- [135] Johan Hult. “A fourth-order Runge–Kutta in the interaction picture method for simulating supercontinuum generation in optical fibers”. In: *Journal of Lightwave Technology* 25.12 (2007), pp. 3770–3775.
- [136] DV Skryabin, F Luan, JC Knight, and P St J Russell. “Soliton self-frequency shift cancellation in photonic crystal fibers”. In: *Science* 301.5640 (2003), pp. 1705–1708.
- [137] AV Yulin, DV Skryabin, and P St J Russell. “Four-wave mixing of linear waves and solitons in fibers with higher-order dispersion”. In: *Optics Letters* 29.20 (2004), pp. 2411–2413.
- [138] Peter M Moselund. *Long-pulse supercontinuum light sources*. Ph.D. thesis, DTU Fotonik, Technical University of Denmark, 2009.
- [139] R. H. Stolen, J. P. Gordon, W. J. Tomlinson, and H. A. Haus. “Raman response function of silica-core fibers”. In: *J. Opt. Soc. Am. B* 6.6 (June 1989), pp. 1159–1166. DOI: 10.1364/JOSAB.6.001159.

Appendix A

A. Reprint permission from OSA

Simon Christensen

From: pubscopyright <copyright@osa.org>
Sent: 24. september 2020 16:02
To: Simon Christensen; pubscopyright
Subject: RE: Copyright permission for JOSAB paper " Directional supercontinuum generation: the role of the soliton "

Dear Simon Christensen,

Thank you for contacting The Optical Society (OSA).

For the use of material from Simon Christensen, Shreesha Rao D. S., Ole Bang, and Morten Bache, "Directional supercontinuum generation: the role of the soliton," J. Opt. Soc. Am. B 36, A131-A138 (2019):

Because you are the author of the source paper from which you wish to reproduce material, OSA considers your requested use of its copyrighted materials to be permissible within the author rights granted in the Copyright Transfer Agreement submitted by the requester on acceptance for publication of his/her manuscript. If the entire article is being included, it is requested that the **Author Accepted Manuscript** (or preprint) version be the version included within the thesis and that a complete citation of the original material be included in any publication. This permission assumes that the material was not reproduced from another source when published in the original publication.

The **Author Accepted Manuscript** version is the preprint version of the article that was accepted for publication but not yet prepared and/or formatted by The Optical Society or its vendors.

Please let me know if you have any additional questions.

Kind Regards,
Hannah Greenwood

Hannah Greenwood
September 23, 2020
Authorized Agent, The Optical Society

The Optical Society (OSA)
2010 Massachusetts Ave., NW
Washington, DC 20036 USA
www.osa.org

Reflecting a Century of Innovation

From: Simon Christensen <sichr@fotonik.dtu.dk>
Sent: Monday, September 21, 2020 6:24 AM
To: pubscopyright <copyright@osa.org>
Subject: Copyright permission for JOSAB paper " Directional supercontinuum generation: the role of the soliton "



Copyright:
Simon Christensen and DTU Fotonik
All rights reserved.
ISBN: XXXXXXXX

Published by:
DTU Fotonik
Technical University of Denmark

Simon Christensen was born in Denmark in 1992. He received his Bachelor of Science degree from Copenhagen University in 2014. In February 2017, he earned his Master of Science degree in Physics, with a specialization in Quantum Optics at Copenhagen University for his work on "Characterization of quantum photonic circuits". In April 2017, Simon started working in the Ultrafast Optics and Terahertz Science group, Department of Photonics Engineering, the Technical University of Denmark to pursue his Ph.D. degree. The Ph.D. work revolved around the generation of supercontinuum in Silicon Nitride waveguides using femtosecond laser sources.

DTU Fotonik
Department of Photonics Engineering
Technical University of Denmark

DTU Fotonik
Building 343
2800 Kongens Lyngby, Denmark
Phone +45 4525 6352
fotonik@fotonik.dtu.dk
www.fotonik.dtu.dk



